

## ABSTRACT

Title of Document: SYNTHESIS, CHARACTERIZATION AND CATALYTIC STUDIES OF BIMETALLIC NANOPARTICLES

Anthony Greg Dylla, Doctor of Philosophy,  
2009

Directed By: Professor Robert A. Walker, Department of  
Chemistry and Biochemistry

Due to the ever-increasing desire for catalysts that possess high activities and selectivities for industrially relevant reactions, much effort is being spent on the synthesis of mono and bimetallic nanoparticles with tunable characteristics such as size, shape and bimetallic composition. Understanding how these characteristics influence catalytic performance is the key to rationally designing catalysts for a specific reaction. While significant breakthroughs have been made, particularly in the area of monometallic nanoparticles with regard to shape and size, relating the bimetallic structure, i.e., core@shell or alloy to a specific reactivity remains a difficult task.

Work presented in this thesis describes the synthesis, characterization and catalytic properties of mono and bimetallic nanoparticles. Our efforts were motivated by the desire to understand the relationships that exist between metallic nanoparticle

structure and their function as catalysts. This work also seeks to better understand the dynamic changes a nanoparticle's structure undergoes during typical catalytic operating conditions. Our approach is to use a wide array of analytical tools including optical methods, electron microscopy, XRD and mass spectrometry to provide an interlocking description of nanoparticle structure, function and durability.

We show how the polymer coatings and degraded carbonaceous deposits affect propene hydrogenation catalytic activity of Pt nanoparticles. We also present a unique view of the interplay between thermodynamic and kinetic variables that control bimetallic nanoparticle alloy structures by looking at ordered and disordered PdCu alloy nanoparticles as a function of particle size.

In another study we show that Ru@Pt and PtRu alloy nanoparticle catalysts have similar surface structures under oxidizing conditions but completely different surface structures under reducing conditions as probed by vibrational spectroscopy. These differences and similarities in surface composition correlate very well to their catalytic activity for CO oxidation under oxidizing and reducing environments, respectively.

Finally, we present the synthesis and characterization of Cu@Pt nanoparticles with a particular focus on the core@shell formation mechanism. We also show how dramatic changes in the surface electronic structure of Cu versus Cu@Pt nanoparticles can affect their ability to transform light into heat by using Raman spectroscopy to observe graphite formation on the surface of these nanoparticles.

SYNTHESIS, CHARACTERIZATION AND CATALYTIC  
STUDIES OF BIMETALLIC NANOPARTICLES

By

Anthony Greg Dylla

Dissertation submitted to the Faculty of the Graduate School of the  
University of Maryland, College Park, in partial fulfillment  
of the requirements for the degree of  
Doctor of Philosophy  
2009

Advisory Committee:

Professor Robert A. Walker, Chair

Professor Bryan W. Eichhorn

Professor Janice E. Reutt-Robey

Professor Sang Bok Lee

Professor Gregory S. Jackson, Dean's Representative

© Copyright by  
Anthony Greg Dylla  
2009

## Dedication

This dissertation is dedicated in memory of my stepfather, Rich Inselmann.

## Acknowledgements

I would like to thank my advisors, Prof. Rob Walker and Prof. Bryan Eichhorn for their support over the past 5 years. They are both proof that a lot more goes into being a good advisor than just being a good scientist – intangibles count.

Thank you to former and current lab mates for scientific discussion and friendship: Prof. Carmen Huffman, Prof. Shenghu Zhou, Dr. Mike Pomfret, Dr. Suleyman Can, Dr. Wendy Heiserman, Dr. Mike Brindza, Sanem Kocak, Bryan Eigenbradt, Renee Siler, Debjani Roy, Ryan Murphy, Pavan Bellamkonda, Chris Sims, Dr. ZhuFang Liu and Dr. Chunjuan Zhang. I want to especially thank Dr. Selim Alayoglu for many helpful and highly rigorous discussions regarding research and also for providing the PtRu catalysts studied in Chapter 4. Thank you to Dr. Zili Wu at Oak Ridge National Lab for the kind hospitality and help with the DRIFTS experiments in Chapter 4. Thanks to Adam Kopp who performed the Raman spectroscopy experiments found in Chapter 5. Thank you to Prof. James Dumesic and Mark Tucker at the University of Wisconsin, Madison for performing the CO chemisorption measurements in Chapter 2. Thank you to Dr. Larry Lai for help with the STEM-EDS line scans found in Chapter 4. Finally, I want to thank my mom, dad and stepmom for always supporting me and giving me the freedom to wander my own path.

# Table of Contents

Dedication.....	ii
Acknowledgements.....	iii
Table of Contents.....	iv
List of Tables.....	vi
List of Figures.....	vii
List of Abbreviations.....	ix
Chapter 1: Background and Introduction.....	1
1.1 Uniqueness of the Nano Size Regime.....	1
1.2 Bimetallic Clusters and Nanoparticles in Catalysis: A Brief History.....	5
1.3 Bimetallic Nanoparticles: Synthesis and Structures.....	7
1.4 Bimetallic Nanoparticles: Characterization.....	10
1.5 Putting it All Together: Surface Science, Theory and Nanoparticles.....	18
1.6 Overview of the Thesis.....	19
1.7 References.....	20
Chapter 2: Nanoparticle Stabilizer Effects on Heterogeneous Catalytic Transformations.....	27
2.1 Introduction.....	27
2.2 Experimental.....	30
2.2.1 Synthesis of Platinum Nanoparticles.....	30
2.2.2 Preparation of Catalyst Materials.....	30
2.2.3 TGA Analysis.....	31
2.2.4 Raman Experiments.....	31
2.2.5 CO Titration Experiments.....	31
2.2.6 Catalysis Experiments.....	32
2.2.7 TEM Analysis.....	32
2.3 Results and Discussion.....	33
2.3.1 Platinum Nanoparticle Properties.....	33
2.3.2 Catalysis.....	35
2.4 Summary.....	42
2.5 Supplemental Information.....	43
2.6 References.....	44
Chapter 3: $\alpha \rightarrow \beta \rightarrow \alpha$ Phase Transitions of PdCu Alloy Nanoparticles and Catalysts .....	47
3.1 Introduction.....	47
3.2 Experimental.....	50
3.2.1 Synthesis.....	50
3.2.2 Characterization.....	51
3.3 Results and Discussion.....	53
3.3.1 TEM and FTIR-CO Probe Characterization.....	53
3.3.2 XRD Analysis of PdCu alloy NPs.....	56
3.3.3 Comparison of PdCu alloy NPs and Highly Diluted Catalyst Materials.....	59
3.4 Conclusions.....	60

3.5 References.....	61
Chapter 4: Ru@Pt and PtRu Alloy Nanoparticles: Combined DRIFT Spectroscopy and Catalysis Studies on Surface Segregation and Surface Redox Properties .....	63
4.1 Introduction.....	63
4.2 Experimental.....	65
4.2.1 Synthesis .....	65
4.2.2 Characterization.....	66
4.3 Results and Discussion .....	67
4.3.1 TEM and EDS Line Scan Analysis.....	67
4.3.2 DRIFT Spectroscopy .....	69
4.3.3 Preferential CO Oxidation (PROX) and CO Oxidation Catalysis.....	75
4.4 Summary .....	79
4.5 Supplemental Information .....	80
4.6 References.....	80
Chapter 5: Cu@Pt (core@shell) Nanoparticles: Synthesis and Characterization .....	83
5.1 Introduction.....	83
5.2 Experimental.....	85
5.2.1 Synthesis of Cu@Pt (core@shell) Nanoparticles .....	85
5.2.1 Synthesis of Cu@CuO (core@shell) Nanoparticles.....	86
5.2.2 Characterization.....	86
5.3 Results and Discussion .....	89
5.3.1 Synthesis .....	89
5.3.2 TEM.....	90
5.3.3 FTIR-CO.....	91
5.3.4 UV-Vis.....	94
5.3.5 XRD.....	95
5.3.5 micro-Raman.....	97
5.4 Conclusions.....	101
5.5 Supplemental Information .....	101
5.6 References.....	104
Chapter 6: Conclusions and Future Work.....	106
6.1 Conclusions.....	106
6.2 Future Work.....	108
Co-author contributions and acknowledgements.....	110
Alphabetical Listing of References by First Author .....	111

This Table of Contents is automatically generated by MS Word, linked to the Heading formats used within the Chapter text.

## List of Tables

Table 2.1 CO chemisorption data for N <sub>2</sub> , H <sub>2</sub> and air annealed 1%Pt/Al <sub>2</sub> O <sub>3</sub> catalysts .....	40
Table 4.1 IR band assignments of CO on Pt, Ru, and Pt-Ru nano-catalysts and surfaces .....	69

## List of Figures

Figure 1.1 Surface area to volume ratio as a function of particle size.....	2
Figure 1.2 Schematic of various bimetallic nanoparticle architectures .....	8
Figure 1.3 Example of TEM and EDS line scan.....	11
Figure 1.4 Example of nanoparticle XRD .....	12
Figure 1.5 Example of UV-Vis showing nanoparticle SPR band .....	15
Figure 1.6 Example of FTIR-CO probe of colloidal nanoparticle suspensions.....	16
Figure 2.1 TEM of 8 nm Pt nanoparticles used to make 0.1% Al <sub>2</sub> O <sub>3</sub> catalysts.....	32
Figure 2.2 TGA of Pt nanoparticles under N <sub>2</sub> and air atmospheres.....	34
Figure 2.3 Raman spectra of pre and post TGA Pt nanoparticles.....	34
Figure 2.4 TPR plots of 0.1% Pt/Al <sub>2</sub> O <sub>3</sub> for the propene hydrogenation reaction.....	36
Figure 2.5 Scatter plot of steady state conversion efficiencies for 0.1% Pt/Al <sub>2</sub> O <sub>3</sub> catalysts for propene hydrogenation .....	38
Figure S2.1 TEM images of pre and post reaction 0.1% Pt/Al <sub>2</sub> O <sub>3</sub> catalysts .....	43
Figure S2.2 Table of steady state conversion efficiencies for 0.1% Pt/Al <sub>2</sub> O <sub>3</sub> catalysts .....	43
Figure 3.1 TEM image of 4 nm PdCu nanoparticles .....	53
Figure 3.2 TEM image of 2.5% PdCu/SiO <sub>2</sub> catalyst .....	54
Figure 3.3 FTIR-CO spectra of PdCu and monometallic Cu and Pd nanoparticle colloids.....	54
Figure 3.4 FTIR-CO spectra of time-lapse PdCu nanoparticle colloids.....	55
Figure 3.5 Phase diagram of the Pd-Cu alloy .....	56
Figure 3.6 XRD of PdCu nanoparticles after annealing .....	57
Figure 3.7 XRD of PdCu nanoparticles after solution annealing .....	58
Figure 3.8 XRD of PdCu nanoparticles and 2.5% PdCu/SiO <sub>2</sub> catalyst after annealing at 210 °C .....	58

Figure 4.1 TEM image of PtRu alloy and Ru@Pt nanoparticles.....	67
Figure 4.2 STEM-EDS line scan of oxidized/reduced 1% Ru@Pt/Al <sub>2</sub> O <sub>3</sub> catalyst....	68
Figure 4.3 DRIFTS CO adsorption of oxidized/reduced 1% Ru@Pt and PtRu alloy/Al <sub>2</sub> O <sub>3</sub> catalysts.....	71
Figure 4.4 TPR plots of CO oxidation and PROX reactions for 1% Ru@Pt and PtRu alloy/Al <sub>2</sub> O <sub>3</sub> catalysts.....	76
Figure 4.5 Schematic representations of surface states of Ru@Pt and PtRu alloy nanoparticles under reducing and oxidizing conditions.....	78
Figure S4.1 DRIFT CO adsorption of oxidized/reduced 1% Ru/Al <sub>2</sub> O <sub>3</sub> catalyst.....	80
Figure 5.1 TEM image of Cu and Cu@Pt nanoparticles.....	90
Figure 5.2 TEM image of Cu and Cu@CuO nanoparticles.....	91
Figure 5.3 Time-lapse FTIR-CO probe of Cu and Cu@CuO nanoparticle colloid suspensions.....	92
Figure 5.4 Time-lapse FTIR-CO probe of Cu and Cu@Pt nanoparticle colloid suspensions.....	93
Figure 5.5 Time lapse UV-Vis of Cu and Cu@Pt nanoparticle colloid suspensions	95
Figure 5.6 Time-lapse XRD of Cu and Cu@CuO nanoparticles.....	96
Figure 5.7 Time-lapse XRD of Cu and Cu@Pt nanoparticles.....	96
Figure 5.8 Raman spectra of Cu, Pt and Cu@Pt nanoparticles collected with 488 and 633 nm excitation.....	99
Figure S5.1 FTIR-CO probe of attempted Cu@CuO@Pt nanoparticle colloid suspension.....	101
Figure S5.2 FTIR-CO probe of monometallic Pt nanoparticle colloid suspension ...	102
Figure S5.3 UV-Vis of Cu and Cu@CuO nanoparticle colloid suspensions.....	102
Figure S5.4 Raman spectrum of neat PVP collected with 633 nm excitation.....	103
Figure S5.5 Raman spectra of Cu nanoparticles acquired with 488 and 633 nm excitation at different laser powers.....	103

## List of Abbreviations

AES	Auger Electron Spectroscopy
BCC	Body Centered Cubic
D band	Disorder Induced Phonon Mode
DFT	Density Functional Theory
DHN	Decahydronaphthalene
DRIFTS	Diffuse Reflectance Infrared Fourier Transform Spectroscopy
EELS	Electron Energy Loss Spectroscopy
EM	Electromagnetic
EXAFS	Extended X-ray Absorption Fine Structure
FCC	Face Centered Cubic
FTIR-CO	Fourier Transform Infrared – Carbon Monoxide Probe
FWHM	Full Width at Half Maximum
G band	Graphite Band
HR-TEM	High Resolution – Transmission Electron Microscopy
LEED	Low Energy Electron Diffraction
$M_1@M_2$	Core(Metal <sub>1</sub> )@Shell(Metal <sub>2</sub> )
ML	Monolayer
MWT	Molecular Weight
NP	Nanoparticle
PGM	Platinum Group Metal
PROX	Preferential CO Oxidation
PVP	Polyvinylpyrrolidone
SA	Surface Area
SPR	Surface Plasmon Resonance
STEM-EDS	Scanning Transmission Electron Microscopy – Energy Dispersive Spectroscopy
STM	Scanning Tunneling Microscopy
TOF	Turn Over Frequency

TOPO	Trioctylphosphine Oxide
TGA	Thermal Gravimetric Analysis
TPR	Temperature Programmed Reaction
UV-Vis	Ultraviolet-Visible Spectroscopy
XANES	X-ray Absorption Near Edge Spectroscopy
XPS	X-ray Photoelectron Spectroscopy
XRD	X-ray Diffraction

# Chapter 1: Background and Introduction

## 1.1 Uniqueness of the Nano Size Regime

The physical and chemical properties of nanoparticles are not easily predicted because nanoparticles are neither molecules nor bulk materials. This unusual nature of nanoparticles is often described as the quantum size effect that leads to unique bonding and electronic structures.<sup>1-3</sup> The simplest example of how the electronic structures of nanoparticles are quite distinct from those associated with macroscopic and molecular systems are quantum dots. While the electrons of atoms have discrete atomic orbitals and the electronic nature of bulk solid-state materials ( $>10^{20}$  atoms) is defined by the continuous band structure, quantum dots can fluoresce like molecules but the fluorescence wavelength is determined by their physical size. As the size of the particle decreases, the continuous band structure of the material begins to break up and become more discrete because of quantum confinement effects.<sup>4</sup> The electronic structure of a nanoparticle then lies somewhere between that of bands and discrete atomic orbitals.

Another example of the quantum size effect is the visible surface plasmon resonance (SPR) of Cu, Ag and Au nanoparticles.<sup>5, 6</sup> As the diameter of the particle becomes very small compared to the wavelength of visible light, the surface electrons of the nanoparticle move collectively under the effect of an applied electromagnetic (EM) field. These collective oscillations create surface plasmons in contrast to free plasmons observed in the bulk metals and become resonant with EM radiation in the visible region for these metals. The absorbance of the visible light due to plasmon

absorbance is the reason that suspensions of nanoparticles of these metals are colored. These two examples – quantum dots and noble metal nanoparticles – show that by confining a material to the nanoscale, unpredictable and unique properties can be observed. These unique physical and chemical properties of nanoparticles can also make them candidates to be highly active catalyst materials.

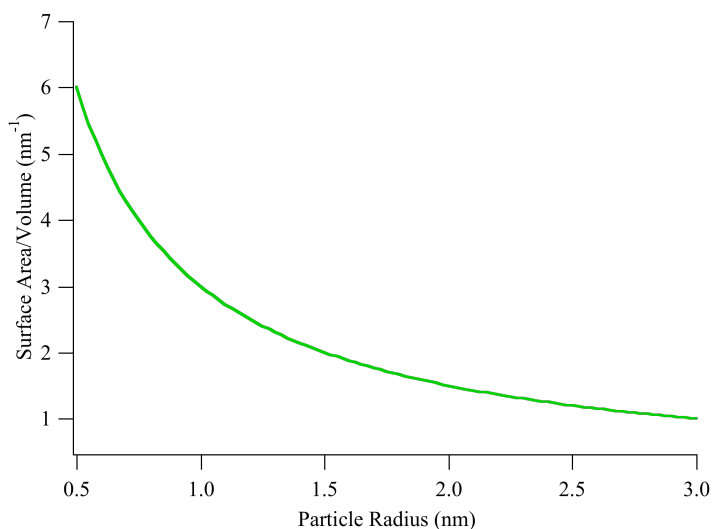


**Figure 1.1** A plot of surface area / volume as a function of particle radius. The plot assumes perfectly spherical particles and covers a range of diameters from 1.0-6.0 nm.

Since all heterogeneous catalysis occurs at a surface, the most obvious advantage to using nano-sized particles is that they have large surface to volume ratios. Figure 1 shows a plot of surface area / volume as a function of particle radius. The surface area to volume  $1/r$  dependence shows clearly that as the particle size decreases, the amount of active surface material increases. By increasing the amount of surface area for a given volume of atoms, the use of expensive platinum group metals (PGMs) for catalysis can be seen as “atomically economical.”

Other nano-size effects that are relevant to catalysis are surface strain and highly uncoordinated surface atoms. Because of their small size and correspondingly large amount of faceting at the surface, nanoparticles have highly uncoordinated surface atoms with highly strained bonding in the surface region. In turn, differences in surface bonding can change the d-band electronic structure of the nanoparticle's surface.<sup>7</sup> This phenomenon has been studied extensively by Norskov and Hammer who used DFT calculations to predict shifts in d-band levels based on the surface strain of a variety of transition metal overlayer structures, where strain is defined as lattice expansion or contraction due to the mismatch in atomic packing between different metals.<sup>8, 9</sup> They proposed that shifts in d-band structure can be correlated to adsorption energies of atoms or molecules at metallic surfaces. By understanding how the strain or stress of the nanoparticle surface relates to shifts in the d-band structure of the nanoparticle, rational design of catalysts with appropriate binding energies of key intermediates can be achieved.

Au nanoparticles used as heterogeneous catalysts are a classic example of how highly uncoordinated edge or terrace surface atoms can affect catalytic activity. Bulk Au is inert but if the diameter of Au particles fall below 10 nm, the nanoparticles become active CO oxidation and propylene epoxidation catalysts. The turnover frequency (TOF) for CO oxidation increases by an additional order of magnitude as the size of the Au nanoparticle decreases from 10 nm to 3 nm. The enhanced activity is believed to be due to the increase in highly active edge, corner and step sites as the particle size decreases.<sup>10, 11</sup>

Finally, due to the inherent non-equilibrium nature of nanoparticles, phases or architectures of nanoparticles that are normally forbidden by thermodynamics can be realized. The AuPt alloy bimetallic nanoparticle is a case in point. The thermodynamic phase diagram of the Au-Pt system shows that below 900 °C, alloys of any AuPt composition are not allowed. However, by controlling the rate of nanoparticle nucleation and growth during the solution-based synthesis, AuPt alloy nanoparticles can be synthesized at temperatures below 300 °C.<sup>12</sup> Though the alloy phase of AuPt nanoparticles is metastable and reverts to a segregated heteroaggregate structure upon heating at high temperatures, this example illustrates how kinetic pathways open for new material formation when a system is confined to the nanoscale.

As the examples above have shown, nanoparticles provide a unique opportunity to control the physical and chemical properties of metals outside of the realm of molecules and bulk materials. Advances in nanoparticle synthesis with respect to the control of size and shape continue to provide new materials with unique catalytic properties. Furthermore, by combining two metals to create bimetallic nanoparticles, a vast set of possible nanostructures becomes possible. In particular, the ability to control the architecture of a nanoparticle, i.e., alloy, core@shell and heteroaggregate, can lead to the creation of materials with high selectivity and activity for a wide variety of important heterogeneous transformations. The next section will give a brief overview of the history of catalysis on surfaces and nanoparticles.

## 1.2 Bimetallic Clusters and Nanoparticles in Catalysis: A Brief History

Much of the early work on nano-scale bimetallic systems came from the study of transition-metal carbonyl clusters in the 1960s. These clusters with total metal atoms numbering from 10 to 100 are often seen as the precursors to bimetallic nanoparticles that typically have 1000s to 10000s of atoms. These early clusters were initially investigated as homogeneous catalysts, but they were soon supported on surfaces or micropores to be used as heterogeneous catalysts after high temperature calcination to remove CO ligands. Sinfelt and coworkers at Exxon in the late 1960s and early 1970s pioneered many of the characterization studies of highly dispersed supported metal clusters of Pt-Ir, Pt-Re and Ru-Cu used for reforming reactions using extended x-ray adsorption fine structure (EXAFS) and Mössbauer effect spectroscopy.<sup>13, 14</sup>

Further studies on a wide range of molecular precursor derived, bimetallic clusters continued throughout the 1980s and into the 1990s with an emphasis on structural characterization by EXAFS.<sup>15-17</sup> This period of work also began studying the catalytic behavior of platinum group metal (PGM) bimetallic nanoparticles from a synergistic viewpoint whereby the combination of the two metals together enhanced the catalytic activity or selectivity relative to the monometallic components by themselves.<sup>18-20</sup> Also during this time the early foundations of catalytic surface science were being laid by Ertl<sup>21-23</sup>, Somorjai<sup>24-26</sup>, Goodman<sup>27-29</sup> and others. Their work focused primarily on studying catalytic metal surfaces via high-pressure sum frequency generation (SFG), high-pressure scanning tunneling microscopy (STM), XPS, AES and LEED. Much of what is known about the adsorption properties of

gas-phase molecules, atoms and intermediates on surfaces came from these early studies. Furthermore, understanding how catalytic activity and selectivity are correlated to differences in surface atom geometry as well as the reactivity of edge versus planar surface sites is emerging from this work. Data showed that not only was the mobility of reactant molecules and atoms on surfaces important but also the diffusion of metallic surface atoms themselves played a role in determining the activity and/or selectivity of a given catalyst. Surface science research then moved on to more complex bimetallic alloyed and overlayer surfaces with the goal of understanding how two metals worked synergistically to give higher catalytic activity or selectivity than the monometallic components on their own. The development of synthetic methods for making bimetallic nanoparticles of analogous architectures (alloy and core@shell) was then in its infancy while the understanding of catalytic activity at bimetallic surfaces was well underway. In the past decade, we would see these two areas begin to converge leading to a greater understanding of complex and industrially relevant catalysts having nanometer dimensions.

Since the mid-1990s the groups of Toshima<sup>20, 30, 31</sup>, Bradley<sup>32-35</sup>, Crooks<sup>36-38</sup>, El-Sayed<sup>39-41</sup>, Schaak<sup>42, 43</sup>, Cheon<sup>44-46</sup>, Somorjai<sup>47-50</sup> and others have developed and characterized small colloidal alloy and core@shell bimetallic nanoparticles prepared primarily from metal salt reduction methods. Along with breaking new ground in the development of methodologies for synthesizing increasingly complex bimetallic nanoparticles, these groups performed many of the initial catalytic studies aimed at elucidating the relationships between well-characterized, bimetallic nanoparticle structure and their function as catalysts. The synthesis and characterization of this last

group of bimetallic nanoparticles will be the primary focus of the next section of the introduction. This chapter will conclude with a brief discussion of relevant surface science studies and DFT calculations as they relate to these bimetallic nanoparticle architectures.

### 1.3 Bimetallic Nanoparticles: Synthesis and Structures

The most common method for producing bimetallic nanoparticles of controllable size, shape and architecture is the solution phase nucleation method.<sup>5, 51, 52</sup> In the most basic scheme, metal salt precursors (e.g., metal nitrates, acetates, carbonyl complexes, chlorides, etc.) are dissolved in an appropriate solvent (e.g., polyols, alcohols, ethers, decahydronaphthalene DHN, etc.) and a polymer (e.g., polyvinylpyrrolidone, PVP), or surfactant/ligand (e.g., citrates, thioethers, long-chain alkyl amines, trioctylphosphine oxide TOPO, etc) is added to act as a surface stabilizer for the formed colloidal nanoparticle. The solution is typically heated in the presence of a reducing agent (e.g., NaBH<sub>4</sub>, butyl lithium, H<sub>2</sub> gas, etc.) that reduces the metal ions to their metallic state and initiates the formation of the nanoparticles. A variation on the general solution method is the use of electrochemistry to reduce monometallic or bimetallic precursors at a cathode in the presence of passivating ligands or polymers. Bimetallic colloids such as Pd-Ni, Fe-Co and Fe-Ni have been prepared by this method.<sup>53, 54</sup>

As one can imagine, based on the availability of controllable parameters such as temperature of reaction, choice of precursors and passivating agents and their concentrations, strength of reducing agent, order of reagent addition and time at a

given temperature, the opportunities to create unique bimetallic nanostructures using the solution method are quite large. The next section will give a summary of these bimetallic nanoparticle architectures along with a discussion on some of the kinetic and thermodynamic variables responsible for their formation.

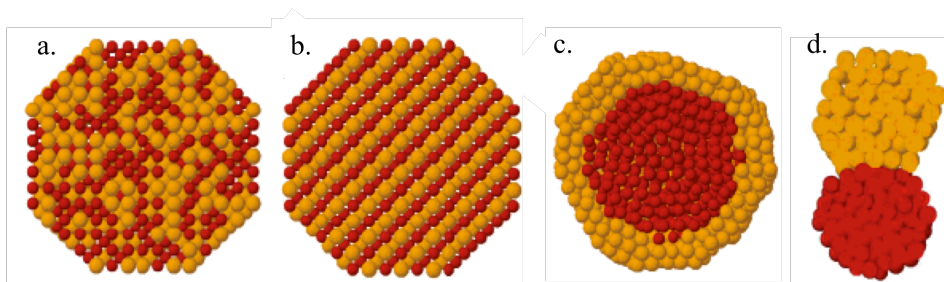


**Figure 1.2** Several bimetallic nanoparticle architectures including (a) disordered alloy (b) ordered alloy (c) core@shell and (d) heteroaggregate. Schematic adapted from reference [82].

As mentioned in the previous section, the ability to synthesize desired architectures of bimetallic nanoparticles opens up new avenues for creating unique catalytic materials with high activity and selectivity for important catalytic transformations. Figure 2 shows schematic representations of several possible architectures of nanoparticles. Though not all of the possible nanoparticle architectures are shown here, the architectures in Figure 2 represent the most commonly studied structures.

The most widely studied bimetallic nanoparticle architecture is the alloy as seen in Figs. 2a and 2b. There are several sub-categories of the alloy including the cluster-in-cluster alloy, random alloy and ordered or intermetallic alloy. Toshima and coworkers as well as Bradley and coworkers have performed extensive studies on the Pd-Cu alloy system with the goal of elucidating the particular alloy structure by EXAFS measurements.<sup>30, 35</sup> Due to the preference for heteroleptic bonding over

homoleptic bonding in the Pd-Cu pair as well as differences in surface energies of Pd and Cu, the PdCu bimetallic nanoparticle forms a disordered or solid solution alloy structure. Conversely, AuPd bimetallic nanoparticles prepared by co-reduction of Au and Pd salts adopt an inhomogeneous cluster-in-cluster nanoparticle due to the preference of homoleptic bond formation.<sup>55</sup> Schaak and coworkers have performed numerous studies on atomically ordered (Fig. 2b) bimetal intermetallic nanomaterials such as PdZn, AuZn, CuZn, AuCu and others.<sup>43, 56, 57</sup> In their work, preformed monometallic nanoparticle powders or films of colloids are mixed and then oven annealed at relatively low temperatures. Due to short diffusion distances afforded by using nanoparticle precursors, many ordered intermetallic nanoparticles have been generated by this method. As mentioned earlier in this chapter, the AuPt bimetallic nanoparticle represents a system where thermodynamically unfavorable products can be kinetically trapped via metal salt reduction solution methods.

The core@shell nanoparticle architecture seen in Fig. 2c can be considered a special type of alloy structure where the degree of alloying at the interface of  $M_1$  and  $M_2$  can be fairly sharp or diffuse in nature. Examples of these structures from the literature include Pd@Pt<sup>58, 59</sup>, Pt@Pd<sup>60</sup>, Cu@Pt<sup>61</sup>, Co@Pt<sup>44</sup>, Ru@Pt<sup>62, 63</sup> and Au@Pd<sup>55</sup>. One of the most straight-forward approaches to creating core@shell nanoparticles is the sequential deposition method. Initially, monometallic nanoparticles are synthesized to form the core. The metal salt precursor of the shell material is then added to the colloidal suspension of core nanoparticles and is further heated. The deposition of the shell material onto the core nanoparticle can occur through several mechanisms. In the case of Co@Pt, Pt atoms are reduced at the

surface of the Co nanoparticle at the expense of Co surface atom oxidation. This core@shell nanoparticle formation mechanism is commonly referred to as transmetalation.<sup>44</sup> In cases where the core metal nanoparticle is not as readily oxidized as in the case of the Pd@Pt system, surface adsorbates are used to deposit the shell metal. Toshima and coworkers bubbled H<sub>2</sub> gas into a colloidal suspension of preformed Pd nanoparticles to saturate the Pd nanoparticle surface with hydride. The surface hydride then served as the redox couple needed to reduce Pt at the surface to create the desired Pd@Pt nanoparticle.<sup>58</sup>

Finally, the heteroaggregate structure seen in Fig. 2d is an example of a bimetallic nanoparticle with minimal heteroleptic bonding. An example of this structure is the Au-Pt system described earlier. In the Au-Pt system, dendritic arms of Pt grow on preferred crystallographic planes of Au core nanoparticles.<sup>12</sup> The minimal alloying of the metals is consistent with the Au-Pt phase diagram that shows no alloy phase of the two metals at temperatures below 900 °C.

#### 1.4 Bimetallic Nanoparticles: Characterization

Nanoparticles are intrinsically non-equilibrium structures due to their inherently high surface energies and also because the method of preparation can often involve kinetically trapping thermodynamically metastable phases of the nanoparticle. Thorough characterization provides important chemical and structural information needed to correlate the non-equilibrium structure to its catalytic activity. This section provides an overview of the most commonly used characterization tools and the information about the nanoparticle structure can be obtained from those techniques.

Transmission electron microscopy (TEM) is the most commonly used tool for obtaining morphological information about a nanoparticle. Particle size analysis software is often used to determine the statistical distribution of nanoparticle sizes by sampling large numbers of particles within multiple TEM images. High resolution TEM (HR-TEM) is often used to determine the lattice spacing of crystallographic planes as a pseudo-analytical tool for determining the chemical composition of a nanoparticle. Beyond the simple imaging of nanoparticles, TEM can also be used to elucidate the crystal structure of a nanomaterial. Crystallographic planes can be determined from elastically scattered electron beams using the bright field mode in the TEM. The observed Moire patterns can give information about the crystallinity and phase of the nanoparticle.

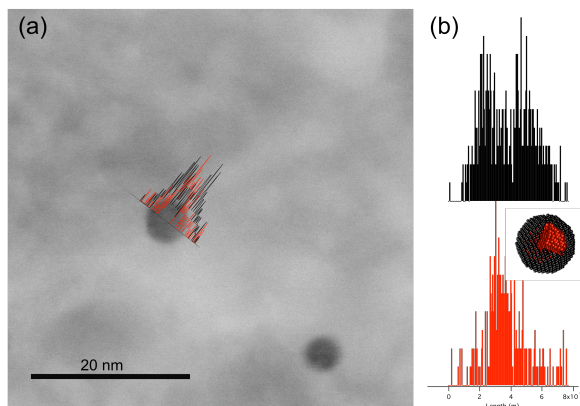


**Figure 1.3** (a) TEM image of Ru@Pt nanoparticles with EDS line scan overlay. (b) EDS line scans separated elementally for clarity along with an idealized Ru@Pt nanoparticle model.

Scanning transmission electron microscopy – energy dispersive spectroscopy (STEM-EDS) is an analytical and structural characterization tool often used to determine the elemental composition and spatial identity of atoms within multimetallic nanoparticles. Based on the energy of the X-rays emitted from nanoparticles bombarded by an electron probe, the technique can give the elemental

identification of a nanoparticle with  $\sim 1$  nm spatial resolution. STEM-EDS has proven to be a powerful technique for identifying complex bimetallic nanoparticle systems that are otherwise difficult to characterize. Figure 1.3 shows an example of an EDS line scan performed in STEM mode for Ru@Pt nanoparticles. The bimodal distribution of Pt at the edges and the Gaussian-like distribution of Ru at the core of the single nanoparticle show clearly that the nanoparticle has core@shell architecture.

Powder X-ray Diffraction (XRD) is a widely used characterization tool in nanoscience. Both the chemical identity and crystallographic structure of a nanoparticle can be determined from XRD.<sup>64</sup> X-rays diffracted from a material with any regularity in crystal structure will obey Bragg's law of diffraction (1):

$$n\lambda = 2d \sin \theta \quad (1)$$

where  $n$  is an integer of the order (typically 1),  $\lambda$  is the wavelength of the impinging x-rays,  $d$  is the lattice spacing of the material and  $\theta$  is the angle between the incident ray and the scattering planes. Based on the unique lattice spacing of a given metal, the

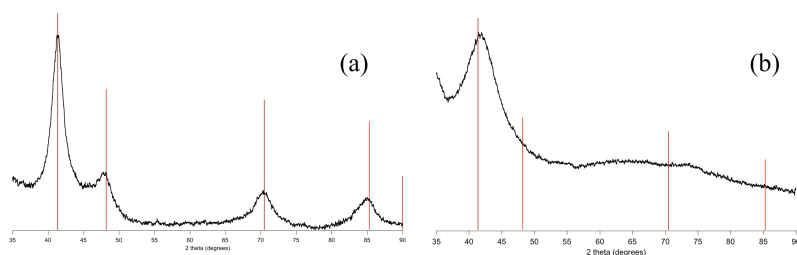


**Figure 1.4** XRD pattern of (a) 10 nm and (b) 3 nm diameter PdCu (50:50) alloy nanoparticles. Vertical lines represent ideal FCC diffraction of the (50:50) PdCu alloy.

elemental identity of a nanoparticle can often be determined based on the position of the diffraction peaks. Furthermore, the lattice spacing of a bimetallic alloy phase

varies linearly with the ratio of  $M_1$  to  $M_2$ . This linear relationship allows for the compositional determination of alloy phases based on diffraction peak position.

Figure 1.4 shows typical XRD patterns of alloyed nanoparticles. Information about the crystallite size of a nanomaterial can be, in some cases, quantitatively determined by the Scherrer equation (2):

$$\tau = \frac{K\lambda}{\beta \cos \theta} \quad (2)$$

where  $\tau$  is the crystallite size,  $K$  is the shape factor (typically 0.95),  $\beta$  is the full width at half maximum (FWHM) of the diffraction peak in radians and  $\lambda$  and  $\theta$  are the same as equation (1). Figure 1.4 is an illustrative example of the inverse relationship between the FWHM ( $\beta$ ) and the crystallite size of a nanoparticle ( $\tau$ ) of equation 2. The single, broad 111 diffraction seen in Figure 1.4b is an example of the often poorly crystalline nature of very small nanoparticles. This phenomenon of only observing one diffraction peak has been studied theoretically by Petkov.<sup>65</sup> Because face-centered cubic (FCC) metals predominantly adopt the low energy 111 plane at their surface and since a 3 nm particle has more than 60% of the atoms within the first layer of the surface, then the diffraction of that plane will be dominant over others. Finally, XRD can be used to distinguish between random (solid solution) alloys and ordered (intermetallic) alloy nanoparticles as the two types of alloy often have different crystallographic packing structures, i.e., FCC versus body centered cubic (BCC) which gives rise to different diffraction patterns.<sup>66</sup>

One limitation of XRD as a characterization tool is that diffraction peaks observed for mixtures of monometallic nanoparticles often are not easily distinguished from those of core@shell nanoparticles due to the phase segregated

nature of the latter. Another constraint is that very small nanoparticles (< 3 nm) often do not diffract due to the lack of any long-range crystalline order.

Although they are not used as characterization tools in the work presented in this thesis, XPS and EXAFS warrant mentioning as two other important x-ray based analytical tools used to understand the chemical and structural properties of nanoparticles. XPS uses x-ray absorption and the detection of ejected electrons as an elemental analysis tool. Because the inelastically scattered electrons have a mean free path in the range of 1-10 nm, only electrons from the topmost layer of a sample will be detected. Wieckowski and coworkers have done extensive studies using XPS to determine the chemical state of several bimetallic nanoparticles with various  $M_1:M_2$  ratios. Using theory and catalyst testing of these bimetallic nanoparticles, they correlate observed shifts in binding energies of metals from the XPS studies to trends in electrochemical catalytic activity.<sup>7, 67</sup>

Extended x-ray absorption fine structure (EXAFS) analysis measures the interference pattern that arises from ejected photoelectrons that interact with nearby atoms. The resultant interference pattern gives information about the coordination environment of an atom within a nanoparticle. EXAFS is a particularly useful tool for studying small bimetallic nanoparticles where the bonding environment of the atoms is highly complex.<sup>68</sup>

UV-Vis absorbance spectrometry is another tool used to characterize the electronic structure of noble metal containing nanoparticles. As discussed in the first section of this chapter, the SPR adsorption band of Au, Ag and Cu nanoparticles lie in the visible region. Figure 1.5 shows UV-Vis spectra of Cu and PtCu alloy

nanoparticles. The band at 565 nm in Figure 1.5a is due to the SPR absorption of Cu nanoparticles. The absorption spectrum of Cu nanoparticles is in striking contrast to PtCu alloy nanoparticles (Fig. 1.5b) that show only gradually rising absorbance across the visible region. This result suggests that the SPR bands of noble metals such as Cu are highly sensitive to the overall electronic structure of the nanoparticle.<sup>69</sup> This phenomenon will be explored further in Chapter 5 of this thesis.

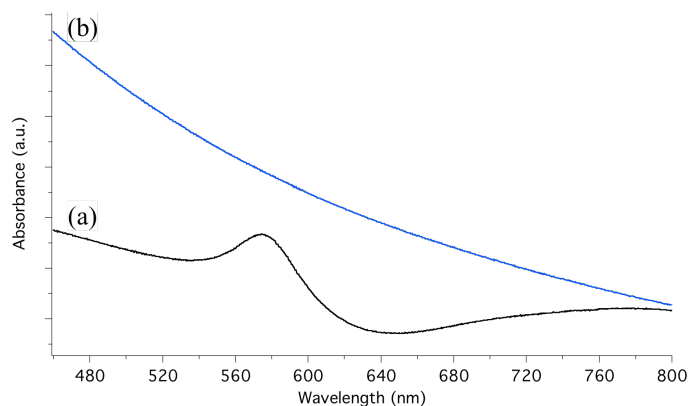


**Figure 1.5** UV-Vis of (a) Cu and (b) PtCu alloy nanoparticles.

FTIR is often used in combination with CO as a probe molecule to elucidate information about nanoparticle surfaces. Bradley and coworkers found that by bubbling CO through colloidal suspensions of nanoparticles, they could probe the surface structure of the nanoparticles based on the positions and relative intensities of the CO stretching frequency commonly observed in the 2200-1900  $\text{cm}^{-1}$  region.<sup>34</sup> Figure 1.6 shows FTIR-CO spectra of Cu and Pd nanoparticles. Several observations

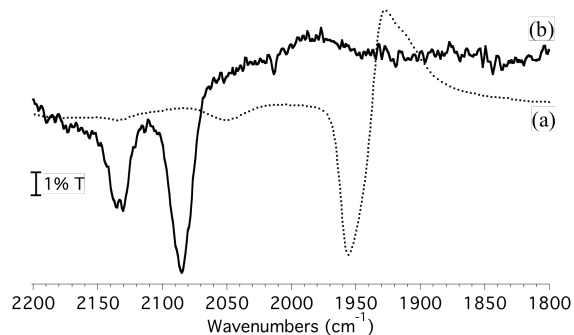


**Figure 1.6** FTIR-CO of (a) Pd and (b) Cu nanoparticles. The colloidal suspension was bubbled with CO for 10 minutes before measurement and the native colloidal suspension was used as the background. The band centered at  $2135\text{ cm}^{-1}$  is due to free CO.

are worth noting in this example. Pd nanoparticles (Fig. 1.6a) show two absorption peaks centered at  $1958$  (strong) and  $2050$  (weak)  $\text{cm}^{-1}$  that are due to CO bridge and linearly bound to Pd sites, respectively. Indirectly, the relative intensities for different binding geometries can give information about the morphology of the surface since terrace, edge and face sites bind CO differently. The absolute band position gives information about the strength of CO binding and therefore can reveal the identity of the metal based on the amount of electron donation into the CO molecule. Comparing CO adsorption on Pd versus Cu seen in Figs. 1.6a and 1.6b, respectively, shows clear differences between the two metals and thus offers a qualitative tool for determining the chemical composition of a nanoparticle surface. CO binds to metal surfaces via  $\sigma$ -bonding while a metal binds to CO through  $\pi$ -back bonding. The  $\pi$ -back bonding of the metal into the antibonding  $\pi^*$  orbitals of the CO causes a decrease in the CO bond order and subsequent red-shift in the CO stretching frequency due to weakening of the CO triple bond.<sup>70</sup> Furthermore, the band position can be used to identify oxidized surface species because of their decreased level of d electron back-donation, that causes a blue-shift relative to a metallic surface species.

Diffuse Reflectance Infrared Fourier Transform Spectroscopy (DRIFTS) is commonly used to study metal oxide supported nanoparticles under both *in situ* and *ex situ* conditions.<sup>71, 72</sup> Overbury and coworkers used *in situ* DRIFTS in conjunction with TPR studies to identify the surface oxidation state of Au nanoparticles under catalytically relevant CO oxidation conditions. They found that Au/SiO<sub>2</sub> catalysts initially calcined at 500 °C exhibit CO binding on Au nanoparticles consistent with Au<sup>n+</sup> and only by co-feeding CO with O<sub>2</sub> was the Au<sup>n+</sup> species reduced to Au<sup>0</sup>.<sup>73</sup> Many of the *ex situ* studies focus on using CO as a probe molecule to determine the qualitative chemical composition of a nanoparticle surface after cycling under catalytically relevant conditions.

Interpreting these IR-CO probe results is not without its challenges. Dipole coupling, lateral effects, competitive binding of nanoparticle stabilizers, and electron donation from one metal to another based on differences in electronegativity can all contribute to unpredictable shifts in frequency and changes in intensity.<sup>74</sup> Nevertheless, the technique is a powerful characterization tool that can help qualitatively and semi-quantitatively identify the surface chemical composition of a nanoparticle under catalytically relevant conditions.

Raman spectroscopy is often used to study catalytic materials due to the technique's inherent adaptability to *in situ* work. Several reasons for this asset include the scattering cross section of gas phase species being negligible; visible lasers allow for the fabrication of relatively inexpensive *in situ* cells, a reduction in black body background at high temperatures; low frequency vibrations including, M-O and M-C vibrational modes below 800 cm<sup>-1</sup> are easily observable.<sup>75</sup> Recently, Bao and

coworkers used Raman spectroscopy to study M-CO bonding that was used to identify active surfaces of RhMn nanoparticles inside carbon nanotubes.<sup>76</sup> Somorjai and coworkers have studied extensively via Raman spectroscopy the interaction of PVP with the surface of Rh and Pt nanoparticles.<sup>77, 78</sup>

### 1.5 Putting it All Together: Surface Science, Theory and Nanoparticles

Goodman and coworkers used XPS to study 1 monolayer (ML) thick metal overlayers on single crystal metal surfaces. They found that the core level binding energies of the metal overlayer shifted with respect to its single crystal monometallic counterpart. These shifts in binding energy correlated well to desorption temperatures for CO on the overlayer.<sup>27</sup> Later this group also reported on 1 ML thick Pd on a variety of single crystal substrates and found similar trends for CO adsorption energies.<sup>29</sup> They attributed this behavior to charge transfer interactions between the metal overlayer and its substrate metal based on the level of filling of the d-bands. This interpretation is significantly different from the mechanism proposed for bulk alloy surfaces where electronegativities dictate the direction of charge transfer. These overlayer structures can be viewed as close analogues to the core@shell architectures presented earlier in the introduction and can provide helpful guidance to making novel and highly active nanoparticle catalysts.

Hammer and Norskov used *ab initio* DFT calculations to correlate the observed shifts in the core level binding energies to variations in the d-band center of the metal overlayer structures.<sup>79, 80</sup> The level of d-band shifting with respect to the Fermi energy could then be correlated to interaction energies of a variety of molecular and atomic adsorbates.

Most recently, Mavrikakis and coworkers have used DFT calculations to study near surface alloy (NSA) bimetallic overlayer and sandwich structures.<sup>9, 81</sup> Results suggest that the electronic structure of the surface of a NSA is highly sensitive to the arrangement of the first few MLs of substrate. Some of these sandwich and overlayer structures are starting to be created as nanoparticle catalysts. Many of the trends in adsorption energies or reactivities observed by the surface science experiments are consistent with predictions made via DFT.

The realization of “catalyst by design” will likely only come about by combining the growing repertoire of complex and well-characterized bimetallic nanoparticle catalysts with the knowledge gained from both DFT theory and surface science analogue bimetallic structures.

## 1.6 Overview of the Thesis

The work in this thesis largely focuses on the synthesis, characterization and catalytic studies of various mono and bimetallic nanoparticle architectures. Chapter 2 looks at how PVP and its degradation products can affect hydrogenation activity of highly dispersed Pt nanoparticles. Chapter 3 is a systematic characterization of the ordered and disordered PdCu alloy nanoparticle system. Chapter 4 correlates redox dependent DRIFTS studies with the activity of PtRu alloy and Ru@Pt nanoparticle catalysts for CO oxidation and PROX. Chapter 5 presents the synthesis and characterization of the Cu@Pt nanoparticle system with an added emphasis on how changes in the SPR of Cu and Cu@Pt nanoparticles affect degradation behavior of PVP at the surface. Finally, Chapter 6 is a summary of the findings presented in this work and also provides some thoughts on the direction for future work.

## 1.7 References

- (1) Toshima, N.; Yonezawa, T. *New J. Chem.* **1998**, *22*, 1179-1201.
- (2) Aiken, J. D.; Finke, R. G. *J Mol Catal A-Chem* **1999**, *145*, 1-44.
- (3) Burda, C.; Chen, X. B.; Narayanan, R.; El-Sayed, M. A. *Chem. Rev.* **2005**, *105*, 1025-1102.
- (4) Wise, F. W. *Accounts Chem Res* **2000**, *33*, 773-780.
- (5) Tao, A.; Habas, S.; Yang, P. *Small* **2008**, *4*, 310-325.
- (6) Moores, A.; Goettmann, F. *New J. Chem.* **2006**, *30*, 1121-1132.
- (7) Lewera, A.; Zhou, W. P.; Hunger, R.; Jaegermann, W.; Wieckowski, A.; Yockel, S.; Bagus, P. S. *Chem. Phys. Lett.* **2007**, *447*, 39-43.
- (8) Greeley, J.; Norskov, J.; Mavrikakis, M. *Annu. Rev. Phys. Chem.* **2002**, *53*, 319-348.
- (9) Mavrikakis, M.; Hammer, B.; Norskov, J. K. *Phys. Rev. Lett.* **1998**, *81*, 2819-2822.
- (10) Haruta, M. *Gold Bull* **2004**, *37*, 27-36.
- (11) Hutchings, G. J.; Haruta, M. *Appl Catal A-Gen* **2005**, *291*, 2-5.
- (12) Zhou, S.; Jackson, G. S.; Eichhorn, B. *Adv. Funct. Mater.* **2007**, *17*, 3099-3104.
- (13) Sinfelt, J. H. *J. Catal.* **1973**, *29*, 308-315.
- (14) Sinfelt, J. H. *Surf. Sci.* **2002**, *500*, 923-946.
- (15) Fairbanks, M. C.; Benfield, R. E.; Newport, R. J.; Schmid, G. *Solid State Commun.* **1990**, *73*, 431-436.
- (16) Waychunas, G. A. *J. Mater. Sci.* **1983**, *18*, 195-207.

- (17) Rao, L. F.; Fukuoka, A.; Kosugi, N.; Kuroda, H.; Ichikawa, M. *J Phys Chem-US* **1990**, *94*, 5317-5327.
- (18) Fukuoka, A.; Kimura, T.; Kosugi, N.; Kuroda, H.; Minai, Y.; Sakai, Y.; Tominaga, T.; Ichikawa, M. *J. Catal.* **1990**, *126*, 434-450.
- (19) Ichikawa, M.; Rao, L. F.; Kimura, T.; Fukuoka, A. *J. Mol. Catal.* **1990**, *62*, 15-35.
- (20) Toshima, N.; Yonezawa, T.; Harada, M.; Asakura, K.; Iwasawa, Y. *Chem. Lett.* **1990**, 815-818.
- (21) Bao, X.; Barth, J. V.; Lehmpfuhl, G.; Schuster, R.; Uchida, Y.; Schlogl, R.; ERTL, G. *Surf. Sci.* **1993**, *284*, 14-22.
- (22) Barth, J. V.; Brune, H.; Ertl, G.; Behm, R. J. *Phys. Rev. B* **1990**, *42*, 9307-9318.
- (23) Ertl, G. *Science* **1991**, *254*, 1750-1755.
- (24) Vanhove, M. A.; Moritz, W.; Over, H.; Rous, P. J.; Wander, A.; Barbieri, A.; Materer, N.; Starke, U.; Somorjai, G. A. *Surf Sci Rep* **1993**, *19*, 191-229.
- (25) Cremer, P.; Stanners, C.; Niemantsverdriet, J. W.; Shen, Y. R.; Somorjai, G. *Surf. Sci.* **1995**, *328*, 111-118.
- (26) McIntyre, B. J.; Salmeron, M. B.; Somorjai, G. A. *Catal. Lett.* **1992**, *14*, 263-269.
- (27) Rodriguez, J. A.; Goodman, D. W. *J Phys Chem-US* **1991**, *95*, 4196-4206.
- (28) Rodriguez, J. A.; Goodman, D. W. *Surf Sci Rep* **1991**, *14*, 1-107.
- (29) Campbell, R. A.; Rodriguez, J. A.; Goodman, D. W. *Phys. Rev. B* **1992**, *46*, 7077-7087.

- (30) Bian, C. R.; Suzuki, S.; Asakura, K.; Ping, L.; Toshima, N. *J Phys Chem B* **2002**, *106*, 8587-8598.
- (31) Shiraishi, Y.; Ikenaga, D.; Toshima, N. *Aust. J. Chem.* **2003**, *56*, 1025-1029.
- (32) Bradley, J. S.; Hill, E. W.; Klein, C.; Chaudret, B.; Duteil, A. *Chem. Mater.* **1993**, *5*, 254-256.
- (33) Bradley, J. S.; Hill, E. W.; Chaudret, B.; Duteil, A. *Langmuir* **1995**, *11*, 693-695.
- (34) Bradley, J. S.; Millar, J. M.; Hill, E. W.; Klein, C.; Chaudret, B.; Duteuil, A.; Geus, J. W.; Joyner, R. W.; Fouilloux, P.; Sermon, P. A.; Ichikawa, M.; Bozonverduraz, F. *Stud. Surf. Sci. Catal.* **1993**, *75*, 969-979.
- (35) Bradley, J. S.; Via, G. H.; Bonneviot, L.; Hill, E. W. *Chem. Mater.* **1996**, *8*, 1895-1903.
- (36) Ye, H.; Crooks, R. M. *J. Am. Chem. Soc.* **2007**, *129*, 3627-3633.
- (37) Scott, R. W. J.; Wilson, O. M.; Oh, S. K.; Kenik, E. A.; Crooks, R. M. *J. Am. Chem. Soc.* **2004**, *126*, 15583-15591.
- (38) Knecht, M. R.; Weir, M. G.; Frenkel, A. I.; Crooks, R. M. *Chem. Mater.* **2008**, *20*, 1019-1028.
- (39) Li, Y.; El-Sayed, M. A. *J Phys Chem B* **2001**, *105*, 8938-8943.
- (40) Narayanan, R.; El-Sayed, M. A. *Nano Lett.* **2004**, *4*, 1343-1348.
- (41) Narayanan, R.; El-Sayed, M. A. *J Phys Chem B* **2005**, *109*, 12663-12676.
- (42) Sra, A. K.; Schaak, R. E. *J. Am. Chem. Soc.* **2004**, *126*, 6667-6672.

- (43) Schaak, R. E.; Sra, A. K.; Leonard, B. M.; Cable, R. E.; Bauer, J. C.; Han, Y. F.; Means, J.; Teizer, W.; Vasquez, Y.; Funck, E. S. *J. Am. Chem. Soc.* **2005**, *127*, 3506-3515.
- (44) Park, J. I.; Cheon, J. *J. Am. Chem. Soc.* **2001**, *123*, 5743-5746.
- (45) Lee, W. R.; Kim, M. G.; Choi, J. R.; Park, J. I.; Ko, S. J.; Oh, S. J.; Cheon, J. *J. Am. Chem. Soc.* **2005**, *127*, 16090-16097.
- (46) Seo, J. W.; Jun, Y. W.; Ko, S. J.; Cheon, J. *J Phys Chem B* **2005**, *109*, 5389-5391.
- (47) Bratlie, K. M.; Lee, H.; Komvopoulos, K.; Yang, P.; Somorjai, G. A. *Nano Lett.* **2007**, *7*, 3097-3101.
- (48) Park, J. Y.; Zhang, Y.; Grass, M.; Zhang, T.; Somorjai, G. A. *Nano Lett.* **2008**, *8*, 673-677.
- (49) Zhang, Y.; Huang, W.; Habas, S.; Kuhn, J. N.; Grass, M. E.; Yamada, Y.; Yang, P.; Somorjai, G. A. *J. Phys. Chem. C* **2008**, *112*, 12092-12095.
- (50) Kim, S.; Yin, Y.; Alivisatos, A.; Somorjai, G. A.; Yates, J. T. *J. Am. Chem. Soc.* **2007**, *129*, 9510-9513.
- (51) Murray, C. B.; Kagan, C. R.; Bawendi, M. G. *Annu Rev Mater Sci* **2000**, *30*, 545-610.
- (52) Bonnemann, H.; Richards, R. M. *Eur J Inorg Chem* **2001**, 2455-2480.
- (53) Reetz, M. T.; Helbig, W.; Quaiser, S. A. *Chem. Mater.* **1995**, *7*, 2227-&.
- (54) Kolb, U.; Quaiser, S. A.; Winter, M.; Reetz, M. T. *Chem. Mater.* **1996**, *8*, 1889-1894.

- (55) Fan, F.; Liu, D.; Wu, Y.; Duan, S.; Xie, Z.; Jiang, Z.; Tian, Z. *J. Am. Chem. Soc.* **2008**, *130*, 6949-+.
- (56) Cable, R.; Schaak, R. *Chem. Mater.* **2007**, *19*, 4098-4104.
- (57) Vasquez, Y.; Luo, Z.; Schaak, R. *J. Am. Chem. Soc.* **2008**, *130*, 11866-11867.
- (58) Wang, Y.; Toshima, N. *J Phys Chem B* **1997**, *101*, 5301-5306.
- (59) Lim, B.; Wang, J.; Camargo, P.; Jiang, M.; Kim, M. J.; Xia, Y. *Nano Lett.* **2008**, *8*, 2535-2540.
- (60) Habas, S. E.; Lee, H.; Radmilovic, V.; Somorjai, G. A.; Yang, P. *Nat Mater* **2007**, *6*, 692-697.
- (61) Zhou, S. H.; Varughese, B.; Eichhorn, B.; Jackson, G.; McIlwrath, K. *Angew Chem Int Edit* **2005**, *44*, 4539-4543.
- (62) Nashner, M. S.; Frenkel, A. I.; Somerville, D.; Hills, C. W.; Shapley, J. R.; Nuzzo, R. G. *J. Am. Chem. Soc.* **1998**, *120*, 8093-8101.
- (63) Alayoglu, S.; Nilekar, A.; Mavrikakis, M.; Eichhorn, B. *Nat Mater* **2008**, *7*, 333-338.
- (64) Pecharsky, V. K.; Zavalij, P. Y. *Fundamentals of Powder Diffraction and Structural Characterization of Materials*; Springer: 2009;
- (65) Yan, W. F.; Petkov, V.; Mahurin, S. M.; Overbury, S. H.; Dai, S. *Catal Commun* **2005**, *6*, 404-408.
- (66) Sanchez-Escribano, V.; Arrighi, L.; Riani, P.; Marazza, R.; Busca, G. *Langmuir* **2006**, *22*, 9214-9219.
- (67) Zhou, W.; Lewera, A.; Bagus, P. S.; Wieckowski, A. *J. Phys. Chem. C* **2007**, *111*, 13490-13496.

- (68) Kowal, A.; Li, M.; Shao, M.; Sasaki, K.; Vukmirovic, M. B.; Zhang, J.; Marinkovic, N. S.; Liu, P.; Frenkel, A. I.; Adzic, R. R. *Nat Mater* **2009**, *8*, 325-330.
- (69) Amekura, H.; Kono, K.; Takeda, Y.; Kishimoto, N. *Appl. Phys. Lett.* **2005**, *87*, 153105.
- (70) Shriver, D. F.; Atkins, P. W. *Inorganic Chemistry*; W.H. Freeman and Company: New York, 2000;
- (71) Choudhary, T. V.; Sivadinarayana, C.; Chusuei, C. C.; Datye, A. K.; Fackler, J. P.; Goodman, D. W. *J. Catal.* **2002**, *207*, 247-255.
- (72) Herrera, J. E.; Balzano, L.; Borgna, A.; Alvarez, W. E.; Resasco, D. E. *J. Catal.* **2001**, *204*, 129-145.
- (73) Wu, Z.; Zhou, S.; Zhu, H.; Dai, S.; Overbury, S. H. *J. Phys. Chem. C* **2009**, *113*, 3726-3734.
- (74) Liu, R. X.; Iddir, H.; Fan, Q. B.; Hou, G. Y.; Bo, A. L.; Ley, K. L.; Smotkin, E. S.; Sung, Y. E.; Kim, H.; Thomas, S.; Wieckowski, A. *J Phys. Chem. B* **2000**, *104*, 3518-3531.
- (75) Stencel, J. M. *Raman Spectroscopy for Catalysis*; Van Nostrand Reinhold: New York, 1990;
- (76) Pan, X.; Fan, Z.; Chen, W.; Ding, Y.; Luo, H.; Bao, X. *Nat Mater* **2007**, *6*, 507-511.
- (77) Borodko, Y.; Habas, S.; Koebel, M.; Yang, P.; Frei, H.; Somorjai, G. A. *J Phys Chem B* **2006**, *110*, 23052-23059.

- (78) Borodko, Y.; Humphrey, S. M.; Tilley, T. D.; Frei, H.; Somorjai, G. A. *J. Phys. Chem. C* **2007**, *111*, 6288-6295.
- (79) Hammer, B.; Norskov, J. K. *Surf. Sci.* **1995**, *343*, 211-220.
- (80) Hammer, B.; Morikawa, Y.; Norskov, J. K. *Phys. Rev. Lett.* **1996**, *76*, 2141-2144.
- (81) Nilekar, A. U.; Mavrikakis, M. *Surf. Sci.* **2008**, *602*, L89-L94.
- (82) Ferrando, R.; Jellenik, J.; Johnston, R. L. *Chem. Rev.* **2008**, *108*, 845-910.

## Chapter 2: Nanoparticle Stabilizer Effects on Heterogeneous Catalytic Transformations

### 2.1 Introduction

Metallic nanoparticles (NPs) have been used for heterogeneous chemical transformations for more than 100 years due to their high surface area and their anomalous activities.<sup>1</sup> Interest in the preparation of new NPs for heterogeneous catalysis remains intense due to one's ability to control NP shape, size, composition and architecture during synthesis. All of these factors can strongly affect selectivity and activity in many reactions.<sup>2-5</sup>

Historically, the preparation of metallic NP catalysts primarily involved impregnating a porous support ( $\text{SiO}_2$ ,  $\text{Al}_2\text{O}_3$ ,  $\text{CeO}_2$  or graphite) with precious metal salts and subsequently reducing the metal cation to its elemental state.<sup>6</sup> This simple but effective method led to the empirical development of a plethora of monometallic, bimetallic and multimetallic systems that account for a large portion of the materials used by the catalysis industry today.<sup>2, 7</sup> These supported NP systems are used for a large number of solution phase and gas phase transformations that include hydrocarbon reforming,<sup>8</sup> small molecule oxidations,<sup>5, 9</sup> and a variety of organic transformations.<sup>4, 7, 10, 11</sup> However, further advances in catalyst development that link theory and NP design will require more sophisticated NP synthetic protocols; especially for bimetallic and multimetallic systems.<sup>12</sup>

While the impregnation methods lead to less contamination of NP surfaces, these methods afford only limited control over NP structure and dispersity. For

example, the formation of complex architectures such as shape-controlled particles,<sup>13,14</sup> rods, tubes, core-shell structures, and contact aggregates is difficult to achieve by way of impregnation and usually requires the use of prefabricated nanostructures. Implementing control over NP synthetic procedures usually involves the use of surfactants and / or stabilizers to control various aspects of particle growth and nucleation processes. These large organic molecules and polymers, such as oleylamine and polyvinylpyrrolidone (PVP), coat the resulting NPs. In many cases, stabilizers are used in huge excess and can constitute up to 50 wt. % of the washed and dried NP product.<sup>15</sup>

The presence of these stabilizers motivates the need to determine stabilizer effects on NP activity and, if necessary, protocols for removing the stabilizer coatings should the coatings prove detrimental to catalytic performance. In principle, stabilizers bound to NPs can occupy active sites and have the potential to impact negatively a NPs catalytic performance.<sup>10, 16-19</sup> An example of such an effect was reported by El-Sayed and co-workers, who showed that a balance between colloidal NP stability (strong NP-ligand interaction) and surface access (weak NP-ligand interaction) must be achieved for the best long-term performance.<sup>20</sup> Similarly, Nikles and coworkers showed that oleylamine and oleic acid used to stabilize Pt<sub>3</sub>Sn NPs rendered the NPs inactive for use as methanol oxidation electrocatalysts. Only by performing a ligand exchange with a smaller and less strongly bound stabilizer, tetramethylammonium hydroxide, was electrocatalytic activity observed.<sup>21, 22</sup> However, Borchert<sup>23</sup> and Bratlie<sup>16</sup> have shown that heterogeneous reactions can proceed on Pt NPs without removing the

stabilizers. Surprisingly, stabilizers have also been shown to enhance the selectivity of certain organic transformation reactions. For example, Bradley and coworkers reported a selectivity enhancement for the hydrogenation of 2-hexyne on PVP coated Pt NPs in a mixed-metal oxide support compared to PVP-free catalysts.<sup>24</sup>

Interpreting these results in a consistent and predictive way is not straightforward. The stabilizers themselves can undergo chemical change that may affect catalytic activity in unknown ways. Somorjai and co-workers have shown how PVP degrades at elevated temperatures leaving behind amorphous carbon deposits.<sup>25</sup> Using resonance enhanced Raman spectroscopy, their studies provided detailed insight into the mechanisms responsible for PVP degradation and resulting graphite formation. Missing from these studies of PVP degradation is an analysis about how (or if) the resulting graphitic products affect NP catalytic activity. While conventional wisdom assumes that protecting agents need to be removed prior to use in heterogeneous applications, the actual effects of PVP stabilizers and their degradation products have not been described in a thorough and systematic manner. The work presented in this paper describes how the conditioning of PVP-protected Pt NPs impacts NP-catalyzed propylene hydrogenation. Specifically, we show that PVP-derived, graphite-like deposits formed during catalytic propene hydrogenation do not impede catalytic activity. In contrast, graphite-like deposits formed from annealing PVP coated NPs under non-oxidizing atmospheres ( $N_2$  or  $H_2$ ) without catalysis significantly diminishes catalytic performance. The ramifications of these results in catalyst conditioning

are discussed.

## 2.2 Experimental

### **2.2.1 Synthesis of Platinum Nanoparticles**

Pt nanoparticles were prepared using a modified synthesis previously reported by Bradley.<sup>26</sup> In a representative synthesis, PVP (55000 MWT) (50 mg, 0.45 mmol) and 15 mL of ethylene glycol (EG) were added to a round bottom flask, stirred under N<sub>2</sub> atmosphere and heated to 170 °C. In a separate flask, Pt(acac)<sub>2</sub> (78.7 mg, 0.20 mmol) was added to 5 mL of EG and stirred until the metal salt precursor was dissolved. The metal salt solution was then rapidly injected into the hot EG/PVP mixture. The solution instantly turned dark brown/black, a distinctive signature of colloid formation. The colloid was stirred and heated to 180 °C for 2 hours under N<sub>2</sub>, quickly cooled to room temperature in an ice bath and washed 3 times with acetone and 2 times with ethanol to remove excess PVP and other byproducts. With each washing, the supernatant and the precipitate were separated by centrifugation. This procedure led to Pt NPs of 7-8 nm in diameter (TEM analysis). XRD analysis showed only the broad Pt diffraction peaks.

### **2.2.2 Preparation of Catalyst Materials**

A 0.1% loaded catalyst (0.1% Pt by weight) was prepared by adding 999 mg  $\gamma$ -Al<sub>2</sub>O<sub>3</sub> to ~ 20 mL of EG and stirred until a slurry was formed. 513  $\mu$ L of the Pt colloid was then added drop-wise to the rapidly stirring alumina/EG slurry. The solvent was removed by gentle heating under vacuum and the remaining solid

was washed with acetone followed by centrifugation. The acetone washing procedure was repeated 4 times.

### **2.2.3 TGA Analysis**

A Thermal Advantage Q500 was used for TGA analysis. For NPs, approximately 1 mg of the dried and the washed sample was loaded into a platinum weighing boat. The samples were treated at 115 °C in N<sub>2</sub> before experiments were run. In a typical experiment, the samples were allowed to equilibrate at room temperature for 15 minutes under either N<sub>2</sub> or air.

### **2.2.4 Raman Experiments**

A Renishaw In Via micro-Raman spectrometer was used to acquire vibrational spectra. The spectrometer is equipped with a 633 nm HeNe laser as well as a 488 nm Ar ion laser, and both operated with powers between 2.5 to 25 mW with a minimum spot size of ~1 mm. Sample focusing was optimized with 50X confocal lens objective adapted to a Leica microscope. NP samples were prepared by pressing ~5 mg of washed and dried nanoparticle powders onto aluminum foil substrates. Typical collection times for Raman measurements were 2-10 minutes in open air.

### **2.2.5 CO Titration Experiments**

Prior to carbon monoxide adsorption measurements, the catalysts were reduced under flowing hydrogen at atmospheric pressure at either 50 °C or 200 °C, followed by evacuation at the same temperature. The carbon monoxide adsorption uptakes were measured at 22 °C on a standard gas adsorption apparatus described elsewhere.<sup>27</sup>

### **2.2.6 Catalysis Experiments**

100 mg of the Al<sub>2</sub>O<sub>3</sub>-supported Pt NP catalyst was mixed with 140 mg of quartz beads and loaded into a reacting flow tube with an inner diameter of 0.147 in run at a constant velocity of 0.0985 m/s (200 sccm). All gas flows were controlled with calibrated mass flow controllers and the products were monitored using a Thermo Prima δB mass spectrometer. The propene hydrogenation reaction was set to ramp at 3 °C/min up to 220 °C and then held until steady state conversion values were reached. Before catalysis experiments were run, a mixture of 27.1% H<sub>2</sub> and 72.9% N<sub>2</sub> was passed over the catalyst at 24 °C for 20 minutes. In all experiments, a mixture of 3.2% propene, 27.1% hydrogen with N<sub>2</sub> balance was used. All gases were purchased from Airgas and were of ultra high purity grade. Percent conversion of propene was calculated by monitoring the main carbon fragments of propane and propene (mass 42 and 44) over the course of the experiment using the mass spectrometer. These values were compared to a calibration curve made using a mixture of propane and propene at various concentrations. The details of our catalysis setup are reported elsewhere.<sup>28</sup> Steady state conversion values are determined after approximately 2 hours of operation at 220 °C.

### **2.2.7 TEM Analysis**

TEM images of nanoparticles and catalysts were acquired using a JEOL 2100 JEM electron microscope operating at 200 kV. The colloidal suspensions of nanoparticles were sufficiently diluted with water and a drop of this solution was placed on a copper/carbon mesh grid and allowed to air dry. Catalyst samples for

TEM were prepared by similar dilution and deposition on the surface of a copper/carbon mesh grid.

## 2.3 Results and Discussion

### **2.3.1 Platinum Nanoparticle Properties**

Figure 2.1 shows TEM images of 7-8 nm Pt NPs used to prepare the 0.1% Pt/Al<sub>2</sub>O<sub>3</sub> catalyst. Acquiring TEM images of the 0.1% catalyst proved difficult due to high dilution factor (images are included in supporting information 2.1).

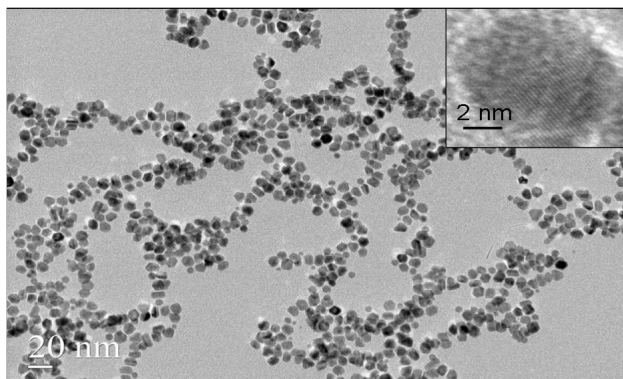


**Figure 2.1** TEM image of 8 nm Pt nanoparticles used to prepare the 0.1% Pt/Al<sub>2</sub>O<sub>3</sub> catalyst.

The use of a 2:1 PVP (monomer unit):Pt ratio provided monodisperse NPs with mostly hexagonal shapes that are associated with cubeoctahedral particles.<sup>1316</sup> These results are consistent with those of other similar PVP/glycol syntheses.<sup>19</sup> The slightly larger size regime reported here is due to a smaller PVP:Pt<sup>2+</sup> ratio.

TGA data from unsupported Pt NPs used to prepare subsequent 0.1% loaded catalysts are presented in Figure 2.2. Significant mass losses beginning at 160 and 180 °C for air and N<sub>2</sub> atmospheres, respectively, are observed even after the multiple washings described in the experimental section. This result implies that the washed NPs remain coated with PVP, which thermally decomposes in the

TGA experiment. The finding is consistent with prior results reported by Du and

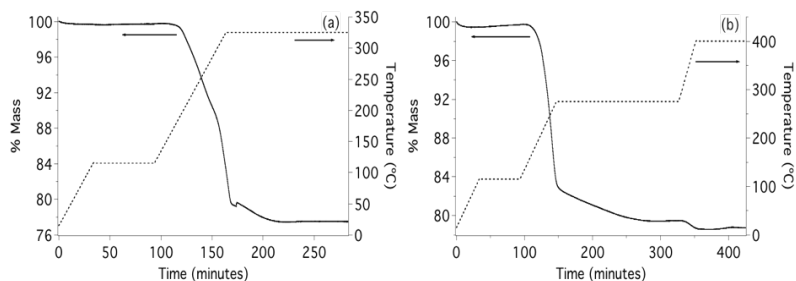


**Figure 2.2** TGA in (a) N<sub>2</sub> atmosphere and (b) air atmosphere of unsupported Pt NPs from the same synthetic batch. Samples were previously dried at 115 °C for 2 hours before TGA experiments.

coworkers.<sup>15</sup> Pure PVP thermally degrades at 375 °C (data not shown). The significantly lower temperatures associated with PVP mass loss on the NP illustrate the role played by Pt NPs in activating C-C and C-H bonds. Over the course of three hours at relatively low temperature (275 °C) in air, oxidation removes the majority of PVP on Pt NPs. Raman spectra of the post-TGA NPs show that all PVP and its degradation products were removed after conditioning at

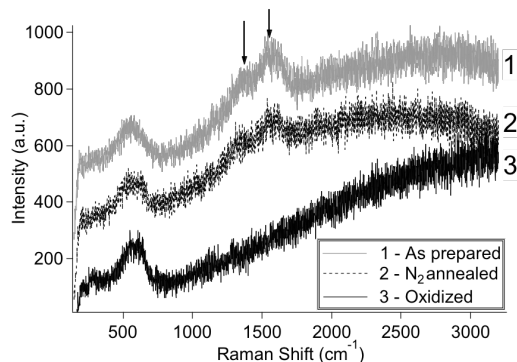


**Figure 2.3** Room temperature Raman spectra (488 nm excitation) of Pt NPs acquired before and after TGA. The peak at 520 cm<sup>-1</sup> is due to surface Pt oxide. The D and G bands typical of graphitic structure are indicated by vertical arrows.

275 °C in air (Figure 2.3). Interestingly, similar mass loss is observed for particles heated under N<sub>2</sub> (Figure 2.2) but carbon clearly remains on the NPs given the clear graphite signature appearing in the Raman spectra of the N<sub>2</sub> conditioned particles

(Figure 2.3). In contrast, Raman spectra of as-prepared NPs recorded at low power (not shown in Fig. 2.3) reveal intact PVP units without graphite deposits. The Raman spectrum recorded at high power degrades the PVP such that both the as-prepared and N<sub>2</sub> conditioned Pt NPs show bands in the 1300-1600 cm<sup>-1</sup> region (Figure 3). These bands are commonly referred to as the D and G bands of graphite.<sup>29</sup> Somorjai and coworkers have shown that UV laser light couples strongly with darkly colored NP samples and can thermally degrade PVP on the surface of Pt NPs.<sup>25, 30</sup> Importantly, the D and G bands observed for the N<sub>2</sub> annealed sample indicate that significant graphite-like deposits persist after the 325 °C inert atmosphere conditioning. Low power Raman spectra of the unsupported, N<sub>2</sub> annealed particles show graphite to be present, even under conditions that leave the PVP polymer intact on the as-prepared particles. El-Sayed and coworkers demonstrated that chemisorbed polymer exists even after high vacuum treatment at 310 C.<sup>31</sup> No such D and G structure is seen for the air-oxidized Pt NP sample indicating a surface that is free of carbonaceous deposits. The band appearing at ~520 cm<sup>-1</sup> in all three spectra likely reflects the phonon mode of surface Pt oxide.<sup>32</sup>

### 2.3.2 Catalysis

Having identified the conditions that lead both to clean (carbon free) NPs and to NPs coated with PVP and graphite, our next goal was to determine what effects – if any – these conditioning procedures had on NP catalytic activity. The hydrogenation of propene was selected as the benchmark reaction due to the reaction's well characterized mechanisms, rate constants and thermodynamic

properties.<sup>31, 33</sup> Furthermore, the intermediate size of propene was anticipated to make this reaction more sensitive to the steric accessibility of active NP surface sites.

Figure 2.4 shows a reaction profile vs. time for the propene hydrogenation reaction using a single loaded catalyst sample. The sequence of experiments was as follows: a 0.1% loaded catalyst was used without any conditioning and the percent conversion of propene to propane was monitored. Following the approach

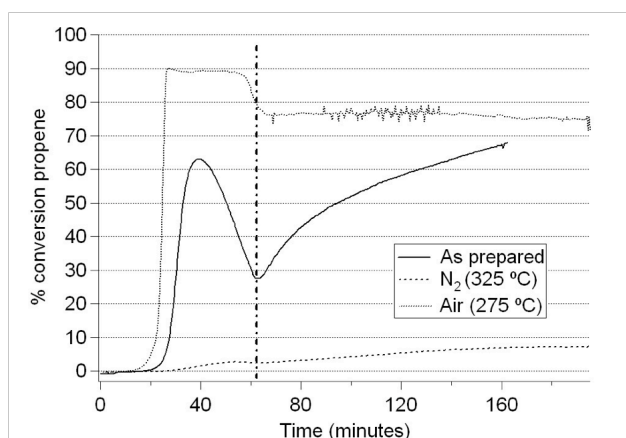


**Figure 2.4** A typical reaction profile of propene hydrogenation. A ramp rate of 3 °C/min was used to reach the equilibrium temperature of 220 °C. The dashed vertical line indicates when 220 °C was reached.

to steady state, the sample was conditioned under N<sub>2</sub> at 325 °C for 3 hours, cooled to room temperature under N<sub>2</sub> and the propene hydrogenation reaction was run again. Finally, the catalyst was subjected to an air-oxidation step at 275 °C for 4 hours. This temperature corresponded to the minimum temperature needed for complete removal of carbon. The N<sub>2</sub> and air oxidations were intended to mimic the conditions used on unsupported NPs to generate the data shown in Figures 2.2 (TGA) and 2.3 (Raman).

Surprisingly, both the as-prepared and oxidized catalysts ultimately

showed similar conversion efficiencies (Figure 2.4). For the as-prepared catalyst, an initial light-off temperature of 85 °C is observed and approximately 2 hours is required to reach steady state conversion of ~70%. Such a long stabilization time suggests that the reactant gases along with the elevated temperatures are slowly enhancing surface activity. The activity improvement could be due to particle surface restructuring or improved gas phase transport to the particle surface. Clearly graphite-like deposits are present, however, because when the catalyst is cooled, conditioned under N<sub>2</sub> (at 325°C for 3 hrs.), and brought back to room temperature, a new reaction profile shows that hydrogenation conversion efficiency drops to < 10%. Such behavior is consistent with the idea that annealing the particles under N<sub>2</sub> leads to a dense, impermeable graphitic layer that coalesces around the NPs, effectively blocking most of the active surface sites. This picture is supported by the Raman data that show graphite formation on the unsupported particles annealed under N<sub>2</sub> (Figure 2.3). Note that catalysts annealed directly at 325 °C without running propene hydrogenation resulted in the same deactivation. Subjecting the NPs to an oxidizing conditioning step at 275 °C in air for 4 hours (the minimum temperature needed for complete removal of carbon based on TGA data) led to a 65 °C light-off temperature and no lag time to ~75% steady-state conversion.

This sequence of as-prepared, N<sub>2</sub> annealed, and oxidized experiments was evaluated at least three times with fresh catalyst charges prepared from independent syntheses. A plot of the steady-state conversion rates is presented in Figure 2.5, and specific values for conversions in each separate run are shown in

supporting information (Supp. Info. 2.2). The 0.1% Pt / Al<sub>2</sub>O<sub>3</sub> catalyst was first run without any prior conditioning apart from the washing procedures described in

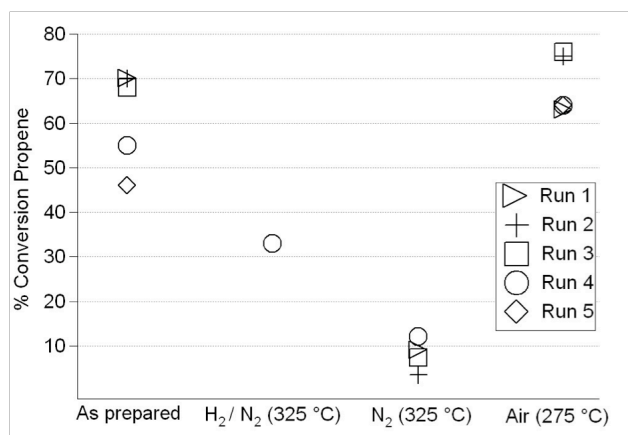


**Figure 2.5** Scatter plot of steady state conversion values of individual runs for propene hydrogenation at 220 °C under different conditioning atmospheres. See text for details. Run number refers to Table S2.1.

The experimental section. Conversion efficiencies showed some spread for catalysts using the as-prepared particles ( $62 \pm 10\%$ ), but data from the N<sub>2</sub> annealed ( $9 \pm 3\%$ ) and oxidized particles ( $63 \pm 2\%$ ) had very high precision. One interesting initial observation from all of these experiments was that little or no conversion occurred at the low temperatures normally reported for propene hydrogenation catalysts.<sup>33</sup> The relatively high flow rates employed in our flow through reactor presumably dissipate the heat of reaction more readily compared to similar reactions run in batch reactors.<sup>28</sup>

Given the reproducibility of this cycle – highest conversion with both as-prepared and fully cleaned catalysts and poor conversion with those same catalysts treated with N<sub>2</sub> at higher temperatures – we sought to better understand the relationship between graphite formation and catalytic activity. We again ran the as-prepared catalyst and observed a steady state conversion efficiency of 55% and

then turned off the propene. The catalyst was treated with a mixture of 27% H<sub>2</sub> and 73% N<sub>2</sub> at 325 °C for 4 hours. Condition in the absence of both H<sub>2</sub> and propene generates catalysts that have propene hydrogenation conversion efficiencies below 10%. The reducing environment treatment diminished the performance of the as-prepared catalyst from 55% to 33% conversion but did not poison the surface as effectively as in the case of the N<sub>2</sub>-annealed catalyst. After the reducing treatment, the catalyst was subjected to the same N<sub>2</sub> annealing as discussed previously. The conversion dropped to 12% after this treatment. Finally, the catalyst was oxidized in air at 275 °C for 2 hours. A steady state conversion of 65% was achieved. This sequence is presented in Figure 2.5 as Run 4.

To determine if the intermediate N<sub>2</sub> annealing step itself caused any hindrance to further PVP oxidation, the N<sub>2</sub> annealing step was removed and an as-prepared catalyst was oxidized directly. However, the observations are sequence independent, as the overall conversion of propene remained the same after oxidative conditioning. This result is denoted as run 5 in Figure 2.5.

A number of observations from these experiments stand out. First, catalysts that have been conditioned under an inert atmosphere show conversion efficiencies that are much smaller than those shown by carbon-free catalysts and as-prepared catalysts. Second, the steady state conversion efficiencies of the cleaned catalysts and as-prepared catalysts are comparable, despite the presence of persistent carbon deposits on the unconditioned catalysts. Third, the unconditioned catalysts do not approach their steady state limit monotonically.

Rather, efficiency rises asymptotically until the steady-state limit is reached. Finally, the presence of H<sub>2</sub> appears to keep high temperature conditionings from significantly deactivating the catalyst. Only inert environments (N<sub>2</sub>) lead to high temperature deactivation of catalyst activity, even when the original catalyst prior to annealing showed steady state conversions that were ~10-fold higher.

Using the CO chemisorption data and the average Pt NP size, one can calculate the catalytically active surface area and total projected Pt surface area, respectively (Table 2.1). In addition, one can estimate the % CO coverage of the

experiment	catalyst treatment	chemisorbed CO ( $\mu\text{mol CO/g catalyst}$ )	TOF ( $\text{s}^{-1}$ ) <sup>c</sup>	steady state conversion (average %) <sup>d</sup>	fractional CO coverage (mol CO/mol Pt sites) <sup>e</sup>
1 <sup>a</sup>	air, 275 °C	1.7	106-128	69	0.21
2 <sup>b</sup>	air, 275 °C	1.7	106-128	69	0.21
3 <sup>b</sup>	N <sub>2</sub> , 325 °C	0.13	52	8	0.016
4 <sup>b</sup>	as synthesized	4.10	43	62	0.51

**Table 2.1** CO chemisorption data for 1% Pt/Al<sub>2</sub>O<sub>3</sub> and TOF data for 0.1% Pt/Al<sub>2</sub>O<sub>3</sub>. <sup>a</sup> preconditioned at 200 °C for 2 hours in H<sub>2</sub>. <sup>b</sup> preconditioned at 50 °C for 2 hours in H<sub>2</sub>. <sup>c</sup> calculated from average % conversion and sites determined from CO chemisorption data normalized to 1.0% loading. <sup>d</sup> average steady state conversion values for 0.1% Pt/Al<sub>2</sub>O<sub>3</sub> catalyst. <sup>e</sup> calculated from CO chemisorption data normalized to 1.0% loading and projected surface area of 1% Pt/Al<sub>2</sub>O<sub>3</sub>. Projected surface area for 1% Pt/Al<sub>2</sub>O<sub>3</sub> catalyst using 8 nm Pt NP model is 8.1  $\mu\text{mol surface Pt/g catalyst}$ .

surface Pt sites by dividing the measured chemisorption surface area by the projected surface area. This measurement provides an indication of the fraction of surface Pt sites that are catalytically active. Finally, the activity per surface Pt atom (the turnover frequency, TOF) has been calculated from the rate of product formation and the number of catalytically active Pt sites determined from the chemisorption experiments. These data are summarized in Table 2.1 along with the average steady-state conversions described in the previous section. Since all catalysts have the same size Pt NPs and therefore the same projected Pt surface

areas, the differences in steady state conversion rates can be attributed to variations in available Pt surface sites and/or the activity of the surface Pt sites.

Surprisingly, the as-prepared catalysts have an active Pt surface area of 0.41  $\mu\text{mol Pt/g catalyst}$ , which is more than twice that of the air-oxidized catalysts (0.17  $\mu\text{mol Pt/g catalyst}$ ). The high surface area persists despite the presence of significant carbonaceous deposits identified by the Raman experiments. Annealing the as-prepared catalysts under  $\text{N}_2$  decreases the amount of surface active Pt sites by more than 10 fold (0.013  $\mu\text{mol Pt/g catalyst}$ ). Annealing the  $\text{N}_2$  annealed samples in air at 275  $^\circ\text{C}$  restores 50% of the original active surface area and is equal to that of the directly air-annealed sample (0.17  $\mu\text{mol Pt/g catalyst}$ ).

The TOF's of the as-prepared and  $\text{N}_2$ -annealed catalysts are very similar suggesting that the activity of the available surface Pt sites is the same. However, the TOF's for the air-annealed samples are consistently twice as high as the other two catalysts (Table 2.1). There may be several possibilities for the increased activity, such as enhanced metal-support interactions, superior gas diffusion rates or surface restructuring (shape modification) of the Pt NPs. Although the TOF's of the as-prepared catalysts are  $\sim 50\%$  less than the air-annealed samples, their surface area are  $\sim 50\%$  higher, which gives the two catalysts similar steady state conversion efficiencies.

These results strongly suggest that the reactive atmosphere present during propene hydrogenation of the as-prepared NPs generates loosely-associated carbonaceous deposits that do not significantly inhibit catalytic performance. In the absence of this reactive atmosphere, the existing carbon coalesces at high

temperatures and effectively blocks access to catalytically active Pt surface sites. The amount of residual carbon surrounding the N<sub>2</sub> annealed NPs is relatively small given that unsupported particles show similar mass loss in the TGA experiments (Figure 2.2), regardless of whether they were heated in inert (N<sub>2</sub>) or oxidizing (air) environments. Finally, when all carbonaceous deposits are removed by air-oxidation, relatively high conversion efficiencies and large accessible areas are again observed. Collectively these observations show that the presence of graphite-like carbon deposits is not necessarily detrimental to catalytic activity, but rather, the catalyst performance will be affected by the location of any carbon present and perhaps by the strength of the graphic carbon-metal interactions. A recent study by Matsumura and coworkers lends support to this idea. In experiments where the amount of carbon surrounding a Pt NP was carefully controlled, these researchers showed that high density carbon shells lowered the activity of decene hydrogenation compared similar Pt NPs coated with low density carbon.<sup>34</sup>

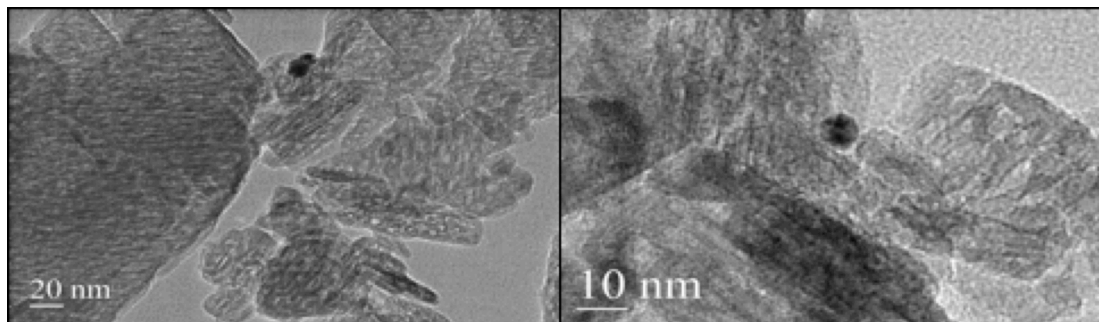
## 2.4 Summary

We have shown that under steady state conditions, PVP degradation to graphite-like carbon does not necessarily hinder heterogeneous transformations of even "medium" sized molecules such as propene. However, densifying the residual carbon through inert gas annealing will significantly diminish catalyst performance. Oxidative removal of the residual graphite-like deposits restores the activity back to that of the conditioned as-prepared catalysts. Both air-oxidized and N<sub>2</sub> annealed catalysts show consistent, time-independent behavior whereas

unconditioned catalysts require longer times to reach steady state performance.

High temperature, inert atmosphere conditioning is clearly deleterious to catalytic performance as evidenced by the low conversion values and high light-off temperatures. We propose that a thin, dense carbonaceous layer is forming under these inert conditions and that this carbon blocks catalytically active sites. This hypothesis is corroborated by Raman spectra that show D and G bands associated with PVP degradation and CO chemisorption data that shows significantly lower surface areas on inert atmosphere annealed NPs compared to both as-prepared and air-oxidized NPs.

## 2.5 Supplemental Information



**Supplemental Information 2.1** TEM images of 0.1% Pt/Al<sub>2</sub>O<sub>3</sub> catalyst before (left) and after (right) catalysis and conditioning.

Sequence of conditioning events	Time (hours) / conditioning temperature (°C)	Run 1 (% Conv.)	Run 2 (% Conv.)	Run 3 (% Conv.)	Run 4 (% Conv.)	Run 5 (% Conv.)	Average / S.D.
As-prepared	N/A	70	70	68	46	55	61.8 / 9.7
H <sub>2</sub> /N <sub>2</sub> (27%/73%) anneal	4 / 325	N/A	N/A	N/A	N/A	33	N/A
N <sub>2</sub> anneal	4 / 325	9	4	7	N/A	12	8 / 2.9
Air oxidation	2 / 275	63	75	76	64	65	68.6 / 6.3

**Supplemental information 2.2** Sequential conditioning conversion efficiencies for propene hydrogenation reaction over 0.1% Pt/Al<sub>2</sub>O<sub>3</sub>.

## 2.6 References

- (1) Schmid, G.; Baumle, M.; Geerkens, M.; Helm, I.; Osemann, C.; Sawitowski, T. *Chem. Soc. Rev.* **1999**, *28*, 179-185.
- (2) Bell, A. T. *Science* **2003**, *299*, 1688-1691.
- (3) Bond, G. C.; Thompson, D. T. *Catal. Rev.-Sci. and Eng.* **1999**, *41*, 319-388.
- (4) Enache, D. I.; Edwards, J. K.; Landon, P.; Solsona-espriu, B.; Carley, A. F.; Herzing, A. A.; Watanabe, M.; Kiely, C. J.; Knight, D. W.; Hutchings, G. J. *Science* **2006**, *311*, 362-365.
- (5) Valden, M.; Lai, X.; Goodman, D. W. *Science* **1998**, *281*, 1647-1650.
- (6) Sinfelt, J. H.; Via, G. H. *J. Catal.* **1979**, *56*, 1-11.
- (7) Coq, B.; Kumbhar, P. S.; Moreau, C.; Moreau, P.; Figueras, F. *J. Phys. Chem.* **1994**, *98*, 10180-10188.
- (8) Bonnemann, H.; Brijoux, W.; Brinkmann, R.; Dinjus, E.; Jousen, T.; Korall, B. *Angew. Chem.-Int. Ed.* **1991**, *30*, 1312-1314.
- (9) Haruta, M. *Catal. Today* **1997**, *36*, 153-166.
- (10) Song, H.; Rioux, R. M.; Hoefelmeyer, J. D.; Komor, R.; Niesz, K.; Grass, M.; Yang, P. D.; Somorjai, G. A. *J. Am. Chem. Soc.* **2006**, *128*, 3027-3037.
- (11) Toshima, N.; Wang, Y. *Advan. Mater.* **1994**, *6*, 245-247.
- (12) Toshima, N.; Yonezawa, T. *New J. Chem.* **1998**, *22*, 1179-1201.
- (13) Rioux, R. M.; Song, H.; Grass, M.; Habas, S.; Niesz, K.; Hoefelmeyer, J. D.; Yang, P.; Somorjai, G. A. *Topics in Catal.* **2006**, *39*, 167-174.
- (14) Grass, M.; Yue, Y.; Habas, S.; Rioux, R.; Teall, C.; Yang, P.; Somorjai, G. *J. Phys. Chem. C* **2008**, *112*, 4797-4804.

- (15) Du, Y. K.; Yang, P.; Mou, Z. G.; Hua, N. P.; Jiang, L. *J. Appl. Polym. Sci.* **2006**, *99*, 23-26.
- (16) Bratlie, K. M.; Lee, H.; Komvopoulos, K.; Yang, P.; Somorjai, G. A. *Nano Letters* **2007**, *7*, 3097-3101.
- (17) Konya, Z.; Molnar, E.; Tasi, G.; Niesz, K.; Somorjai, G. A.; Kiricsi, I. *Catal. Lett.* **2007**, *113*, 19-28.
- (18) Lee, H.; Habas, S. E.; Kwestin, S.; Butcher, D.; Somorjai, G. A.; Yang, P. D. *Angew. Chem.-Int. Ed.* **2006**, *45*, 7824-7828.
- (19) Rioux, R. M.; Song, H.; Hoefelmeyer, J. D.; Yang, P.; Somorjai, G. A. *J. Phys. Chem. B* **2005**, *109*, 2192-2202.
- (20) Li, Y.; El-sayed, M. A. *J. Phys. Chem. B* **2001**, *105*, 8938-8943.
- (21) Liu, Z.; Reed, D.; Kwon, G.; Shamsuzzoha, M.; Nikles, D. E. *J. Phys. Chem. C* **2007**, *111*, 14223-14229.
- (22) Liu, Z.; Shamsuzzoha, M.; Ada, E. T.; Reichert, W. M.; Nikles, D. E. *J. Power Sources* **2007**, *164*, 472-480.
- (23) Borchert, H.; Tenske, D.; Kolny-Olesiak, J.; Parisi, J.; Al-Shamery, K.; Baeumer, M. *Angew. Chem.-Int. Ed.* **2007**, *46*, 2923-2926.
- (24) Lange, C.; De, C., D; Gamez, A.; Storck, S.; Bradley, J. S.; Maier, W. F. *Langmuir* **1999**, *15*, 5333-5338.
- (25) Borodko, Y.; Habas, S. E.; Koebel, M.; Yang, P. D.; Frei, H.; Somorjai, G. A. *J. Phys. Chem. B* **2006**, *110*, 23052-23059.
- (26) Bradley, J. S.; Hill, E. W.; Behal, S.; Klein, C.; Chaudret, B.; Duteil, A. *Chem. Mater.* **1992**, *4*, 1234-1239.

- (27) Spiewak, B. E.; Shen, J.; Dumesic, J. A. *J. Phys. Chem.* **1995**, *99*, 17640-17644.
- (28) Zhou, S. H.; Varughese, B.; Eichhorn, B.; Jackson, G.; Mcilwrath, K. *Angew. Chem.-Int. Ed.* **2005**, *44*, 4539-4543.
- (29) Wang, Y.; Alsmeyer, D. C.; Mccreery, R. L. *Chem. Mater.* **1990**, *2*, 557-563.
- (30) Borodko, Y.; Humphrey, S. M.; Tilley, T. D.; Frei, H.; Somorjai, G. A. *J. Phys. Chem. C* **2007**, *111*, 6288-6295.
- (31) Yoo, J. W.; Hathcock, D. J.; El-sayed, M. A. *J. Catal.* **2003**, *214*, 1-7.
- (32) Chan, H. Y. H.; Zou, S. Z.; Weaver, M. J. *J. Phys. Chem. B* **1999**, *103*, 11141-11151.
- (33) Argo, A. M.; Odzak, J. F.; Lai, F. S.; Gates, B. C. *Nature* **2002**, *415*, 623-626.
- (34) Ng, Y. H.; Ikeda, S.; Harada, T.; Park, S.; Sakata, T.; Mori, H.; Matsumura, M. *Chem. Mater.* **2008**, *20*, 1154-1160.

## Chapter 3: $\alpha \rightarrow \beta \rightarrow \alpha$ Phase Transitions of PdCu Alloy Nanoparticles and Catalysts

### 3.1 Introduction

As scientists find more ways to control the size, shape and structure of metallic nanoparticles (NPs), these materials are finding widespread use in a multitude of catalytic<sup>1</sup>, bioimaging<sup>2</sup>, and novel plasmonic applications.<sup>3</sup> By tuning metal salt reduction synthesis parameters, taking advantage of adsorbate induced segregation<sup>4-6</sup>, surface site blocking<sup>7,8</sup> and controlling NP shape via crystal growth kinetics<sup>9, 10</sup>, many advances have been made toward the ultimate goal of “rational design” of nanomaterials having specific, tunable functionality. In particular, the controlled design of many complex bimetallic nanoparticle architectures has led to the development of highly active and selective catalysts as well as a more fundamental understanding of what the important factors are in designing a bimetallic NP catalyst for a given homo- or heterogeneous reaction.

The Pd-Cu alloy system has been studied extensively by the surface science and NP catalysis communities because of its potential as an active catalyst for a host of organic liquid-solid and gas-solid heterogeneous transformations.<sup>11</sup> Catalytic performance can be tuned in many of these systems by changing the Pd:Cu ratio of the resultant alloy. Toshima and coworkers found that higher activity and selectivity for the hydration of acrylonitrile could be obtained by tuning the Pd:Cu ratio of 4 nm PdCu alloy NPs. They proposed that the increase in Pd-Cu contacts on the surface may play a role in the enhanced catalytic performance.<sup>12</sup>

The alloying behavior of the Pd-Cu system in small NPs (~5 nm) has been studied independently by Bradley and Toshima via EXAFS.<sup>12, 13</sup> Bradley and coworkers prepared 5-6 nm Pd<sub>90</sub>Cu<sub>10</sub> alloys and by using FTIR-CO probe techniques along with EXAFS found that Cu migrates into the core of the NP to maximize Pd-Cu contacts and forms a gradient alloy with a Pd-rich shell. This Cu core migration was observed even when the alloy NPs were prepared by sequential deposition of Cu<sup>2+</sup> precursor onto preformed Pd NPs. Toshima and coworkers prepared a series of PdCu alloy NPs ranging from 4/1 to 1/4 Pd/Cu ratio and through EXAFS studies found similar results as Bradley for low Cu concentration alloy NPs. At higher Cu concentrations, the exothermicity of Pd-Cu bond formation (-13 kJ/mol)<sup>14</sup> forced an enrichment of Cu at the surface to maintain a maximum of Pd-Cu contacts. They proposed a “hetero-bond-philic structure” that is in contrast to other bimetallic systems such as Pt/Pd and Au/Pd that form core-shell or cluster-in-cluster bimetallic architectures.<sup>15</sup>

Bradley and coworkers have extensively studied the PdCu alloy NP system by way of FTIR-CO probe experiments.<sup>16-18</sup> They have shown that the presence of solution-phase CO can induce a highly Pd-dominant surface in the alloy NPs because of the relative strength of Pd-CO binding in comparison to Cu-CO binding. They also showed that this CO induced segregation behavior was reversible. After 1 hour of heating the colloidal PdCu alloy NPs that had been subjected to saturation CO coverage, the original mixed Pd-Cu surface was recovered. Most studies of PdCu alloy surfaces have shown a slight enrichment of Cu at the surface. This enrichment may be due to a slightly lower surface energy

of Cu ( $1.84 \text{ J/m}^2$ ) compared to Pd ( $2.09 \text{ J/m}^2$ )<sup>19</sup> or it may be due to the preference of Pd-Cu contacts over Cu-Cu or Pd-Pd contacts in moderate to high Cu-rich systems. Also, the reduction potentials of Cu (0.34 V) and Pd (0.915 V)<sup>20</sup> would suggest that initial nucleation and growth would consume the Pd<sup>n+</sup> precursor before Cu<sup>n+</sup> precursor, creating a gradient alloy structure with a Pd rich core and a Cu rich shell. These studies show that randomly alloyed (solid solution) structures are dominant in small NPs due to the high enthalpy of formation of Pd-Cu bonds compared to Cu-Cu and Pd-Pd bond formation (EXAFS) and the low barrier for segregation or redistribution of atoms in the near-surface region (FTIR-CO).

The thermodynamic phase diagram of the Pd-Cu system shows an ordered  $\beta$ -phase (bcc, CsCl structure) at temperatures where most metal salt reduction syntheses of these PdCu alloy NPs occur ( $<300 \text{ }^\circ\text{C}$ ).<sup>21</sup> The transition from the ordered  $\beta$ -phase to the solid solution  $\alpha$ -phase (fcc, random alloy) occurs near  $500 \text{ }^\circ\text{C}$  for a 1:1 molar ratio of Pd:Cu. The phase diagram is in direct contrast to many PdCu alloy NP studies including those mentioned above which show the PdCu alloy in the random alloy phase. This discrepancy suggests a complex interplay of surface effects, hetero-atom bonding preferences, reduction potentials and surface energies that can produce metastable structures for nanomaterials and offers fresh avenues to create materials with controllable architectures. Schaak and coworkers have exploited this phenomena to create a series of metastable PtM (M = Sn, Bi, Pb, Sb) intermetallic alloys that are normally only accessible under high temperature solid-state reaction conditions.<sup>22, 23</sup>

Here we present a systematic study of the phase transition behaviour of 3

nm PdCu alloy NPs loaded onto high surface area SiO<sub>2</sub> supports (PdCu/SiO<sub>2</sub>) by annealing the samples at various temperatures and over various times while tracking the phase transitions via powder XRD. PdCu/SiO<sub>2</sub> catalysts with relatively low NP loading exhibit a significantly slower transition from the kinetic  $\alpha$  phase to the thermodynamically stable  $\beta$  phase compared to unsupported PdCu NPs. These results suggest that NP growth is required to transition from the kinetically trapped  $\alpha$  phase to the thermodynamically stable  $\beta$  phase. Because more than 60% of the atoms are within one layer of the surface for small (3 nm) NPs, we expect surface effects (ligands and surface energies) to determine the overall structure of the NP. Conversely, as NPs grow, a larger fraction of the atoms are in the core of the NP and bulk thermodynamic structures will dominate. Recently Busca et al. prepared PdCu alloy NPs supported on Al<sub>2</sub>O<sub>3</sub> via coimpregnation of metal oxides followed by 400 °C reduction in H<sub>2</sub>. Their XRD analysis showed a mixture of  $\alpha$  and  $\beta$  phases of the PdCu alloy system but no further analysis was performed.<sup>24</sup>

## 3.2 Experimental

### **3.2.1 Synthesis**

#### *3.2.1.1 PdCu Alloy Nanoparticles*

PdCu alloy nanoparticles were prepared by using a slightly modified synthesis reported by Bradley.<sup>16</sup> Briefly, 29.4 mg of Cu(acetate)<sub>2</sub>, 38.3 mg of Pd(acetate)<sub>2</sub> and 63.1 mg of polyvinylpyrrolidone (PVP) (55000 MWT) were charged into a 100 mL 3-neck round bottom flask with a Teflon stirbar. The dry reagents were placed under vacuum for 30 minutes at room temperature before

injecting 20 mL of 2-ethoxyethanol. The mixture was stirred at room temperature while switching between N<sub>2</sub> and vacuum atmospheres to remove oxygen. Once the precursors were completely dissolved, the mixture was heated rapidly (~10 °C/min) under an N<sub>2</sub> atmosphere. The green/orange solution gradually became darker and finally formed a black colloidal suspension at 75 °C. The colloid was then heated to 125 °C for an additional 60 minutes. The reaction was quenched by removing the heating mantle and placing the flask in an ice bath.

#### *3.2.1.2 SiO<sub>2</sub> loaded PdCu Alloy Nanoparticles*

Appropriate amounts of high surface area SiO<sub>2</sub> were added to 5 mL of the PdCu colloidal suspension to create 6% total metal loaded catalysts. The slurries were heated to 90 °C under N<sub>2</sub> atmosphere and stirred overnight. The solvent was then removed from the catalyst by vacuum distillation at 90 °C. The catalysts were washed several times with acetone and separated from the solution by centrifugation at 2000 RPM. Finally, the samples were dried in a 60 °C oven for 1 hour before further analysis.

### **3.2.2 Characterization**

#### *3.2.2.1 Transmission Electron Microscopy*

TEM samples were prepared by diluting ~200 µL of the colloidal suspension in ~1 mL 1-propanol or deionized water. 5 µL of this mixture was drop-cast and dried on continuous carbon film-deposited copper or nickel grids. A small amount of the PdCu alloy catalyst was suspended via sonication in deionized water before drop-casting onto copper or nickel grids. A JEM 2100 LaB6 TEM operating at 200 kV was used for both low and high-resolution imaging.

### 3.2.2.2 *Fourier Transform IR – CO Probe*

For the IR-CO probe experiments, the PdCu alloy colloidal suspension was bubbled with CO using a stainless steel needle submerged in the suspension at a flow rate of 35 sccm for 10 minutes. A 100  $\mu$ L aliquot of CO saturated colloidal suspension was filled in a liquid IR cell and monitored in a Nexus 870 FT-IR spectrometer. The liquid IR cell consisted of a 0.5 mm Teflon spacer sandwiched between two rectangular CaF<sub>2</sub> windows. The colloidal suspension prior to CO bubbling was used for the background spectra.

### 3.2.2.3 *Powder X-ray Diffraction*

A Bruker C2 Discover (Parallel Beam) General Area Diffraction Detection (GADDS) system was used for powder diffraction detection. The monochromatic Cu K $\alpha$  radiation source that was biased at 40 mV and 40 mA was employed along with Bruker ACS Hi-Star detector. The diffraction patterns were acquired between 33-90° by integrating four frames with 14° 2 $\theta$  per frame while the sample was oscillated in the XY plane to provide more homogeneous signal acquisition. Nanoparticle samples were prepared by washing 3 mL aliquots of the native PdCu alloy suspension in acetone and centrifuging at 6000 RPM for 10 minutes to separate the nanoparticles from solution by decanting the clear supernate. The wash/centrifuge procedure was repeated and finally the nanoparticle powders were dried in a 60 °C oven for ~1 hour before XRD analysis. Unsupported nanoparticle powders and PdCu/SiO<sub>2</sub> catalysts were pressed onto a glass slide for XRD analysis.

#### 3.2.2.4 *Ex-situ Annealing*

Nanoparticle powders or SiO<sub>2</sub> supported nanoparticles were loaded into Pyrex tubing and attached to a vacuum manifold. The samples were cycled between N<sub>2</sub> and vacuum atmospheres several times before a final 60-minute evacuation. The tubes were flame-sealed and heated in a programmable tube furnace at a rate of 10 °C/min until the desired temperature and then held isothermally for 3-72 hours.

### 3.3 Results and Discussion

#### **3.3.1 TEM and FTIR-CO Probe Characterization**

TEM images (Fig. 3.1) show that the PdCu alloy nanoparticles (NPs) are monodisperse and spherical in shape with an average size of 2.9 nm. TEM images of the Al<sub>2</sub>O<sub>3</sub> supported PdCu alloy (PdCu/SiO<sub>2</sub>) are shown in Figure 3.2. No particle growth or sintering of the NPs is observed in the as-prepared samples and the NPs are well dispersed on the support.

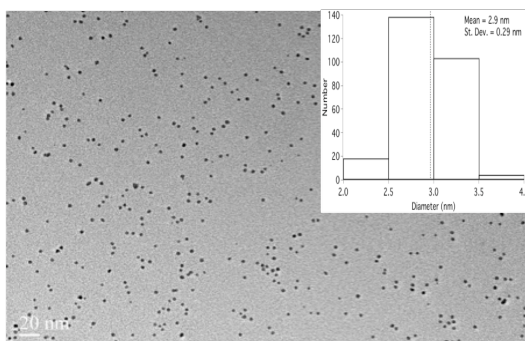


**Figure 3.1** Low-magnification TEM and histogram counting ~250 PdCu alloy nanoparticles.

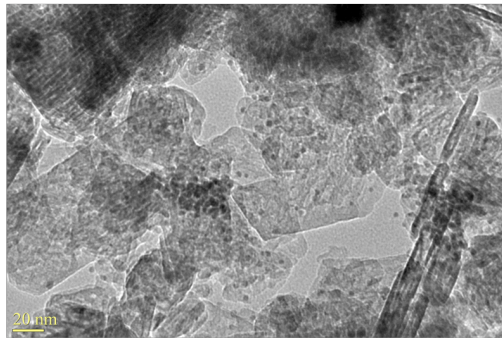


**Figure 3.2** Low-magnification TEM of 2.5% wt PdCu/SiO<sub>2</sub>.

FTIR-CO probe experiments were performed on the colloidal PdCu NPs to determine the surface binding geometries and oxidation states of the surface Pd and Cu species. Figure 3.3 shows spectra in the region of 2200-1800 cm<sup>-1</sup>. Three

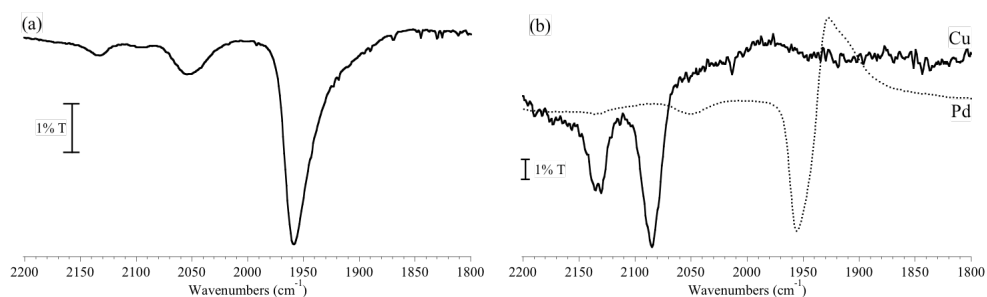


**Figure 3.3** FTIR-CO probe of (a) PdCu (50:50) alloy nanoparticles and (b) Pd and Cu monometallic nanoparticles.

main bands are observed for the PdCu alloy NPs (Fig. 3.3a). Bands centered at 1960, 2050 and 2095 cm<sup>-1</sup> are indicative of Pd-CO<sub>bridge</sub>, Pd-CO<sub>linear</sub> and Cu-CO<sub>linear</sub> modes, respectively. For comparison, monometallic Cu and Pd NP colloids were prepared and analyzed via FTIR-CO probe experiments and are shown in Figure 3.3b. The band positions of the PdCu alloy NPs are close to those observed for the monometallic Pd and Cu NPs indicating that the surface of the PdCu alloy NPs is metallic and exhibits “normal” binding geometries. Bradley and coworkers have performed extensive studies of PdCu alloy NP colloids using the FTIR-CO probe

technique.<sup>18</sup> Our findings are in general agreement with their reports. In one study they reported on the relative intensities of the Pd-CO<sub>bridge</sub> and Pd-CO<sub>linear</sub> bands and found that as the NP size decreased, the intensity of the Pd-CO<sub>bridge</sub> band increased at the expense of the Pd-CO<sub>linear</sub> band. This change in relative band intensities was rationalized by a geometric argument that for a smaller NP, a larger proportion of edge and terrace sites (which preferentially bind CO in a bridging fashion) are present compared to face sites. This rationale is in agreement with the relative band intensities of the Pd-CO<sub>bridge</sub> and Pd-CO<sub>linear</sub> species observed in the FTIR spectrum of our PdCu alloy NPs (Fig. 3.3a) and the small size and rounded shape of the nanoparticles observed in our TEM results (Fig. 3.1).

By monitoring the XRD of the PdCu alloy NPs over time we found that the  $\beta$  phase PdCu alloy NPs can be made by “annealing” solutions of PdCu alloy NP colloids for several hours (see subsequent XRD analysis sections). Figure 3.4 shows FTIR-CO probe spectra acquired over the course of 10 hours. No change in

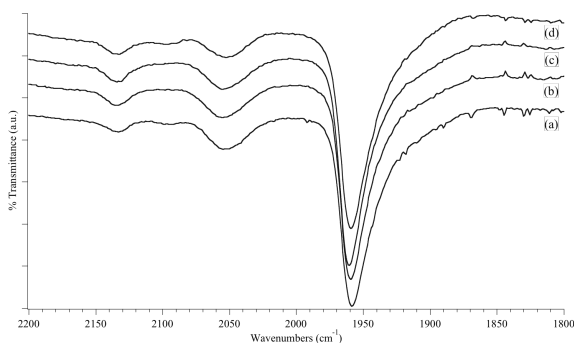


**Figure 3.4** FTIR-CO probe experiments of PdCu alloy nanoparticles after (a) 10 minutes, (b) 1 hour, (c) 4 hours and (d) 10 hours of reflux.

the surface structure is observed upon phase transition from the kinetic  $\alpha$  phase to the thermodynamic  $\beta$  phase. One might expect that the ordered  $\beta$  phase would show a significantly different surface electronic structure due to the high ordering

and lack of heterogeneity compared to the  $\alpha$  phase. A likely explanation is that the surface restructures to the most favorable configuration for saturation CO coverage during the CO probe and measurement. This explanation is consistent with Bradley and coworkers findings on similar PdCu alloy NPs.<sup>13</sup> In order to avoid altering the surface structure of the PdCu alloy NP through environmental effects, we used XRD as a bulk phase analysis technique to distinguish changes in the PdCu alloy NPs and catalysts.

### 3.3.2 XRD Analysis of PdCu alloy NPs

A general schematic of the PdCu alloy phase diagram is presented in Figure 5. The dashed vertical line indicates the Pd:Cu molar ratio (50:50) used in

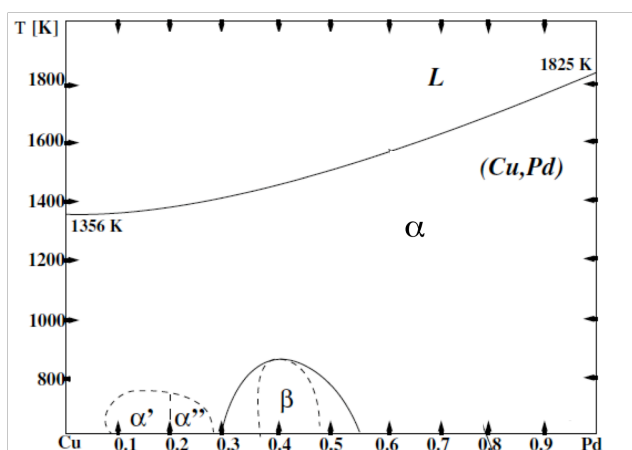


**Figure 3.5** General phase diagram of bulk Pd-Cu alloy. Adapted from reference [21].

this study. The diagram shows that the thermodynamically stable phase at temperatures used most often in colloidal NP synthesis (<300 °C) is the ordered (bcc)  $\beta$  phase.

Powder XRD analyses of the PdCu alloy NPs are shown in Figure 6. The as-prepared PdCu alloy NPs show broad diffraction peaks indicative of lattice

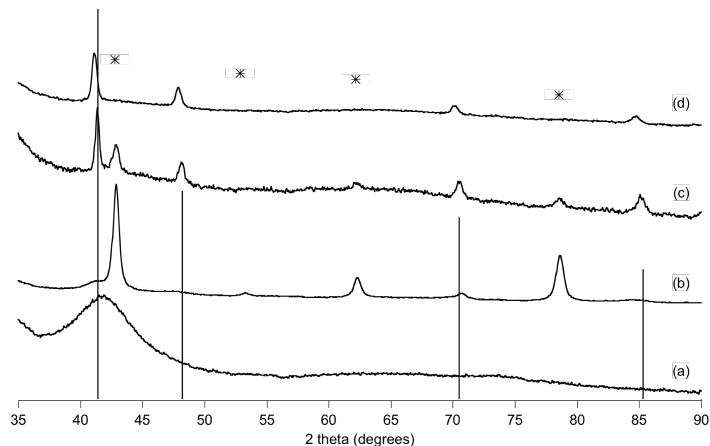


**Figure 3.6** Powder XRD of (a) as prepared PdCu alloy NPs, (b) annealed at 300 °C for 2 hours, (c) annealed at 500 °C for 4 hours and (d) annealed at 500 °C for 10 hours. Vertical lines indicate Pd:Cu (50:50) solid solution diffraction pattern (JCPDS file#: 48-1551). Markers indicate diffraction pattern of beta (bcc  $L1_0$ ) phase.

strain and/or poor crystallinity due to the small size of the NPs. The first diffraction peak at  $\sim 42.5^\circ$   $2\theta$  is very broad and slightly shifted to higher  $2\theta$  than the 1:1 Pd:Cu random alloy, suggesting a slightly Cu enriched alloy. Another explanation for the slight shift toward higher  $2\theta$  is that a small amount of  $\beta$  phase has already formed even after short times at mild temperatures (1 hour, 125 °C). A weak shoulder is also observed near the (200) diffraction peak position of the 1:1 Pd:Cu random alloy. No diffraction peaks are observed for the higher  $2\theta$  indices. This result also may be due to the small size and poor crystallinity of the as-prepared PdCu alloy NPs.<sup>25</sup> Upon annealing at 300 °C, the XRD pattern shows the PdCu alloy NPs transitioning from the kinetic  $\alpha$  phase to the thermodynamic  $\beta$  phase. Both phases are present at this relatively mild temperature and short annealing time. Annealing the PdCu alloy NPs at 500 °C for 4 hours produces the thermodynamic  $\alpha$  phase, though some residual  $\beta$  phase is clearly present. Finally, annealing the PdCu alloy NPs at 500 °C for 10 hours shows the complete

conversion to the thermodynamic  $\alpha$  phase.

We can assume that annealing the dried, unsupported NP powders at even mild temperatures will cause the NPs to coalesce into bulk metal alloys. To determine quantitatively what size regime and minimum temperature is required to cause the kinetic  $\alpha$  phase to transition to the thermodynamically favorable  $\beta$  phase we “annealed” a 10 mL aliquot of the native PdCu alloy colloid by stirring at 130 °C for 7 hours under an N<sub>2</sub> atmosphere. The XRD pattern and a TEM image of this sample are shown in Figure 7. For comparison, the as prepared PdCu alloy NP

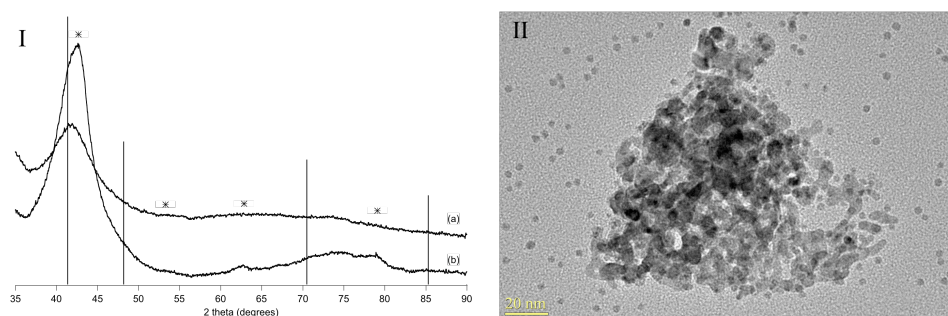


**Figure 3.7** (I) Powder XRD of (a) as prepared PdCu alloy NPs and (b) PdCu alloy NPs solution annealed for 7 hours at 130 °C. Vertical lines indicate Pd:Cu (50:50) solid solution diffraction pattern (JCPDS file#: 48-1551). Markers indicate diffraction pattern of beta (bcc L1<sub>0</sub>) phase. (II) TEM image of solution annealed (130 °C, 7 hours) PdCu alloy NPs.

XRD pattern is also shown. The shift in the main diffraction peak as well as the appearance of peaks at higher 2θ angles are evidence of the transition from the kinetic  $\alpha$  to thermodynamic  $\beta$  phase. The TEM image in Figure 7 shows a mixture of relatively small and monodisperse PdCu alloy NPs as well as larger aggregates. Apparently, heating the PdCu alloy NP colloid for long times causes the small NPs to aggregate and form clustered networks where the smaller domains are approximately 15-20 nm in diameter and the larger clusters range between 100 and 200 nm in diameter. These clusters may form due to a breakdown of the

PVP-NP interactions at elevated temperatures over long periods of time or because the small PdCu alloy NPs have relatively high surface energies. We believe that these large aggregates are responsible for the  $\beta$  phase observed in the XRD in Figure 7.

### 3.3.3 Comparison of PdCu alloy NPs and Highly Diluted Catalyst

#### Materials

To add further evidence that PdCu NP growth is a requirement for the kinetic  $\alpha$  to thermodynamic  $\beta$  phase transition we prepared catalysts with low loadings of PdCu alloy NPs using high surface area SiO<sub>2</sub> as the support material. By diluting the PdCu alloy NPs in the inert SiO<sub>2</sub> matrix we hoped to suppress NP growth and therefore suppress the transition from the kinetic  $\alpha$  phase to the thermodynamic  $\beta$  phase.

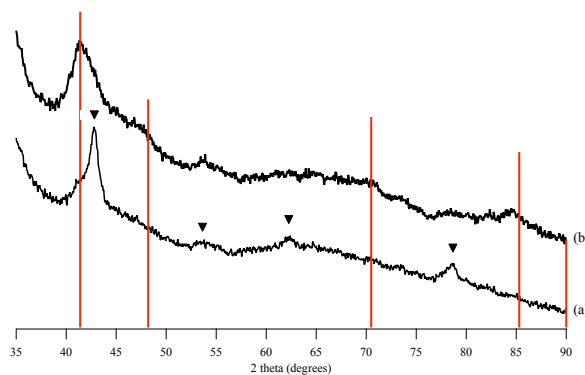


**Figure 3.8** XRD of (a) as-prepared PdCu alloy NPs and (b) 2.5% PdCu/SiO<sub>2</sub>. Vertical lines indicate diffraction pattern of Pd:Cu (50:50) solid solution (fcc)  $\alpha$  phase (JCPDS file #: 48-1551). Markers indicate diffraction pattern of ordered (bcc)  $\beta$  phase.

The PdCu alloy NPs supported in SiO<sub>2</sub> with 2.5% total metal loading (PdCu/SiO<sub>2</sub>) were heated at 210 °C over a time period of a few days. We knew from previous experiments that 210 °C annealing would cause the unsupported PdCu alloy NPs to transition from the kinetic  $\alpha$  phase to the thermodynamic  $\beta$

phase. Figure 8 shows XRD patterns of the unsupported PdCu alloy NPs and PdCu/SiO<sub>2</sub> after 24 hours of annealing at 210 °C. Clearly, the unsupported NPs transition readily to the  $\beta$  phase while the PdCu/SiO<sub>2</sub> remains trapped in the  $\alpha$  phase, though a small shoulder at higher  $2\theta$  of the main (111) peak is observed. This structural evolution could be due to close contact of neighboring NPs within the SiO<sub>2</sub> matrix or because of agglomeration of unsupported PdCu NPs.

### 3.4 Conclusions

We have shown that small PdCu alloy NPs possess a thermodynamically unfavored random alloy fcc phase at low temperatures and that these NPs transition to the thermodynamically favorable ordered bcc phase upon heating at low temperatures either in colloidal suspension or as unsupported NP powders. The phase transition can be suppressed by supporting the NPs in an inert matrix that spatially isolates the NPs and inhibits NP growth. These results strongly suggest that NP growth is a requirement for the  $\alpha$  to  $\beta$  phase transition and offers a unique view of the interplay between thermodynamic and kinetic variables that control NP alloy structures.

Current work in our lab focuses on making slightly larger NPs with presumably lower surface energies that are less prone to agglomerate at moderate temperatures. Our preliminary results suggest that we can obtain predominantly ordered  $\beta$  phase NPs with reasonably small sizes. These highly ordered phase bimetallic nanoalloy catalysts may provide enhanced activities and selectivities for a variety of catalytic transformations. Although, as previously reported by Bradley and coworkers, the near-surface atoms of these alloy NPs could fluctuate

to accommodate preferred binding of reactants or stabilizing ligands.

### 3.5 References

- (1) Bonnemann, H.; Richards, R. M. *Eur J Inorg Chem* **2001**, 2455-2480.
- (2) Sharna, P.; Brown, S.; Walter, G.; Santra, S.; Moudgil, B. *Adv Colloid Interface* **2006**, *123*, 471-485.
- (3) Ozbay, E. *Science* **2006**, *311*, 189-193.
- (4) Lang, H.; Maldonado, S.; Stevenson, K.; Chandler, B. *J. Am. Chem. Soc.* **2004**, *126*, 12949-12956.
- (5) Mu, R.; Fu, Q.; Liu, H.; Tan, D.; Zhai, R.; Bao, X. *Appl. Surf. Sci.* **2009**, *255*, 7296-7301.
- (6) Bernardi, F.; Alves, M.; Traverse, A.; Silva, D.; Scheeren, C.; Dupont, J.; Morais, J. *J. Phys. Chem. C* **2009**, *113*, 3909-3916.
- (7) Grass, M. E.; Joo, S. H.; Zhang, Y.; Somorjai, G. A. *J. Phys. Chem. C* **2009**, *113*, 8616-8623.
- (8) Lange, C.; De Caro, D.; Gamez, A.; Storck, S.; Bradley, J. S.; Maier, W. F. *Langmuir* **1999**, *15*, 5333-5338.
- (9) Somorjai, G. A.; Park, J. Y. *Top Catal* **2008**, *49*, 126-135.
- (10) Xiao, L.; Zhuang, L.; Liu, Y.; Lu, J.; Abruna, H. D. *J. Am. Chem. Soc.* **2009**, *131*, 602-608.
- (11) Aiken, J. D.; Finke, R. G. *J Mol Catal A-Chem* **1999**, *145*, 1-44.
- (12) Bian, C. R.; Suzuki, S.; Asakura, K.; Ping, L.; Toshima, N. *J Phys Chem B* **2002**, *106*, 8587-8598.

- (13) Bradley, J. S.; Via, G. H.; Bonneviot, L.; Hill, E. W. *Chem. Mater.* **1996**, *8*, 1895-1903.
- (14) Smithells, C.; Brandes, E. *Metals Reference Book*; Butterworths: London, 1976;
- (15) Shiraishi, Y.; Ikenaga, D.; Toshima, N. *Aust. J. Chem.* **2003**, *56*, 1025-1029.
- (16) Bradley, J. S.; Hill, E. W.; Klein, C.; Chaudret, B.; Duteil, A. *Chem. Mater.* **1993**, *5*, 254-256.
- (17) Bradley, J. S.; Millar, J. M.; Hill, E. W.; Klein, C.; Chaudret, B.; Duteuil, A.; Geus, J. W.; Joyner, R. W.; Fouilloux, P.; Sermon, P. A.; Ichikawa, M.; Bozonverduraz, F. *Stud. Surf. Sci. Catal.* **1993**, *75*, 969-979.
- (18) Bradley, J. S.; Hill, E. W.; Chaudret, B.; Duteil, A. *Langmuir* **1995**, *11*, 693-695.
- (19) Ponc, V.; Bond, G. C. *Catalysis by Metals and Alloys*; Elsevier: Amsterdam, 1995;
- (20) Bard, A. J.; Faulkner, L. R. *Electrochemical Methods: Fundamentals and Applications*; John Wiley & Sons: New York, 2001;
- (21) Bozzolo, G.; Garces, J. E.; Noebe, R. D.; Abel, P.; Mosca, H. O. *Prog. Surf. Sci.* **2003**, *73*, 79-116.
- (22) Sra, A. K.; Schaak, R. E. *J. Am. Chem. Soc.* **2004**, *126*, 6667-6672.
- (23) Cable, R.; Schaak, R. *Chem. Mater.* **2007**, *19*, 4098-4104.
- (24) Sanchez-Escribano, V.; Arrighi, L.; Riani, P.; Marazza, R.; Busca, G. *Langmuir* **2006**, *22*, 9214-9219.
- (25) Yan, W. F.; Petkov, V.; Mahurin, S. M.; Overbury, S. H.; Dai, S. *Catal Commun* **2005**, *6*, 404-408.

# Chapter 4: Ru@Pt and PtRu Alloy Nanoparticles: Combined DRIFT Spectroscopy and Catalysis Studies on Surface Segregation and Surface Redox Properties

## 4.1 Introduction

Developing bimetallic catalysts with high activity and selectivity has historically been an empirical endeavor that has led to many highly active and selective catalysts for a variety of heterogeneous transformations.<sup>1, 2</sup> Only recently have advances in the rational design of bimetallic systems allowed for the design of high activity and/or selectivity catalysts based on surface composition<sup>3</sup>, particle shape<sup>4-6</sup>, particle size<sup>7</sup> and other electronic or ligand effects.<sup>4, 8</sup> Much of the recent understanding about structure-activity relationships have derived from advanced analytical surface science techniques as well as first principles calculations.<sup>9, 10</sup>

One of the major challenges of studying nano-phase bimetallic catalysts is determining the bimetallic composition and structure of the nanoparticles under normal catalytic reaction conditions, i.e., operating temperatures, pressures and reactant concentrations. *In situ* techniques such as Raman and various IR spectroscopies have historically been used to observe changes in oxidation state and binding geometries of adsorbates for many monometallic and bimetallic alloy nano-catalysts.<sup>11, 12</sup> More recent IR spectroscopic studies of complex bimetallic nanoparticles have shown that surface adsorbates can restructure a nanoparticle surface due to preferential binding of reactants such as CO and NO<sub>x</sub>.<sup>13, 14</sup> Most recently, *in situ* XPS has been used to study Fe-Pt<sup>15</sup>, Pt-Ni<sup>16</sup> and Pt-Pd<sup>15</sup> bimetallic

systems under a variety of catalytically relevant conditions to show similar surface and bulk restructuring of nanoparticles due to changes in oxidation state. In all of these studies, however, little effort has gone into making direct quantitative correlations between nanoparticle structure and catalytic activity and specificity. Predictive rational design of nanoparticle systems having well defined catalytic properties must be able to identify explicitly how nanoparticle structural evolution directly impacts the catalysts' performance in reactive applications. Scientists and engineers must know the consequences of structure transformation and how reversibility of nanoparticle structures might influence catalytic processes. This last issue is particularly important if derived structure-function relationships depend on *ex situ* analysis before and after usage.

In the studies presented below we directly correlate the structure of Pt-Ru nanoparticles having different bimetallic architectures with the ability of these nanoparticles to catalyze either CO oxidation or preferential CO oxidation (PROX). The nanoparticle architectures themselves are either Ru@Pt (core@shell) or PtRu alloy, both of which consist of 50:50 (Ru:Pt) composition and are of the same size and shape. Using CO adsorption DRIFT spectroscopy we show that oxidized state Ru@Pt and PtRu alloy catalysts show similar surface structures while reduced state Ru@Pt and PtRu alloy catalysts show significantly different surface structures. The differences and similarities in surface structure observed for the reduced and oxidized Pt-Ru systems correlate well with reducing catalytic reaction (PROX) and oxidizing catalytic reaction (CO oxidation) activities observed in temperature programmed reaction profiles (TPR), respectively. Repeated catalyst cycling shows that the

different surface structures of the Ru@Pt and PtRu alloy catalysts are reversible over several reduction-oxidation cycles. *Ex situ* EDS line scans also show the stability of the Ru@Pt (core@shell) structure over several reduction-oxidation cycles.

## 4.2 Experimental

### **4.2.1 Synthesis**

#### *4.2.1.1 Ru@Pt and PtRu alloy Nanoparticles*

The Ru@Pt core-shell nanoparticles were synthesized using a sequential polyol process described elsewhere.<sup>17</sup> Briefly, Ru(acac)<sub>3</sub> (acac = acetylacetonate) was initially reduced in refluxing glycol in the presence of polyvinylpyrrolidone stabilizers (MWT = 55,000). The resulting Ru nanoparticles (mean particle size = 3.0 nm) were subsequently coated with Pt by adding PtCl<sub>2</sub> to the Ru/glycol colloid and slowly heating to 200 °C. The PtRu alloy nanoparticles were synthesized via co-reduction of the [Ru(CO)<sub>3</sub>Cl<sub>2</sub>]<sub>2</sub> dimer and Pt(acac)<sub>2</sub> with glycol and polyvinylpyrrolidone stabilizer at 200 °C.

#### *4.2.1.2 Synthesis of 1% Metal Loaded Al<sub>2</sub>O<sub>3</sub> Catalysts*

The catalysts are prepared by adding  $\gamma$ -Al<sub>2</sub>O<sub>3</sub> to colloidal suspension of nanoparticles, and drying the slurry under vacuum. Typically, 10 mL of any suspension and 973 mg  $\gamma$ -Al<sub>2</sub>O<sub>3</sub> are mixed overnight and vacuum dried at temperatures over 100 °C while vigorously stirring the mixture. Such composition yields a 1% by weight Pt alumina supported bimetallic catalyst. The catalyst is washed with acetone several times and equi-volume mixture of acetone and ethanol, then baked at 60 °C overnight.

## 4.2.2 Characterization

### 4.2.2.1 TEM Analysis with EDS Line Scan

A Jeol 2100F Field Emission Transmission Electron Microscope (FE-TEM) equipped with an Inca Energy Dispersive Spectrometer (EDS) was used for line scans of the nanoparticles. The FE-TEM was operated at 200 kV in scanning mode. The TEM samples were prepared by dropcasting 1-propanol diluted catalysts powders or nano-colloids onto Cu TEM grids that were allowed to air dry before analysis.

### 4.2.2.2 Diffuse Reflectance Infrared Fourier Transform Spectroscopy

IR spectra were collected using a Thermo Nicolet Nexus 670 spectrometer in diffuse reflectance mode (DRIFTS). Approximately 20 mg of 1 wt.% Pt (Ru@Pt or PtRu alloy)/Al<sub>2</sub>O<sub>3</sub> was loaded into the DRIFTS chamber and heated to 210 °C in He and held isothermally for 30 minutes before further analysis. For CO adsorption measurements, the sample was exposed to a 2% CO / 2% Ar / 96% He atmosphere for 10 minutes and then purged for 15 minutes under He before acquiring spectra at 120 °C. For the reduction oxidation cycles, the sample was heated at 10 °C/min to 210 °C in He and held isothermally for 30 minutes in either 4% H<sub>2</sub> / 96% He (reducing) or 2% O<sub>2</sub> / 98% He (oxidizing) atmospheres. The sample was then cooled to 120 °C in He where the CO adsorption measurements were taken as described above.

#### 4.2.2.3 Preferential CO Oxidation (PROX) and CO Oxidation Catalysis

Our fixed bed reactor setup used to study the PROX and CO oxidation reactions has been described previously.<sup>18</sup> Briefly, 105 mg of 1 wt% Pt (Ru@Pt or PtRu alloy)/Al<sub>2</sub>O<sub>3</sub> was mixed with 135 mg of quartz sand and loaded into a quartz tube surrounded by a programmable furnace. Gases were controlled by mass flow controllers and the effluent gas phase product was analyzed by a Prima δ8 mass spectrometer. Temperature programmed reactions (TPR) were run at 1.8 °C/min to 210 °C and held isothermally for 30 minutes.

### 4.3 Results and Discussion

#### 4.3.1 TEM and EDS Line Scan Analysis

Figure 4.1 shows TEM of Ru@Pt, PtRu alloy and 1%wt Pt/Al<sub>2</sub>O<sub>3</sub> Ru@Pt catalysts. Ru@Pt and PtRu alloy NPs are 4 nm in average diameter, exhibit FCC structure and have a narrow size range. The loaded catalyst samples are well dispersed on the Al<sub>2</sub>O<sub>3</sub> support and no evidence of sintering is observed even after multiple reduction-oxidation cycles at 210 °C.

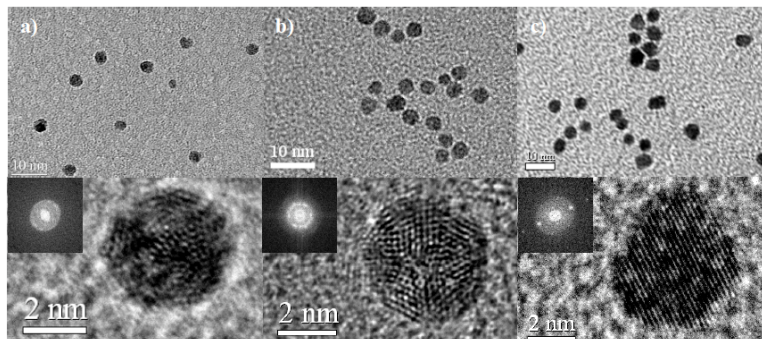


**Figure 4.1** TEM images of Ru (a), Ru@Pt (b), PtRu alloy (c) nanoparticles. HR-TEM images below with Fast Fourier Transform (FFT) inset. Adapted from reference [28].

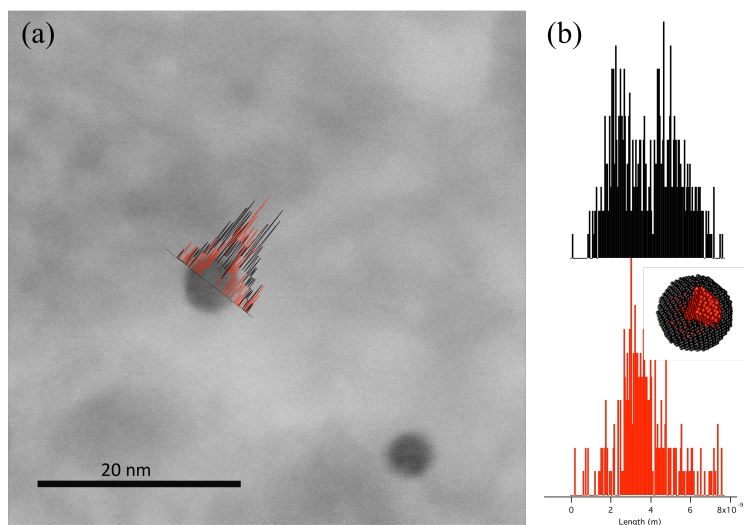


**Figure 4.2** (a) TEM with EDS line scan and (b) line scans separated for clarity. Sample is redox cycled Ru@Pt/Al<sub>2</sub>O<sub>3</sub> ending with a reducing cycle.

In a previous report from our group, single-particle EDS line scans were performed on as-prepared Ru@Pt nanoparticles and showed a bimodal distribution of Pt near the edges of the nanoparticle and a single peak at the center of the nanoparticle for Ru. This strongly suggests the proposed core@shell structure. EDS line scans were performed on post-catalysis Ru@Pt/Al<sub>2</sub>O<sub>3</sub> samples to determine if the original core@shell structure was preserved. For this experiment, two reduction-oxidation cycles were performed before a final reduction treatment for 30 minutes at 210 °C followed by cooling to room temperature under He atmosphere. Figure 4.2a shows the TEM image with the EDS line scan overlay. The same overlays are presented separately in Figure 4.2b for clarity. The EDS line spectrum for the Pt component is bimodal while the Ru component shows a single peak at the center of the nanoparticle. The bimodal shape for the shell material (Pt) and the single peak for the core material (Ru) show that the core@shell structure of the Ru@Pt nanoparticle

is maintained even after multiple reduction-oxidation cycles at 210 °C. No sintering or significant nanoparticle growth was observed.

### 4.3.2 DRIFT Spectroscopy

#### 4.3.2.1 Background on Band Assignments of CO Adsorption on Nano Phase PtRu

Table 4.1 shows CO band assignments from previous reports of CO adsorption on Pt, Ru and PtRu nano-catalyst and surface alloy systems along with the band positions for this work. While the binding geometries of CO on both reduced

Species	Frequency (cm <sup>-1</sup> )	System (particle size)	Comments	Reference
Pt <sup>0</sup> -CO	2076-90	Ru surface w/ 1ML Pt	atop	[19]
Pt <sup>0</sup> -CO	2070	Pt-Ru/SiO <sub>2</sub> (2.5-4 nm)	atop	[20]
Pt <sup>0</sup> -CO	2075	Pt-Ru/SiO <sub>2</sub> (3.6 nm)	atop	[21]
Pt <sup>0</sup> -CO	2062	Pt/Al <sub>2</sub> O <sub>3</sub> (1.1 nm)	atop	[22]
Pt <sup>0</sup> -CO	2085	Ru surface w/ sub monolayer Pt coverage	atop, terraced site	[23]
Pt <sup>0</sup> -CO	2070	Pt-Ru/SiO <sub>2</sub> (3.6 nm)	atop	[24]
Pt <sup>0</sup> -CO	2121	Pt/Al <sub>2</sub> O <sub>3</sub> (1.1 nm)	atop	[22]
mixed Pt,Ru-CO	2033-50	Ru surface w/ sub monolayer Pt coverage	CO on Pt-Ru step sites (Ru-CO)	[23]
Ru <sup>0</sup> -CO	2038-42	Ru/Al203 (3 nm)	atop	[25]
Ru <sup>0</sup> -CO	2049	Ru/Al <sub>2</sub> O <sub>3</sub> (thin film)	atop	[26]
Ru <sup>0</sup> -CO	2049	Pt-Ru/SiO <sub>2</sub> (3.6 nm)	atop	[24]
Ru <sup>0</sup> -CO	2049	Pt-Ru/SiO <sub>2</sub> (2.5-4 nm)	atop	[20]
Ru <sup>0</sup> -CO	2050	Pt-Ru/SiO <sub>2</sub> (3.6 nm)	atop	[21]
Ru <sup>0</sup> -CO	2000-49	Ru/Al <sub>2</sub> O <sub>3</sub> (3.6 nm)	atop	[24]
Ru <sup>0</sup> -CO	~2010	Ru/Al <sub>2</sub> O <sub>3</sub> (3.6 nm)	atop, isolated Ru <sup>0</sup> -CO surrounded by Ru <sup>+</sup>	[24]
Ru <sup>0</sup> -CO	2040±10	Ru/SiO <sub>2</sub> (1.1 nm)		[27]
Ru-(CO) <sub>2</sub>	2060, 1990	Ru/Al <sub>2</sub> O <sub>3</sub> (3.6 nm)	symmetric, asymmetric multicarbonyl	[24]
Ru <sup>0</sup> -CO	~2080	Ru/Al <sub>2</sub> O <sub>3</sub> (3.6 nm)	atop, Red shift w/ decreasing CO coverage	[24]
Ru <sup>0</sup> -CO <sub>2</sub>	2080, 2015	Ru/Al <sub>2</sub> O <sub>3</sub> (3.6 nm)	symmetric, asymmetric multicarbonyl	[24]
Ru <sup>0</sup> -CO <sub>2</sub>	2130-40, 2070-80	Ru/Al <sub>2</sub> O <sub>3</sub> (3.6 nm)	symmetric, asymmetric multicarbonyl on isolated Ru <sup>0</sup> sites	[24]
Ru <sup>0</sup> -CO <sub>2</sub>	2130-40, 2070-80	Ru/SiO <sub>2</sub> (1.1 nm)	symmetric, asymmetric multicarbonyl	[27]
Ru <sup>0</sup> -CO <sub>2</sub>	2140, 2080	Pt-Ru/SiO <sub>2</sub> (3.6 nm)	symmetric, asymmetric multicarbonyl	[24]
Pt <sub>2</sub> -CO, Ru <sub>2</sub> -CO	1700-1900	Pt-Ru/SiO <sub>2</sub> (2.5-4 nm)	bridge CO species on Pt <sup>0</sup> and Ru <sup>0</sup>	[20]
	2015-20	Ru@Pt, oxidized		This work
	2077	Ru@Pt, oxidized		This work
	2085sh	Ru@Pt, oxidized		This work
	2117	Ru@Pt, oxidized		This work
	2135	Ru@Pt, oxidized		This work
	2020	Ru@Pt, reduced		This work
	2085	Ru@Pt, reduced		This work
	2013	PtRu alloy, oxidized		This work
	2074	PtRu alloy, oxidized		This work
	2125	PtRu alloy, oxidized		This work
	2038	PtRu alloy, reduced		This work
	2074	PtRu alloy, reduced		This work
	2003	Ru, oxidized		This work
	2067	Ru, oxidized		This work
	2121	Ru, oxidized		This work
	2000	Ru, reduced		This work
	2044	Ru, reduced		This work

**Table 4.1** IR band assignments for CO stretching modes on Pt, Ru and Pt-Ru nano-catalyst and surfaces including main band positions for this work.

and oxidized Pt species are relatively straightforward, CO bound to oxidized and reduced Ru species can be complex due to the formation of multicarbonyl species.

Many of the band assignments of these multicarbonyl binding geometries are still

debated. The interpretations are also complicated by several overlapping bands of CO bound to Pt and Ru as well as shifting of bands due to dipole coupling, dilution and ligand effects. These effects will be discussed in the subsequent sections.

#### *4.3.2.2 DRIFT Spectroscopy*

Before the spectra were acquired the catalysts were oxidized or reduced at 210 °C followed by cooling to 120 °C to perform CO adsorption measurements described in the experimental section. This reduction-oxidation procedure was repeated several times on a single catalyst to show the reversible nature of the catalyst surface. For these IR studies we focused primarily on the 1900-2200  $\text{cm}^{-1}$  region where CO stretching modes of linearly bound CO on transition metals occur. Most literature is in agreement that bands in the 1700-1900  $\text{cm}^{-1}$  region can be assigned to bridge bound CO species, but their assignment to a particular metal species in a bimetallic system can be difficult due to overlap in bands and their characteristically weak and broad nature.

#### *4.3.2.3 DRIFT Spectra of Oxidized and Reduced PtRu alloy Catalysts*

Figure 4.3a shows CO adsorption DRIFT spectra at 120 °C after saturation CO coverage on PtRu alloy 1 wt% Pt/ $\text{Al}_2\text{O}_3$  catalysts that have been exposed to oxidizing (even numbers) and reducing (odd numbers) conditions. The spectra show clearly that the reduction oxidation cycles induce significant surface state changes in the case of the PtRu alloy catalyst and that the surface states are reversible.

Three broad but distinct bands centered at 2126  $\text{cm}^{-1}$ , 2072  $\text{cm}^{-1}$  and 2013  $\text{cm}^{-1}$  are present in the oxidized PtRu alloy spectra (Fig 4.3a2 and 4.3a4). One

interpretation is that these bands can be assigned to the CO stretching vibration of the CO stretching vibration of mono and multicarbonyls on Ru surface sites. The combination of  $2126\text{ cm}^{-1}$  and  $2072\text{ cm}^{-1}$  are commonly assigned to the symmetric and asymmetric modes of  $\text{Ru}^{n+}(\text{CO})_x$ , respectively. The broad feature at  $2013\text{ cm}^{-1}$  can be assigned to  $\text{Ru}^0\text{-CO}$  sites surrounded by a  $\text{Ru}^{n+}$  matrix. Due to the width of the bands, it is possible that an

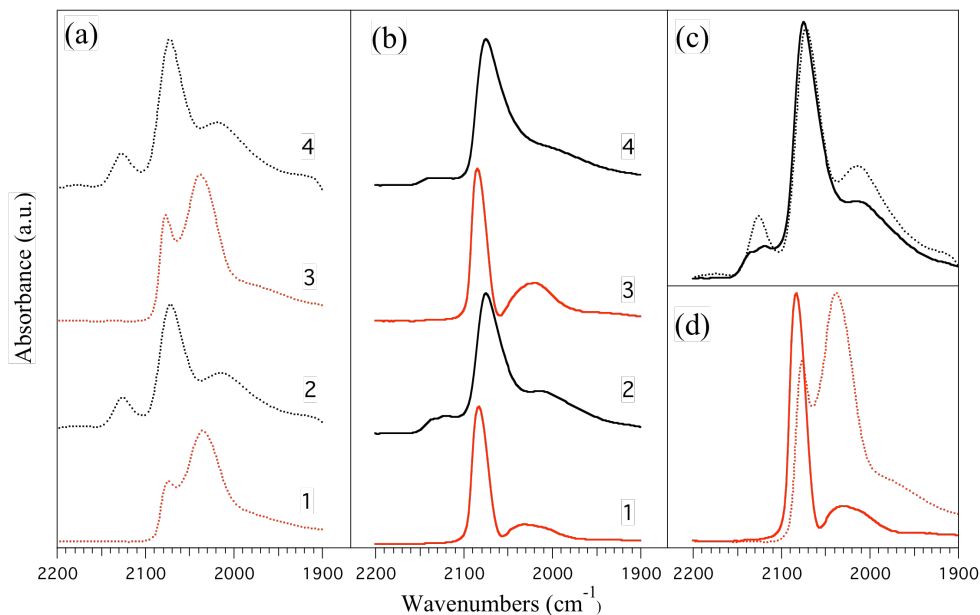


**Figure 4.3** DRIFTS of (a) Redox series for PtRu alloy, (b) Redox series for Ru@Pt, (c) comparison of oxidized state alloy and core@shell, (d) comparison of reduced state alloy and core@shell. Dashed lines indicate PtRu alloy. Solid lines indicate Ru@Pt. Red lines indicate reduction. Black lines indicate oxidation.

additional feature is present to the blue of the main  $2072\text{ cm}^{-1}$  band at  $2085\text{ cm}^{-1}$  that could be assigned to  $\text{Pt}^0\text{-CO}$ . To help us determine if it was feasible that a highly oxidized PtRu alloy structure would exhibit features attributable predominantly to  $\text{Ru}^{n+/0}$  species, we performed control experiments on monometallic Ru/ $\text{Al}_2\text{O}_3$  catalysts under the same conditions (see Supp. Info). The band positions and relative intensities of the oxidized PtRu alloy and oxidized monometallic Ru are very similar

suggesting that either the PtRu alloy catalyst has a surface that is initially enriched in Ru or that the oxidizing treatment may be inducing surface restructuring.

Another interpretation of the oxidized PtRu alloy DRIFT spectrum is that the band at  $2072\text{ cm}^{-1}$  is due to  $\text{Pt}^0\text{-CO}$  while the band at  $2126\text{ cm}^{-1}$  can be assigned to  $\text{Pt}^{2+}\text{-CO}$  and a similar interpretation as above can be made for the  $2013\text{ cm}^{-1}$  band. Due to the inherent heterogeneous nature of the PtRu alloy surface and the broadness of all the bands observed in the oxidized PtRu alloy spectra, a case can be made for the spectrum to be interpreted as a complex combination of oxidized and reduced species of both Pt and Ru existing at the surface. Similar DRIFT spectroscopy experiments were performed on monometallic Ru/ $\text{Al}_2\text{O}_3$  (see Supp. Info. 4.1). These spectra show that CO binds relatively weakly to oxidized Ru surfaces compared to metallic Ru surfaces. This leads us to believe that the oxidized PtRu alloy surface is dominated by metallic  $\text{Pt}^0\text{-CO}$  binding with minor contributions from oxidized Ru-CO binding.

In the case of the reduced PtRu alloy catalyst (Fig 4.3a1 and 4.3a3), a narrower band appears at  $2071\text{ cm}^{-1}$  along with a new feature at  $2035\text{ cm}^{-1}$  while the band at  $2127\text{ cm}^{-1}$  seen in the oxidized PtRu alloy spectrum disappears. The band at  $2035\text{ cm}^{-1}$  is often assigned to  $\text{Ru}^0\text{-CO}$ . Due to the narrowing of the band shape and slight blue-shift, we assign the  $2071\text{ cm}^{-1}$  band to  $\text{Pt}^0\text{-CO}$ . The relative intensities of the  $\text{Pt}^0\text{-CO}$  and  $\text{Ru}^0\text{-CO}$  would suggest that the surface is predominantly Ru rich but is more metallic in nature compared to the oxidized PtRu alloy catalyst. The loss of intensity at  $2127\text{ cm}^{-1}$  provides additional evidence that this feature is associated with an oxidized surface species.

#### 4.3.2.4 DRIFT Spectra of Oxidized and Reduced Ru@Pt Catalysts

Figure 4.3b shows CO adsorption DRIFT spectra at 120 °C after saturation CO coverage on Ru@Pt 1 wt% Pt/Al<sub>2</sub>O<sub>3</sub> catalysts that have been exposed to oxidizing (even numbers) and reducing (odd numbers) conditions. The oxidized Ru@Pt catalyst (Fig 4.3b2 and 4.3b4) has a main band centered at 2073 cm<sup>-1</sup> with a broad tail extending to lower energies. Two weak but distinguishable bands appear at 2117 cm<sup>-1</sup> and 2135 cm<sup>-1</sup> that are similar in relative intensity and overall breadth to the feature at 2125 cm<sup>-1</sup> seen in the oxidized PtRu alloy catalyst. Based on reports from literature, these features could arise from several different sources. The first important observation is that the oxidized PtRu alloy and oxidized Ru@Pt catalysts show very similar vibrational features. In the case of the Ru@Pt catalysts, this result would suggest that the underlying Ru core restructures and becomes surface accessible allowing Ru to oxidize and relegating some Pt to the near- or sub-surface region. Another interpretation of the oxidized Ru@Pt CO adsorption spectra is that the main band centered at 2072 cm<sup>-1</sup> is a combination of several bands including a shoulder at 2085 cm<sup>-1</sup> a main feature at 2072 cm<sup>-1</sup> and two broad, weak features at 2054 cm<sup>-1</sup> and 2020 cm<sup>-1</sup>. The 2085 cm<sup>-1</sup> shoulder can be assigned to Pt<sup>0</sup>-CO while the 2127 cm<sup>-1</sup> and 2072 cm<sup>-1</sup> bands can be assigned to the Ru<sup>n+</sup>(CO)<sub>x</sub> species described earlier. The two weak features at 2052 cm<sup>-1</sup> and 2075 cm<sup>-1</sup> can be assigned to Ru<sup>0</sup>(CO)<sub>2</sub> and Ru<sup>0</sup>-CO sites surrounded by a Ru<sup>n+</sup> matrix, respectively. A final interpretation is that the main band at 2072 cm<sup>-1</sup> could be assigned to Pt<sup>0</sup>-CO, while the tailing feature into the red would be indicative of CO binding on different surface Pt sites due to dilution by Ru brought to the surface by oxidation. CO adsorption DRIFT spectra of monometallic Ru (see Supp. Info. 4.1) show that oxidized Ru binds

CO poorly compared to reduced Ru based on band intensities. This result leads us to believe that the final interpretation – namely, the oxidized Ru@Pt CO binding is dominated by Pt<sup>0</sup> – is the most likely.

Upon reduction, a sharp feature centered at 2085 cm<sup>-1</sup> and a weaker, broad feature at 2020 cm<sup>-1</sup> are observed (Fig 3b1 and 3b3). We assign the 2085 cm<sup>-1</sup> band to Pt<sup>0</sup>-CO and the 2020 cm<sup>-1</sup> band to Ru<sup>0</sup>-CO. The EDS line scan data presented in Figure 4.2 suggest that under reducing conditions the surface of the Ru@Pt nanoparticle is decidedly Pt-rich. The attenuation of the main band of the reduced Ru@Pt at 2085 cm<sup>-1</sup> compared to the broad band of the oxidized Ru@Pt suggest that the surface is more homogeneous and likely dominated by metallic Pt. Furthermore, the blue-shift from 2071 cm<sup>-1</sup> in the oxidized Ru@Pt to 2085 cm<sup>-1</sup> in the reduced Ru@Pt may be indicative of dipole coupling of similar CO species on the Pt-dominant surface.

To summarize these results and interpretation, Figure 4.3c compares CO adsorption spectra from the reduced and oxidized states of the two bimetallic catalyst systems. CO adsorption spectra of the oxidized catalysts are strikingly similar suggesting similar surface structures dominated by Pt<sup>0</sup>-CO with minor contributions from Ru<sup>n+</sup>-CO species. Comparison of the CO adsorption spectra of the reduced catalysts suggests that the surface structures of these two catalysts are significantly different from each other. We interpret the reduced PtRu alloy surface to be dominated by a mixture of metallic Pt and Ru species and may be Ru-rich in nature based on relative band intensities. In contrast, the reduced Ru@Pt surface is Pt-rich as demonstrated by the attenuation and blue-shift of the main band at 2085 cm<sup>-1</sup>.

In the next section we will show that a surface structure-function relationship exists for these reduced and oxidized catalysts by performing catalytic studies under reducing (PROX) and oxidizing (CO oxidation) conditions that closely mimic the reduction-oxidation cycles used in the DRIFTS studies.

#### **4.3.3 Preferential CO Oxidation (PROX) and CO Oxidation Catalysis**

The goal in most efforts to design nanoparticles having specific compositions, architectures and/or shapes is to build enhanced activity or selectivity into the nanoparticle structure. Consequently, the first question that must be answered for a given bimetallic nanoparticle architecture is if the nanoparticle is stable under typical operating conditions. The second question is whether or not the nanoparticle shows the desired properties and do these properties scale with variables that can be readily controlled in a systematic way. Observations from the DRIFT spectroscopy of PtRu alloy and Ru@Pt catalysts would predict that the surface structures are stable, reproducible and reversible under catalytically relevant conditions. The DRIFT spectroscopy data would also predict that under oxidizing conditions, since the surface structures of the PtRu alloy and Ru@Pt catalysts are similar, that their catalytic activity should be similar for an oxidizing catalytic reaction. Conversely, under reducing conditions, the DRIFT spectroscopy results show that the PtRu alloy and Ru@Pt surfaces are dissimilar and we would expect that a reducing catalytic environment would exhibit different catalytic activities for the PtRu alloy and Ru@Pt catalysts. We chose the CO oxidation reaction as our catalytic test reaction to mimic oxidizing conditions and preferential CO oxidation (PROX) as our reducing mimic.

Temperature programmed reaction (TPR) plots of CO conversion for the PROX and CO oxidation reaction on PtRu alloy and Ru@Pt catalysts are presented in Figure 4.4. In all cases, the PROX TPR was first run from 40 °C to 210 °C at 1.8 °C/min and held isothermally for 30 minutes followed by an oxidative treatment at 210 °C for 30 minutes. The catalyst was then cooled down to room temperature under Ar. The CO oxidation TPR was then run with the same ramp rate and held isothermally for 30 minutes. An additional reducing treatment and PROX TPR was performed on the Ru@Pt catalyst. The time and temperature parameters used for the TPR profiles were chosen to mimic closely the conditions used in the preceding DRIFT spectroscopy analysis.

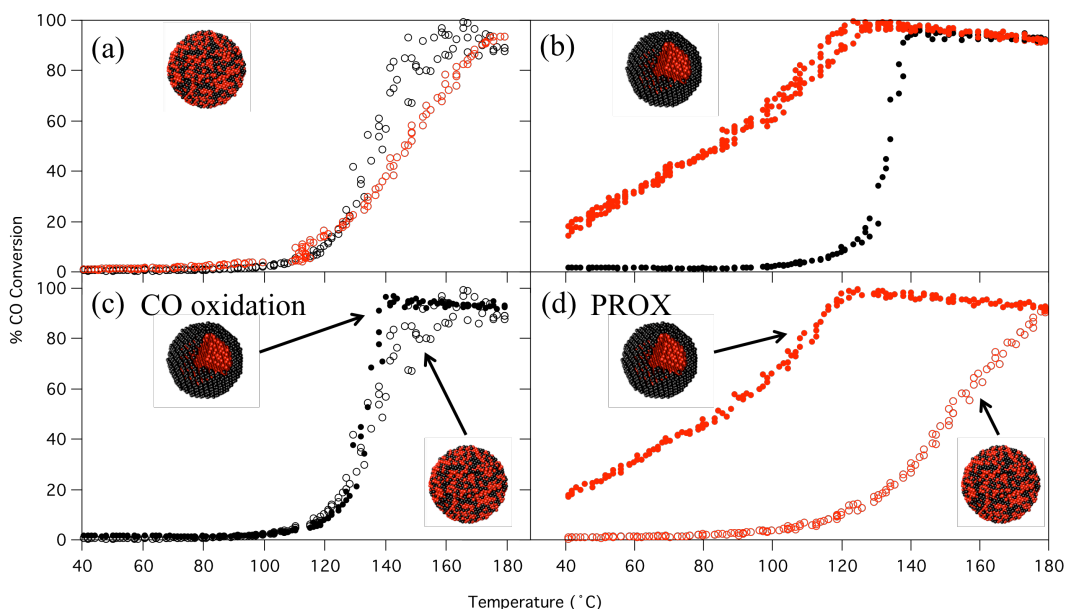


**Figure 4.4** TPR plots of CO oxidation (black) and PROX (red) for PtRu alloy (open circles) and Ru@Pt (filled circles) 1 wt% Pt/Al<sub>2</sub>O<sub>3</sub> catalysts. Conditions for PROX: 0.2% CO, 0.5% O<sub>2</sub>, 50% H<sub>2</sub>, 49.3% Ar and CO oxidation: 0.2% CO, 0.5% O<sub>2</sub>, 99.3% Ar. The total flow rate was 200 sccm and the temperature was ramped at a rate of 1.5 °C/min.

In the case of the PtRu alloy catalyst (Fig. 4.4a), initial light off for CO oxidation is not observed until  $\sim 110$  °C and 100% conversion occurs at  $\sim 170$  °C for both the PROX and CO oxidation reaction. Interestingly, although significantly different surface structures under oxidizing and reducing conditions are observed for the PtRu alloy based on DRIFTS results, their activity for CO oxidation is quite similar regardless of oxidation state. This may suggest that metallic Ru at the surface of the PtRu alloy nanoparticle plays little role in the CO oxidation mechanism. The traditional CO oxidation mechanism for Pt-Ru systems relies on a bifunctional surface where Pt binds CO and Ru provides oxophilic sites for oxygen species. This suggests that the ratio of Pt:Ru sites at the surface remains relatively constant since accessible Pt would need to remain constant, but the oxidation state of the surface Ru is changing based on the reactive atmosphere.

For the Ru@Pt catalyst (Fig. 4.4b), the initial PROX reaction showed CO oxidation light off near room temperature and reached 100% conversion at  $\sim 110$  °C. The subsequent CO oxidation TPR showed light off at 110 °C and 100% CO conversion at 130 °C. In the final step, the Ru@Pt catalyst was reduced and the PROX TPR was run again. The TPR of the second PROX reaction is almost identical to the first with only a slightly lower temperature for 100% conversion. The reversible nature of the catalytic activities for the two reactions is consistent with the reversibility observed in the DRIFTS studies. In the DRIFTS studies we suggested that the reduced Ru@Pt surface was dominated by metallic Pt while the oxidized Ru@Pt was still predominantly Pt-rich but that some oxidized Ru species existed at the surface. This subtle difference is interesting in light of the CO oxidation and

PROX catalytic activities. Figure 4.4b shows that the unique core@shell structure of Ru@Pt provides for enhanced catalytic activity under PROX conditions. This may be due to lattice contraction of the Pt shell caused by the underlying Ru that causes a shift in the d-band center and affects adsorbate binding strengths. This unique surface structure is not readily accessible in the case of the PtRu alloy even after long periods of reducing conditions. This may be possibly due to the severe entropic penalty that would be ensued by rearranging the random alloy structure to a core@shell structure.

Finally, the CO oxidation and PROX TPR plots for the two bimetallic systems are presented in Figure 4.4c and 4.4d, respectively. As predicted, similar CO oxidation activity is observed under CO oxidation (oxidizing) conditions while dissimilar CO oxidation activity is observed under PROX (reducing) conditions. These catalytic activity comparisons are in full agreement with our DRIFTS studies under similar conditions that showed similar surface structures under oxidizing conditions and different surface structures under reducing conditions. Figure 4.5 shows a schematic representation of the reduced and oxidized surface structures of the two bimetallic systems.

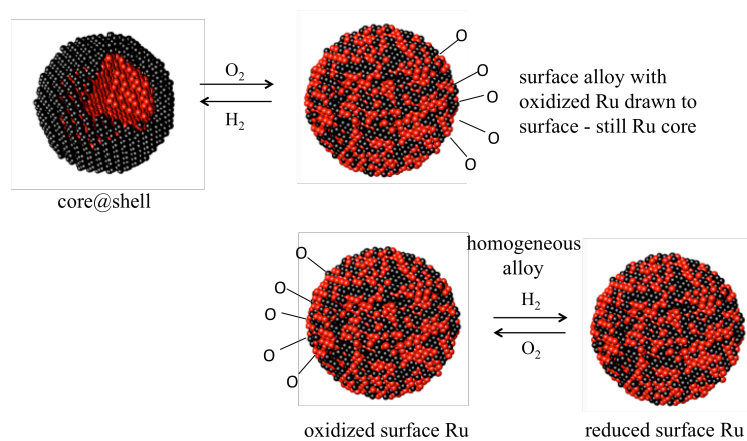


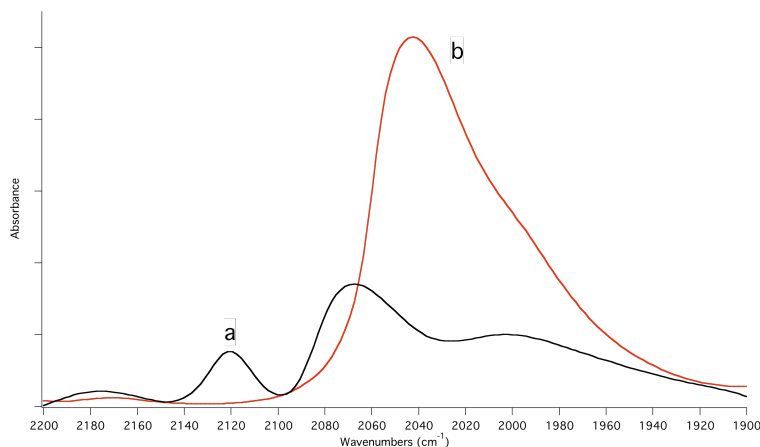
**Figure 4.5** Schematic representations of the surface states of Ru@Pt and PtRu alloy NPs under reducing and oxidizing conditions.

#### 4.4 Summary

Using CO adsorption DRIFT spectroscopy we have shown that oxidized state Ru@Pt and PtRu alloy catalysts show similar surface structures while reduced state Ru@Pt and PtRu alloy catalysts show significantly different surface structures. The differences and similarities in surface structure observed for the reduced and oxidized Pt-Ru systems correlate well with reducing catalytic reaction (PROX) and oxidizing catalytic reaction (CO oxidation) activities observed in temperature programmed reaction profiles (TPR), respectively. Repeated catalyst cycling shows that the different surface structures of the Ru@Pt and PtRu alloy catalysts are reversible over several reduction-oxidation cycles.

Interestingly, while the PROX activities of Ru@Pt and PtRu alloy catalysts are quite dissimilar, both reduced state catalysts have accessible Pt<sup>0</sup> and Ru<sup>0</sup> species at the surface. Mavrikakis and coworkers have proposed a hydrogen-assisted CO oxidation mechanism whereby changes in the electronic structure of the surface Pt layer due to lattice strain creates a low energy pathway to oxygen dissociation via hydroperoxy intermediate.<sup>17</sup>

## 4.5 Supplemental Information



**Supplemental Information 4.1** Comparison of CO adsorption DRIFTS of monometallic Ru/Al<sub>2</sub>O<sub>3</sub> catalyst. (a) oxidized state and (b) reduced state.

## 4.6 References

- (1) Ponec, V.; Bond, G. C. *Catalysis by Metals and Alloys*; Elsevier: Amsterdam, 1995;
- (2) Sinfelt, J. H. *Bimetallic Catalysts: Discoveries, Concepts and Applications*; John Wiley & Sons: New York, 1983;
- (3) Park, J. Y.; Zhang, Y.; Grass, M.; Zhang, T.; Somorjai, G. A. *Nano Lett.* **2008**, *8*, 673-677.
- (4) Habas, S. E.; Lee, H.; Radmilovic, V.; Somorjai, G. A.; Yang, P. *Nat Mater* **2007**, *6*, 692-697.
- (5) Somorjai, G. A.; Park, J. Y. *J. Chem. Phys.* **2008**, *128*, 182504.
- (6) Xiao, L.; Zhuang, L.; Liu, Y.; Lu, J.; Abruna, H. D. *J. Am. Chem. Soc.* **2009**, *131*, 602-608.
- (7) Campbell, C. *Science* **2002**, *298*, 811-814.
- (8) Aiken, J. D.; Finke, R. G. *J Mol Catal A-Chem* **1999**, *145*, 1-44.

- (9) McClure, S. M.; Goodman, D. W. *Chem. Phys. Lett.* **2009**, *469*, 1-13.
- (10) Nilekar, A. U.; Mavrikakis, M. *Surf. Sci.* **2008**, *602*, L89-L94.
- (11) Niemantsverdriet, J. W. *Spectroscopy in Catalysis*; Wiley-VCH: Weinheim, 2007;
- (12) Kowal, A.; Li, M.; Shao, M.; Sasaki, K.; Vukmirovic, M. B.; Zhang, J.; Marinkovic, N. S.; Liu, P.; Frenkel, A. I.; Adzic, R. R. *Nat Mater* **2009**, *8*, 325-330.
- (13) Lang, H.; Maldonado, S.; Stevenson, K.; Chandler, B. *J. Am. Chem. Soc.* **2004**, *126*, 12949-12956.
- (14) Bradley, J. S.; Hill, E. W.; Chaudret, B.; Duteil, A. *Langmuir* **1995**, *11*, 693-695.
- (15) Ma, T.; Fu, Q.; Su, H.; Liu, H.; Cui, Y.; Wang, Z.; Mu, R.; Li, W.; Bao, X. *ChemPhysChem* **2009**, *10*, 1013-1016.
- (16) Mu, R.; Fu, Q.; Liu, H.; Tan, D.; Zhai, R.; Bao, X. *Appl. Surf. Sci.* **2009**, *255*, 7296-7301.
- (17) Alayoglu, S.; Nilekar, A.; Mavrikakis, M.; Eichhorn, B. *Nat Mater* **2008**, *7*, 333-338.
- (18) Zhou, S. H.; Varughese, B.; Eichhorn, B.; Jackson, G.; McIlwrath, K. *Angew Chem Int Edit* **2005**, *44*, 4539-4543.
- (19) Rauscher, H.; Hager, T.; Diemant, T.; Hoster, H.; De, Buatier, M., F.; Behm, R. *J. Surf. Sci.* **2007**, *601*, 4608-4619.
- (20) Chin, S. Y.; Alexeev, O. S.; Amiridis, M. D. *J. Catal.* **2006**, *243*, 329-339.

- (21) Alexeev, O. S.; Chin, S. Y.; Engelhard, M. H.; Ortiz-Soto, L.; Amiridis, M. D. *J. Phys. Chem. B* **2005**, *109*, 23430-23443.
- (22) Alexeev, O. S.; Chin, S. Y.; Engelhard, M. H.; Ortiz-Soto, L.; Amiridis, M. D. *J. Phys. Chem. B* **2005**, *109*, 23430-23443.
- (23) Schlapka, A.; Kasberger, U.; Menzel, D.; Jakob, P. *Surf. Sci.* **2002**, *502*, 129-135.
- (24) Chin, S. Y.; Williams, C. T.; Amiridis, M. D. *J. Phys. Chem. B* **2006**, *110*, 871-882.
- (25) Mazzieri, V.; Coloma-Pascual, F.; Arcoya, A.; L'Argentiere, P.; Figoli, N. S. *Appl. Surf. Sci.* **2003**, *210*, 222-230.
- (26) Baird, A. S.; Kross, K. M.; Gottschalk, D.; Hinson, E. A.; Wood, N.; Layman, K. A. *J. Phys. Chem. C* **2007**, *111*, 14207-14214.
- (27) Assmann, J.; Loffler, E.; Birkner, A.; Muhler, M. *Catal. Today* **2003**, *85*, 235-249.
- (28) Alayoglu, Selim. Ph.D. Thesis, University of Maryland, College Park, MD, 2008.

## Chapter 5: Cu@Pt (core@shell) Nanoparticles: Synthesis and Characterization

### 5.1 Introduction

Recent experiments and DFT calculations show that bimetallic nanoparticles with (core@shell) architectures can be vastly superior to their alloy counterparts for a variety of industrially relevant heterogeneous transformations.<sup>1-3</sup> Previously our group focused on the Pt-Ru bimetallic system to compare the properties and catalytic activities of core@shell and alloy architectures.<sup>4</sup> In that work, a systematic study comparing the preferential CO oxidation (PROX) activities and selectivities of PtRu alloy and Ru@Pt nanoparticles showed that the unique architecture of the Ru@Pt nanoparticles was superior to the alloy architecture despite the fact that the nanoparticles had the same size, shape and atomic Pt:Ru ratio. To understand the origin of this behavior one can begin by considering planar systems.

Goodman and coworkers performed XPS studies of 1 ML thick overlayers on single crystal metals to determine what effect the underlying substrate would have on the surface metal. Their work showed that the core level binding energies of the surface metal shifted relative to its single crystal monometallic counterpart. This shift in surface electronic structure was correlated to adsorption energies of CO on the same surfaces.<sup>5,6</sup> DFT calculations from the Norskov and Mavrikakis groups suggest that thin layers of one metal over a second metal causes stress or strain on the near-surface atoms.<sup>7,8</sup> This stress or strain shifts the d-band center that affects the binding energy of molecular and atomic reactants and intermediates. By tuning the d-band center based on the bimetallic  $M_1$ - $M_2$  combination used, one can begin to

predictively choose the rational design of catalysts based on the specific desired binding energies of key intermediates.

The catalytically relevant analogue of these overlayer surfaces is the (core@shell) nanoparticle where a thin layer (1-2 ML) of one metal is deposited over a preformed nanoparticle. In order to bridge the gap between theory, ideal surfaces and catalysis, a better understanding of core@shell nanoparticle synthesis must be achieved. Although mechanisms for core@shell nanoparticle formation are still debated, several examples of well-characterized core@shell nanoparticles do exist. For instance, Cheon and coworkers synthesized 8 nm Co@Pt nanoparticles by a transmetallation mechanism whereby surface Co atoms of a preformed Co nanoparticle were involved in a redox couple that reduced Pt at the surface.<sup>9, 10</sup> Toshima and coworkers used surface hydride on preformed Pd nanoparticles to reduce Pt to form Pd@Pt nanoparticles.<sup>11</sup> Ru@Pt has been thoroughly characterized by XRD, FTIR-CO and XPS. This last example is work from our group that showed Ru@Pt could only be synthesized using Ru@RuO<sub>2</sub> nanoparticle cores. By using strict oxygen free synthesis conditions, fully metallic Ru nanoparticles were synthesized but Pt would not coat the surface of these nanoparticles to form the Ru@Pt structure.<sup>4</sup> These and other examples show that the core@shell nanoparticle architecture is complex and that several pathways may exist for their formation. The complexity of core@shell nanoparticles emphasizes the need for the careful characterization of their intermediates and products in order to understand the mechanism of shell metal deposition on small core nanoparticles and move beyond the largely empirical methods currently used.

This chapter presents the synthesis and time-lapsed characterization of Cu@Pt (core@shell) nanoparticles. Here, “time-lapsed” refers to *ex situ* measurements carried out with aliquots of the nanoparticle removed at different stages of the reactions progress. We found that Pt shells cover the metallic Cu core nanoparticles to form Cu@Pt while Pt growth is inhibited at the CuO surface. Furthermore, the combined time-lapse UV-Vis, FTIR-CO and XRD measurements used to observe Pt coating Cu core nanoparticles shows that the surface plasmon resonance (SPR) of Cu nanoparticles is easily quenched by even small amounts of Pt coating the surface. We propose that a transmetalation mechanism is responsible for the formation of Cu@Pt nanoparticles based on the time-lapse characterization of the deposition of Pt onto Cu nanoparticles.

Finally, Raman spectroscopy was used to investigate how changes in the surface plasmon resonance (SPR) band of Cu caused by the addition of a partial Pt shell overlayer affect their visible light absorption efficiencies. We found a striking correlation between the relative absorbance of 488 nm versus 633 nm light for Cu and Cu@Pt nanoparticles and their ability to form graphite deposits on their surfaces.

## 5.2 Experimental

### **5.2.1 Synthesis of Cu@Pt (core@shell) Nanoparticles**

A modified synthesis previously reported by our group was used to make Cu nanoparticles and subsequent Cu@Pt (core@shell) nanoparticles.<sup>12</sup> Briefly, 22.2 mg (0.085 mmol) Cu(acetylacetonate)<sub>2</sub>, 159.1 mg polyvinylpyrrolidone (PVP) (55000 MWT) and 20 mL of 1,4 butanediol were mixed in a 100 mL 3-neck RBF with a

Teflon stirbar. The mixture was purged under vacuum at 80 °C for 10 minutes to remove impurities. The mixture was then placed under N<sub>2</sub> atmosphere while heating at ~10 °C/min to 185 °C. A red colloidal suspension indicative of Cu nanoparticle formation was observed at 185 °C. The suspension was further heated for 5 minutes before cooling to room temperature under N<sub>2</sub> in a cold water bath. 33.2 mg (0.125 mmol) PtCl<sub>2</sub> was then added to the Cu nanoparticle suspension and the mixture was slowly heated (~2 °C/min) to 185 °C under N<sub>2</sub>. The suspension turned from dark red to black indicating the reduction of Pt<sup>2+</sup> to Pt<sup>0</sup>. The black suspension was further heated for 2 hours and finally cooled to room temperature in a cold water bath.

### **5.2.1 Synthesis of Cu@CuO (core@shell) Nanoparticles**

A modified version of the Cu nanoparticle synthesis described in the previous section was used to obtain Cu@CuO nanoparticles. Once Cu nanoparticles were formed at 185 °C, the colloid was further heated at 185 °C for 1 hour. The color of the nanoparticle suspension changed from red to deep purple. This suspension was cooled to room temperature under N<sub>2</sub> atmosphere in a cold water bath.

### **5.2.2 Characterization**

#### *5.2.2.1 Transmission Electron Microscopy*

TEM samples were prepared by diluting ~200 µL of the colloidal suspension in ~1 mL 1-propanol or deionized water. 5 µL of this mixture was drop-cast and dried on continuous carbon film-deposited copper or nickel grids. A JEM 2100 LaB6 TEM operating at 200 kV was used for both low and high-resolution imaging.

#### 5.2.2.2 *Fourier Transform IR – CO Probe*

For the IR-CO probe experiments, the Cu and Cu@Pt colloidal suspension was bubbled with CO using a stainless steel needle submerged in the suspension at a flow rate of 35 sccm for 10 minutes. A 100  $\mu$ L aliquot of CO saturated colloidal suspension was filled in a liquid IR cell and monitored in a Nexus 870 FT-IR spectrometer. The liquid IR cell consisted of a 0.5 mm Teflon spacer sandwiched between two rectangular CaF<sub>2</sub> windows. The colloidal suspension prior to CO bubbling was used for the background spectra.

#### 5.2.2.3 *Powder X-ray Diffraction*

A Bruker C2 Discover (Parallel Beam) General Area Diffraction Detection (GADDS) system was used for powder diffraction detection. The monochromatic Cu K $\alpha$  radiation source that was biased at 40 mV and 40 mA was employed along with Bruker ACS Hi-Star detector. The diffraction patterns were acquired between 33-90° by integrating four frames with 14° 2 $\theta$  per frame while the sample was oscillated in the XY plane to provide more homogeneous signal acquisition. Nanoparticle samples were prepared by washing 3 mL aliquots of the native Cu and Cu@Pt suspension in acetone and centrifuging at 6000 RPM for 10 minutes to separate the nanoparticles from solution by decanting the clear supernate. The wash/centrifuge procedure was repeated and finally the nanoparticle powders were dried in a 60 °C oven for ~1 hour before XRD analysis. Unsupported nanoparticle powders were pressed onto a glass slide for XRD analysis.

#### 5.2.2.4 *UV-Vis*

A Hitachi 3010 S spectrometer was used to collect UV-Vis spectra. Low volume 5 mm path length quartz cuvettes were used to collect spectra in the 250-700 nm range. The colloidal suspension of either Cu or Cu@Pt was washed with acetone and centrifuged at 6000 RPM for 10 minutes to separate the nanoparticles from solution by decanting the clear supernate. The nanoparticles were then diluted with spectroscopic grade methanol and the mixture was sonicated until a colloidal suspension was formed. The suspension was diluted with methanol until the maximum absorbance was below 1.0. Neat spectroscopic grade methanol was used as the blank.

#### 5.2.2.5 *micro-Raman*

A Renishaw In Via micro-Raman spectrometer was used to acquire vibrational spectra. The spectrometer is equipped with a 633 nm HeNe laser as well as a 488 nm Ar ion laser, and both operated with powers between 2.5 to 25 mW with a minimum spot size of ~1 mm. Sample focusing was optimized with 50X confocal lens objective adapted to a Leica microscope.

NP samples were prepared by pressing ~5 mg of washed and dried nanoparticle powders onto glass slide substrates. Typical collection times for Raman measurements were 2-10 minutes in open air.

## 5.3 Results and Discussion

### **5.3.1 Synthesis**

Several interesting transformations were observed during the synthesis of Cu nanoparticles. First, the light blue solution indicative of a  $\text{Cu}^{2+}$  turned to lime green at 120 °C. This color change is likely due to the reduction of  $\text{Cu}^{2+}$  to  $\text{Cu}^+$ . The green solution gradually became darker and more turbid until a black suspension was formed at 170 °C. Unfortunately, attempts to characterize this black intermediate state by TEM or FTIR-CO probe failed. We speculate that this dark suspension is  $\text{Cu}^0$  nuclei that form small clusters and serve as the seeds for further growth and formation of the Cu nanoparticle end product. Attempts to cool the black suspension to room temperature resulted in the formation of a green solution likely indicating oxidation of the clusters back to  $\text{Cu}^+$ . Upon further heating, the suspension turned from black to brick red within 5 seconds at 185 °C. These observations are consistent with nucleation-growth mechanisms commonly proposed whereby a threshold concentration of zero-valent atoms or small clusters must be reached before a burst of nucleation and subsequent nanoparticle growth occurs.<sup>13</sup> Upon further heating at 185 °C, the Cu colloidal suspension gradually turns from red to blue-purple over the course of 60 minutes. We believe that this further heating causes oxidation of the surface of the Cu nanoparticles to form  $\text{Cu}@\text{CuO}$  nanoparticles.

Upon adding  $\text{PtCl}_2$  to the initially formed Cu nanoparticle suspension and heating the mixture slowly from room temperature to 185 °C, a color change from red to black is observed at 120 °C. This observation is consistent with the formation of a  $\text{Pt}^0$  shell around the Cu nanoparticles. Interestingly, if  $\text{PtCl}_2$  is added to the  $\text{Cu}@\text{CuO}$

nanoparticle suspension and heated slowly to 185 °C, no color change is observed at 120 °C. Instead, an abrupt change from blue-purple to brown/black is observed at ~150 °C. This is approximately the same temperature for monometallic Pt nanoparticle formation under similar conditions. This would suggest that the CuO shell prohibits Pt growth at the surface. One possible explanation for this behavior is that transmetalation of Cu occurs at the Cu nanoparticle surface whereby surface Cu<sup>0</sup> atoms are oxidized and Pt<sup>2+</sup> is reduced at the surface. Conversely, Cu@CuO surface sites cannot be oxidized further to reduce Pt<sup>2+</sup>. Cheon and coworkers reported on this phenomenon for the Co@Pt nanoparticle system.<sup>10</sup> Another possibility is that differences in lattice parameters between Cu (3.62 Å) and CuO (4.68 Å) are significant enough to promote Pt deposition on Cu but prohibit Pt deposition on CuO.

### 5.3.2 TEM

TEM images of Cu and Cu@Pt nanoparticles are presented in Figure 1 along with histograms of nanoparticle size based on  $\geq 100$  particles. Cu nanoparticles are 2.8 nm in diameter, relatively monodisperse but non-uniformly round in shape. Attempts to grow larger Cu nanoparticles by changing PVP/Cu(acetylacetonate)<sub>2</sub> ratios resulted in a high degree of polydispersity. The TEM image in Figure 5.2a shows initial Cu

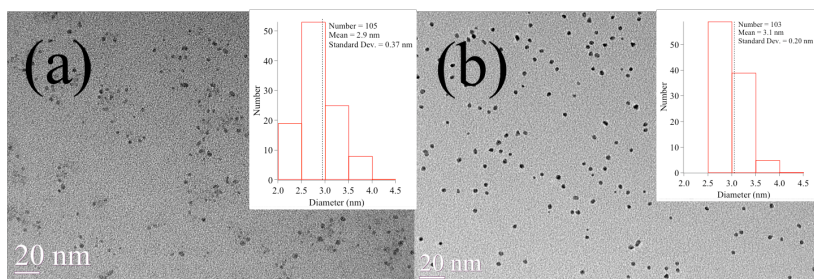


**Figure 5.1** TEM images of (a) Cu and (b) Cu@Pt nanoparticles with histograms.

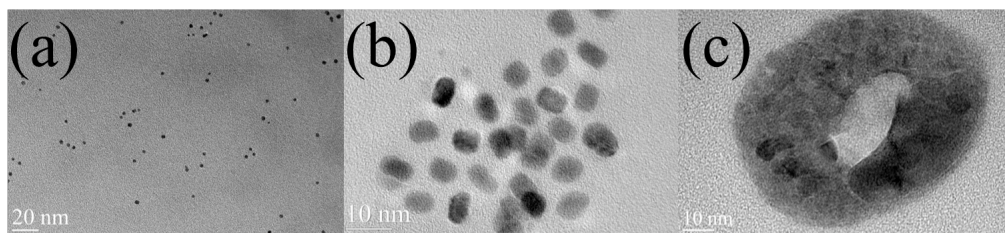


**Figure 5.2** TEM images of (a) Cu nanoparticles, (b) Cu nanoparticles after 30 min. reflux and (c) Cu nanoparticles after 60 minutes reflux.

Cu nanoparticles similar to those in Fig. 5.1a. After 30 minutes of reflux the Cu nanoparticles grow to  $\sim 8$  nm in diameter (Fig. 5.2b). The larger size of the Cu nanoparticles seen in Figure 5.2b suggests that an oxide shell grows on the initial Cu nanoparticle cores over time. After 60 minutes of reflux the large particles aggregate to form  $\sim 150$  nm diameter clusters as seen in Figure 5.2c. The large aggregates appear to contain smaller domains that are the same size as the nanoparticles in Figure 5.2b.

### 5.3.3 FTIR-CO

Figure 5.3 shows FTIR-CO spectra for Cu and Cu@CuO nanoparticles. Over the course of 60 minutes the main spectral feature initially observed at  $2086\text{ cm}^{-1}$

disappears and a new band appears at  $2109\text{ cm}^{-1}$ . The band at  $2086\text{ cm}^{-1}$  can be

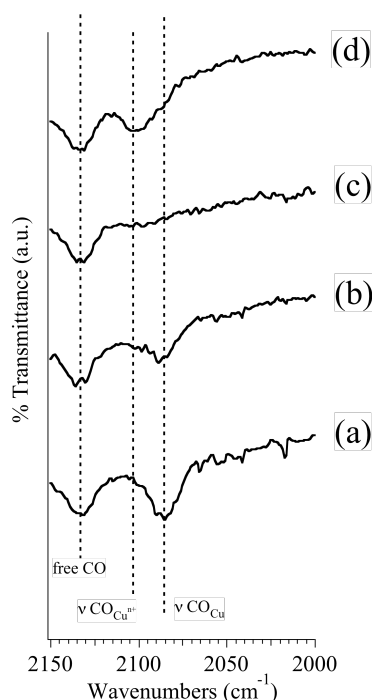


**Figure 5.3** Time lapse FTIR-CO of Cu and Cu@CuO nanoparticles (a) 1 minute, (b) 15 minutes, (c) 30 minutes and (d) 60 minutes reflux after Cu nanoparticle formation. assigned to CO bound linearly to  $\text{Cu}^0$  sites on the surface of the nanoparticle while the band at  $2109\text{ cm}^{-1}$  can be assigned to CO bound linearly to  $\text{Cu}^{n+}$  sites.<sup>14, 15</sup> Interestingly, the  $2109\text{ cm}^{-1}$  band appears only after the  $2086\text{ cm}^{-1}$  band disappears. This may suggest that metallic Cu nanoparticles first coalesce into larger Cu nanoparticles followed by surface oxidation. Although we use Schlenk techniques under  $\text{N}_2$  atmosphere for the syntheses of these nanoparticles, oxidation may still occur due to water content in the solvents. The observed color change, the spectral evolution of the CO vibrational features and their subsequent assignments are consistent with our hypothesis that a CuO shell grows over the preformed Cu nanoparticles to form Cu@CuO nanoparticles. As stated in the previous section,

attempts to form a Pt shell over Cu@CuO nanoparticles resulted in monometallic Pt nanoparticle formation characterized by FTIR-CO probe (see Supp. Info 5.1).

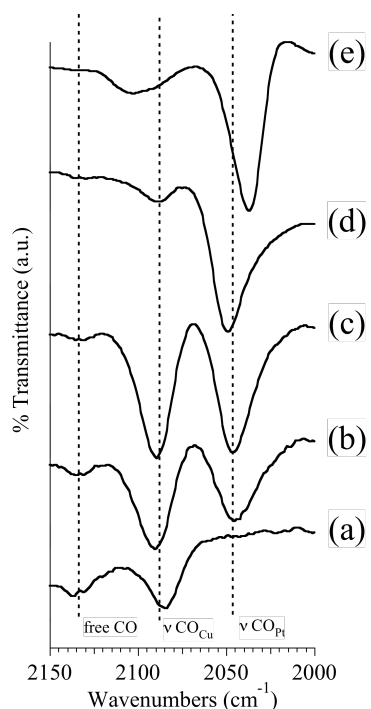


**Figure 5.4** Time lapse FTIR-CO of (a) initial Cu nanoparticles, (b) 15 minutes, (c) 30 minutes, (d) 60 minutes and (e) 130 minutes after the addition of PtCl<sub>2</sub> and heating.

Figure 5.4 shows FTIR-CO spectra for Cu nanoparticles and time-lapsed spectra of Cu@Pt nanoparticles. After the addition of PtCl<sub>2</sub> and subsequent heating, a band at 2048 cm<sup>-1</sup> begins to grow in while the band at 2086 cm<sup>-1</sup> previously assigned to Cu-CO<sub>linear</sub> initially increases and then decreases over time. The band at 2048 cm<sup>-1</sup> can be assigned to CO bound linearly to Pt<sup>0</sup>. While the initial increase of intensity of the 2086 cm<sup>-1</sup> band cannot currently be explained, the increase in the 2048 cm<sup>-1</sup> band and overall decrease in the 2086 cm<sup>-1</sup> is consistent with the growth of a metallic Pt shell over the Cu nanoparticle core. Finally after 130 minutes at 185 °C, the band at 2048 cm<sup>-1</sup> red-shifts to 2039 cm<sup>-1</sup> and a combination of bands assigned to Cu<sup>n+</sup>-CO<sub>linear</sub> and Cu<sup>0</sup>-CO<sub>linear</sub> are observed at 2109 and 2086 cm<sup>-1</sup>, respectively

(Fig. 5.4e). Interestingly, the combination of bands assigned to  $\text{Cu}^{n+/0}\text{-CO}_{\text{linear}}$  are present even after heating the Cu@Pt nanoparticle colloid for long times (>130 min.). This suggests that Cu is still accessible at the surface of the nanoparticle even though enough  $\text{Pt}^{2+}$  precursor was added to coat the Cu nanoparticles with 2 ML of Pt. This result could be explained by considering our earlier proposal that a transmetalation mechanism is responsible for the deposition of Pt onto Cu nanoparticle surfaces. If surface Cu is oxidized to  $\text{Cu}^{2+}$ , which would presumably be in solution, then  $\text{Cu}^{2+}$  may reduce again on the Cu@Pt nanoparticle. This would explain why a small amount of surface  $\text{Cu}^{n+/0}$  is still observed by the FTIR-CO probe experiment.

Literature reports of CO bound to monometallic Pt and Pt in Cu-Pt systems show that the  $\text{Pt-CO}_{\text{linear}}$  band for our Cu@Pt nanoparticles is highly red-shifted by comparison.<sup>16</sup> As a control experiment, we prepared monometallic Pt nanoparticles of similar size and shape and performed the FTIR-CO probe experiment (see Supp. Info. 5.2). The band for  $\text{Pt-CO}_{\text{linear}}$  appears at  $2070\text{ cm}^{-1}$  and is consistent with other literature reports for monometallic Pt nanoparticles. One way to interpret the dramatic red-shift of the  $\text{Pt-CO}_{\text{linear}}$  band for the Cu@Pt nanoparticles is to note that Cu sites remain present on the Cu@Pt nanoparticle surface. This dilution by Cu would disrupt dipole-dipole coupling of CO bound to surface Pt and lead to the observed red-shift.<sup>17</sup>

### 5.3.4 UV-Vis

Figure 5.5 shows time-lapsed UV-Vis spectra of Cu and Cu@Pt nanoparticles. The band observed at  $\sim 565\text{ nm}$  in the initial Cu nanoparticle spectrum (Fig. 5.5a) is due to the surface plasmon resonance (SPR) of Cu nanoparticles. The SPR band disappears completely upon the addition of surface Pt to the Cu nanoparticles as seen

in Figure 5.5b-e. The featureless slope observed in these spectra are similar to that of monometallic Pt. Based on the FTIR-CO probe experiment we know that the surface

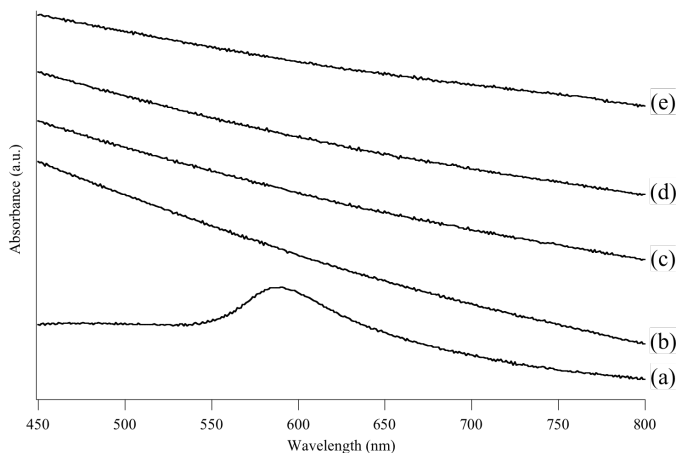


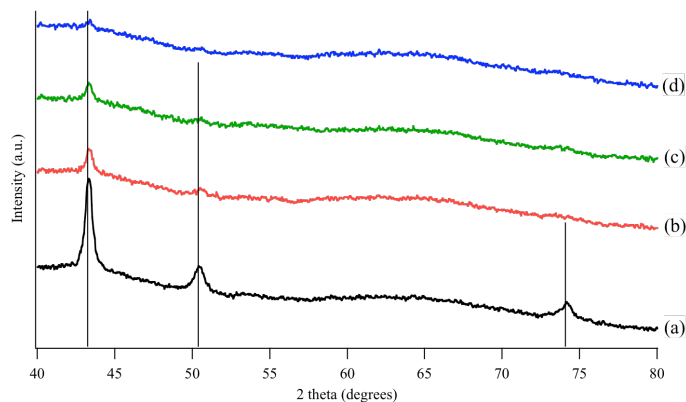
**Figure 5.5** Time-lapse UV-Vis of (a) initial Cu nanoparticles, (b) Cu@Pt (15 minutes), (c) Cu@Pt (30 minutes), (d) Cu@Pt (120 minutes) and (e) Cu@Pt (overnight).

of the nanoparticle is predominantly  $\text{Cu}^0$  15 minutes after the addition of  $\text{Pt}^{2+}$  to the Cu nanoparticles. This suggests that even small amounts of surface Pt on the Cu nanoparticles disrupts the surface electronic structure that gives rise to the visible-SPR phenomenon. This result may also give further credence to the transmetalation mechanism proposed in the previous sections. If surface Cu oxidation is a requirement for the deposition and reduction of  $\text{Pt}^{2+}$ , then it is likely that the initial Pt is highly intercalated in the near-surface region of the nanoparticle and thus would be more likely to disrupt the surface electron structure of the Cu nanoparticle.

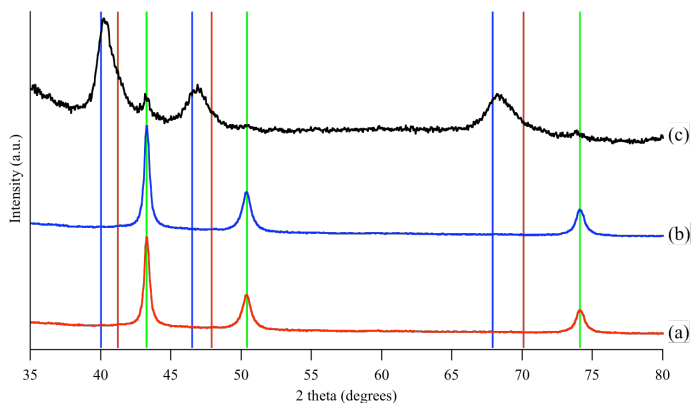
### 5.3.5 XRD

Figure 5.7 shows XRD patterns of Cu and Cu@CuO nanoparticles. Diffraction from metallic Cu is observed in the case of the initial Cu nanoparticles and diminishes upon Cu@CuO formation. After 15-60 minutes of heating at 185 °C,

no diffraction is observed for the CuO species of Cu@CuO that was identified by



**Figure 5.6** Time-lapse XRD of Cu and Cu@CuO nanoparticles (a) 1 minute, (b) 15 minutes, (c) 30 minutes and (d) 60 minutes reflux after Cu nanoparticle formation. Black vertical lines represent ideal diffractions of Cu.



**Figure 5.7** Time-lapse XRD of (a) Cu nanoparticles, (b) Cu@Pt (30 minutes), (c) Cu@Pt (60 minutes). Blue, red and green vertical lines represent ideal diffractions of Pt, PtCu(50:50) and Cu, respectively.

FTIR-CO probe experiments (see Fig. 5.3) while the diffraction due to metallic Cu is highly diminished. The fact that we do not observe CuO diffraction is likely due to the non-crystalline nature of the CuO shell.

Figure 5.8 shows XRD patterns of Cu@Pt nanoparticles. Figure 5.8a shows that the initial Cu nanoparticles exhibit diffraction peaks that match bulk metallic Cu. Figure 5.8b shows that upon addition of  $\text{Pt}^{2+}$  and subsequent heating, no diffraction is

observed for metallic Pt even though the FTIR-CO and UV-Vis data show clearly that Pt exists at the Cu nanoparticle surface under the same conditions. A likely explanation is that the Pt on the surface at these early times will be highly dilute or in small islands on the surface and thus non-diffracting due to its non-crystalline nature or lack of long range order. Figure 5.8c shows that metallic Pt diffraction is present after longer periods of heating at 185 °C. Also present in Figure 5.8c are diffraction peaks from Cu and CuPt alloy. This result is consistent with the Cu@Pt nanoparticle architecture with a complete Pt shell where some alloying at the interface of Cu and Pt would be expected. The diffraction due to the CuPt alloy is very broad and suggests a non-homogeneous mixing of Cu and Pt at the interface. Again, considering transmetalation as a probable mechanism for Pt deposition on Cu nanoparticle surfaces, we can imagine that there should initially be ample mixing of Cu and Pt at the surface of the Cu nanoparticles due to initial oxidation of surface Cu.

### **5.3.5 micro-Raman**

We have shown by time-lapsed characterization experiments that Pt will coat Cu nanoparticles to form Cu@Pt but Pt deposition is prohibited on Cu@CuO surfaces. The FTIR-CO probe experiments show a monotonic decrease in the Cu-CO band relative to the Pt-CO band over time. Cu still remains at the surface because the Cu-CO mode remains even after long reaction times. This behavior suggests that Pt coats the surface of Cu nanoparticles throughout the course of the synthesis, but Cu remains accessible possibly due to re-deposition of Cu onto the surface of the Cu@Pt nanoparticle. The source of the Cu in the latter stages of the synthesis may come from Cu that was oxidized during initial Pt deposition.

The time-lapse XRD measurements do not show the initial Pt deposition observed in the FTIR-CO experiments. Instead, only diffraction peaks due to monometallic Cu are observed until the late stages of the synthesis where Pt, Cu and PtCu alloy diffractions appear. This suggests that initially deposited Pt does not have the long range order or crystallinity required to observe diffraction. Only after larger domains of Pt coat the Cu nanoparticle surface does Pt diffract.

Finally the time-lapse UV-Vis measurements show that even small amounts of Pt deposited on the surface of Cu nanoparticles is adequate to disrupt the SPR band of Cu. Even after just 15 minutes of Pt deposition time was the SPR quenched. The UV-Vis spectra from that point forward exhibited band shapes similar to monometallic Pt nanoparticles. Based on the drastic change in the absorbance profile of Cu compared to Cu@Pt nanoparticles, we surmised that the two structures might be differentiated based on their ability to transform light into heat. We saw in Chapter 2 that Pt nanoparticles can readily transform PVP into graphitic deposits near its surface when heated to moderate temperatures. Furthermore, Somorjai and coworkers have studied how PVP degrades into carbonaceous (graphitic) deposits on the surface of Pt nanoparticles when exposed to heating by the focused laser source of a Raman spectrometer. If we consider the concentrated (1  $\mu\text{m}$  spot size) visible laser used in our Raman spectrometer as a heat source for nanoparticles, then we should be able to qualitatively predict the nanoparticle's efficiency for transforming concentrated visible light into heat by comparing the relative absorbances of 488 nm and 633 nm light for a given nanoparticle. In the present study, we show that this thermal energy can transform PVP coating the nanoparticle surface into graphite

based on the nanoparticles relative absorbance of 488 and 633 nm laser light as determined from the UV-Vis measurements presented in section 5.3.4.

Figure 5.9 shows Raman spectra of Cu, Pt and two Cu@Pt nanoparticles collected with both 488 nm (Fig. 5.9 I) and 633 nm (Fig. 5.9 II) excitations. Cu nanoparticles in Figure 5.9Ia show three bands centered at 1660, 1480 and 1424  $\text{cm}^{-1}$  that are the same as those of neat PVP (see Supp. Info 5.2). The combination of 1660 and 1480  $\text{cm}^{-1}$  can be assigned to C=O and C-N stretching commonly referred to as the amide I and II bands while the 1424  $\text{cm}^{-1}$  feature can be assigned to  $\text{CH}_2$  scissoring.<sup>18</sup> Moving down column I, spectra of Pt nanoparticles (Fig. 5.9Ib) and two Cu@Pt nanoparticles (Fig. 5.9Ic-d) show bands centered at 1340 and 1580  $\text{cm}^{-1}$  that

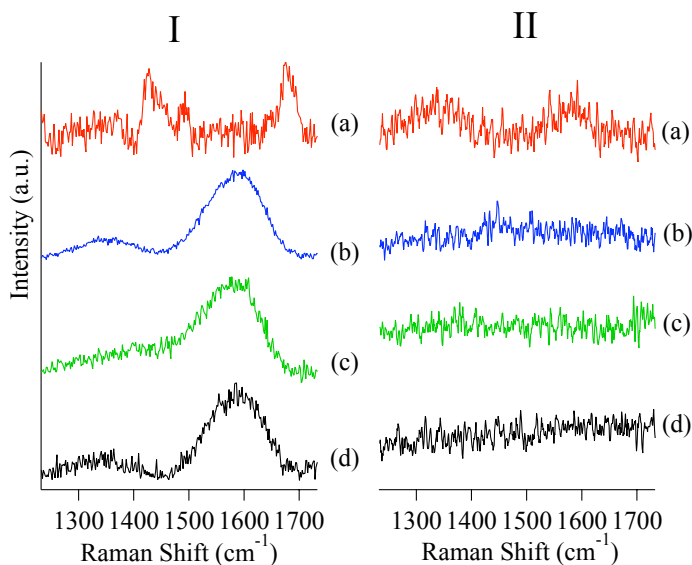


**Figure 5.8** Raman spectra of (a) Cu nanoparticles, (b) Pt nanoparticles (c) Cu@Pt (30 minutes) and (d) Cu@Pt (60 minutes). Spectra in column I were acquired with 488 nm (1 mW) excitation and column II with 633 nm (0.4 mW) excitation.

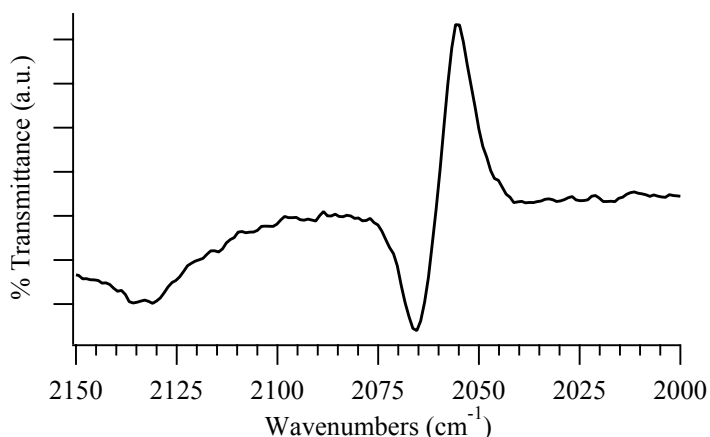
are consistent with the D and G bands of disordered and ordered graphite, respectively.<sup>19</sup> As proposed above, the formation of graphite results from local

heating of nanoparticles by absorbing light. Based on the UV-Vis absorbance profiles of Cu, Cu@Pt and Pt nanoparticles, Figure 5.8I shows that Cu@Pt has a similar propensity to generate graphite from PVP as monometallic Pt. This result suggests that by adding even small amounts of Pt to the Cu nanoparticle surface, the nanoparticle's ability to absorb visible light that is transformed into heat has been altered significantly. A similar series of Raman spectra are presented in Figure 5.9II where 633 nm excitation is used. Completely opposite of the case for 488 nm excitation, Cu nanoparticles show bands consistent with graphite formation and Pt and Cu@Pt nanoparticles show no traces of graphite. By comparing the 488 and 633 nm Cu spectra we can likely rule out the possibility that the graphite formation phenomena is simply due to the known C-C bond catalyzing ability of Pt. Referring back to the UV-Vis spectra presented in Figure 5.5 we see that Cu@Pt and Pt nanoparticles have significantly higher absorbances at 488 nm than at 633 nm. Conversely, the relative absorbances of 488 and 633 nm light are similar for the case of Cu nanoparticles. While it is unclear why the bands associated with PVP do not appear in the 633 nm Pt and Cu@Pt spectra, the fact that bands due to graphite, which were so clearly present in the case of the 488 nm Pt and Cu@Pt spectra, are completely absent, gives further support to the idea that the relative absorbance of a nanoparticle is strongly correlated with heat formation. Much like the UV-Vis data suggests, the Cu@Pt nanoparticles behave like pure Pt nanoparticles in terms of their propensity to form graphite showing that the nanoparticles are very effective at converting light into heat.

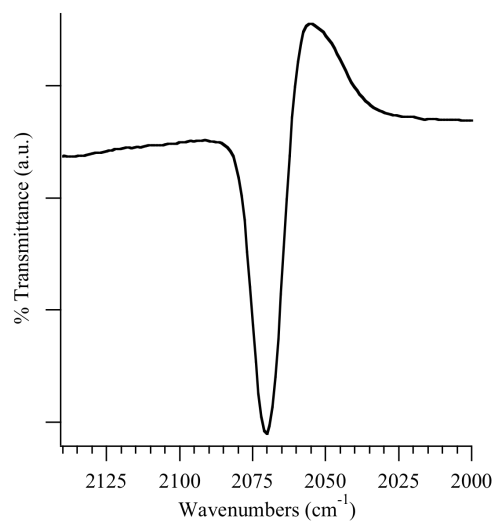
## 5.4 Conclusions

Studies described in this chapter have presented the synthesis of 3 nm Cu@Pt nanoparticles and their time-lapsed characterization by FTIR-CO probe, UV-Vis and XRD. We show that an oxidized Cu surface inhibits Pt deposition and that sub-monolayer amounts of Pt on the surface of the Cu nanoparticles are ample to disrupt the SPR band of Cu. We have also shown that transmetalation is a likely mechanism for Pt deposition onto Cu nanoparticles based on the fact that Pt cannot be deposited over the surface of Cu@CuO nanoparticles as well as our interpretation of the FTIR-CO, UV-Vis and XRD results. Finally, heating efficiencies of Cu and Cu@Pt nanoparticles derived from relative UV-Vis absorbances were correlated to the thermal degradation behavior of PVP on the surface of the nanoparticles as monitored by Raman spectroscopy.

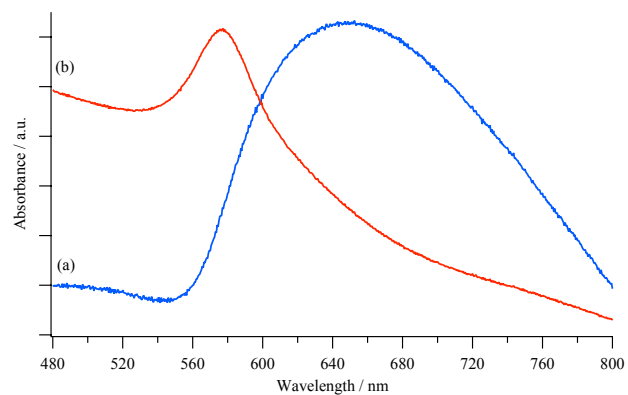
## 5.5 Supplemental Information



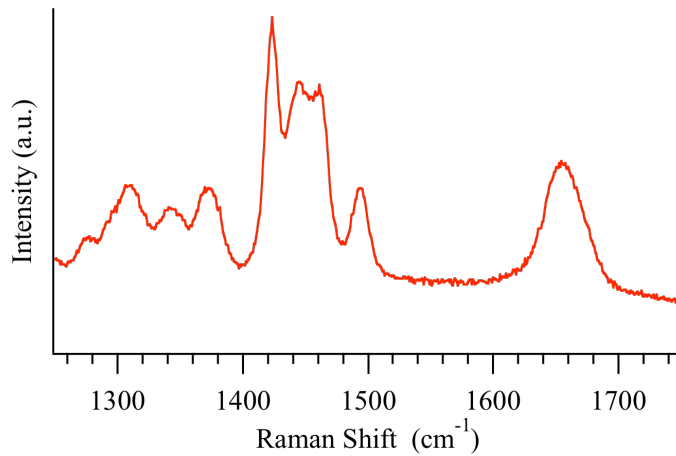
**Supplemental Information 5.1** FTIR-CO probe experiment of attempted Cu@CuO@Pt nanoparticle formation.



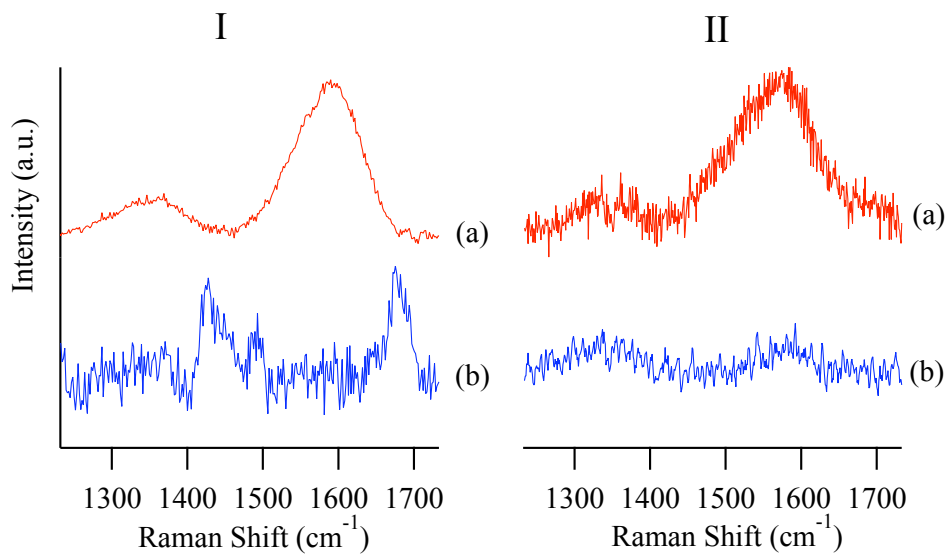
**Supplemental Information 5.2** FTIR-CO probe experiment of monometallic Pt nanoparticles (8 nm diameter).



**Supplemental Information 5.3** UV-Vis of (a) Cu@CuO and (b) Cu nanoparticles.



**Supplemental Information 5.4** Raman spectra of neat PVP acquired with 633 nm excitation.



**Supplemental Information 5.5** Raman spectra of Cu nanoparticles collected with (I) 488 nm and (II) 633 nm excitation. Spectrum (Ia) was collected with 5 mW power and (Ib) with 1 mW power. Spectrum (IIa) was collected with 6 mW power and (IIb) with 4 mW power.

## 5.6 References

- (1) Nilekar, A. U.; Mavrikakis, M. *Surf. Sci.* **2008**, *602*, L89-L94.
- (2) Romanowski, S.; Bartczak, W. M.; Wesolkowski, R. *Langmuir* **1999**, *15*, 5773-5780.
- (3) Xiao, L.; Zhuang, L.; Liu, Y.; Lu, J.; Abruna, H. D. *J. Am. Chem. Soc.* **2009**, *131*, 602-608.
- (4) Alayoglu, S.; Nilekar, A.; Mavrikakis, M.; Eichhorn, B. *Nature Materials* **2008**, *7*, 333-338.
- (5) Rodriguez, J. A.; Goodman, D. W. *J Phys Chem-US* **1991**, *95*, 4196-4206.
- (6) Campbell, R. A.; Rodriguez, J. A.; Goodman, D. W. *Phys. Rev. B* **1992**, *46*, 7077-7087.
- (7) Greeley, J.; Mavrikakis, M. *Nat Mater* **2004**, *3*, 810-815.
- (8) Greeley, J.; Norskov, J. K.; Mavrikakis, M. *Annu. Rev. Phys. Chem.* **2002**, *53*, 319-348.
- (9) Lee, W. R.; Kim, M. G.; Choi, J. R.; Park, J. I.; Ko, S. J.; Oh, S. J.; Cheon, J. J. *Am. Chem. Soc.* **2005**, *127*, 16090-16097.
- (10) Park, J. I.; Cheon, J. *J. Am. Chem. Soc.* **2001**, *123*, 5743-5746.
- (11) Wang, Y.; Toshima, N. *J Phys Chem B* **1997**, *101*, 5301-5306.
- (12) Zhou, S. H.; Varughese, B.; Eichhorn, B.; Jackson, G.; McIlwrath, K. *Angew Chem Int Edit* **2005**, *44*, 4539-4543.
- (13) Mulvaney, P.; Ahrenstorf, K.; Heller, H.; Kornowski, A.; Broekaert, J.; Weller, H. *Adv. Funct. Mater.* **2008**, *18*, 3850-3856.

- (14) Dulaurent, O.; Courtois, X.; Perrichon, V.; Bianchi, D. *J Phys Chem B* **2000**, *104*, 6001-6011.
- (15) Bradley, J. S.; Hill, E. W.; Chaudret, B.; Duteil, A. *Langmuir* **1995**, *11*, 693-695.
- (16) Bourane, A.; Dulaurent, O.; Bianchi, D. *J. Catal.* **2000**, *196*, 115-125.
- (17) Rauscher, H.; Hager, T.; Diemant, T.; Hoster, H.; De, Buatier, M., F.; Behm, R. *J. Surf. Sci.* **2007**, *601*, 4608-4619.
- (18) Bordoko, Y; Habas, S.; Koebel, M.; Yang, P.; Frei, H.; Somorjai, G. A. *J. Phys. Chem. B* **2006**, *110*, 23052-23059.
- (19) Wang, Y.; Alsmeyer, D. C.; McCreery, R. L. *Chem. Mater.* **1990**, *2*, 557-563.

## Chapter 6: Conclusions and Future Work

### 6.1 Conclusions

Work presented in this thesis is concerned with the synthesis, characterization and catalytic properties of bimetallic nanoparticles. The work presented here has shown bimetallic nanoparticles to be unique in that non-thermodynamic phases can be accessed and that the overall architecture of the bimetallic system, i.e., core@shell versus alloy, can drastically change their catalytic properties. Furthermore, this work shows that under relevant catalytic conditions, the architectures of bimetallic nanoparticles can be dynamic and reversible.

Our efforts were motivated by the desire to understand the relationships that exist between metallic nanoparticle structure and their function as catalysts. The core@shell nanoparticle architecture is particularly interesting because it can be viewed as an analogue to overlayer planar structures that are currently under investigation by the surface science community as well as computational chemists performing DFT calculations on similar systems. These bimetallic overlayer structures have unique surface electronic properties that are dissimilar from the two metals by themselves or alloyed in the bulk. Our desire was to synthesize and fully characterize core@shell bimetallic nanoparticles that would mimic the systems described above.

Though this thesis is a testament to some of those advancements, much work remains due to the complexity of small nanoparticles with core@shell and alloy architectures and the abundance of possible bimetallic combinations. While

even initial characterization of these bimetallic nanoparticles is often non-trivial, understanding their structure under catalytically relevant conditions can be quite difficult. Furthermore, determining what chemical or physical property of a bimetallic nanoparticle is responsible for their observed catalytic activity remains a very difficult task.

In Chapter 2 we demonstrated that carbonaceous overlayers formed from PVP can be deleterious to the catalytic activity of Pt nanoparticle catalysts for propene hydrogenation. Somewhat surprisingly, when the PVP coatings are left intact, the catalytic activity is approximately as high as when the PVP/carbon layers are oxidatively removed before the catalysis reaction is run. We found that only under inert atmosphere, high temperature pre-catalysis conditionings was a decrease in catalytic activity observed. We propose that a thin, dense carbonaceous layer is forming under these inert conditions and that this carbon blocks catalytically active sites. This hypothesis is corroborated by Raman spectra that show D and G bands associated with PVP degradation and CO chemisorption data that shows significantly lower surface areas on inert atmosphere annealed NPs compared to both as-prepared and air-oxidized NPs.

In Chapter 3 we showed that small PdCu alloy NPs possess a thermodynamically unfavored random alloy fcc phase at low temperatures and that these NPs transition to the thermodynamically favorable ordered bcc phase upon heating at low temperatures either in colloidal suspension or as unsupported NP powders. The phase transition can be suppressed by supporting the NPs in an inert matrix that spatially isolates the NPs and inhibits NP growth. These results

strongly suggest that NP growth is a requirement for the  $\alpha$  to  $\beta$  phase transition and offers a unique view of the interplay between thermodynamic and kinetic variables that control NP alloy structures.

In Chapter 4 we used *ex situ* CO adsorption DRIFT spectroscopy in conjunction with TPR studies to show that oxidized Ru@Pt and PtRu alloy catalysts show similar surface structures and CO oxidation activities while reduced Ru@Pt and PtRu alloy catalysts show significantly different surface structures and CO oxidation activities. Repeated catalyst cycling showed that the different surface structures of the Ru@Pt and PtRu alloy catalysts are reversible over several reduction-oxidation cycles. We also showed by STEM-EDS that the Ru@Pt catalyst maintains its core@shell architecture even after multiple oxidation-reduction cycles at 210 °C.

In Chapter 5 we presented the time-lapsed characterization of 3 nm Cu@Pt nanoparticles and proposed a transmetallation mechanism for the Pt shell deposition over Cu core nanoparticles. Finally, heating efficiencies of Cu and Cu@Pt nanoparticles derived from relative UV-Vis absorbances were correlated to the thermal degradation behavior of PVP on the surface of the nanoparticles as monitored by Raman spectroscopy.

## 6.2 Future Work

Three of the most interesting thrusts to explore based on the findings in this thesis are further exploration of synthetic techniques to create non-thermodynamic phases of bimetallic nanoparticles, forced *in situ* formation of core@shell nanoparticle catalysts and combined DRIFT or Raman spectroscopy with online monitoring of catalytic reactions. First, exploring the synthesis of new, and perhaps

thermodynamically unfavorable bimetallic alloy nanoparticles is worthy of attention due to the high cost of PGMs in many catalytically active materials. Moving away from these materials by synthesizing and catalytically testing new bimetallic alloy nanoparticles that have a low PGM:early transition metal (Mo, W, Fe) ratio would certainly be an interesting and industrially relevant endeavor. Based on the wide array of controllable parameters involved in nanoparticle synthesis, there are bound to be interesting and potentially catalytically relevant materials to be discovered.

Recent studies on adsorbate-induced nanoparticle restructuring may provide not only a dynamic understanding of the fate of a bimetallic nanoparticle during and after catalysis, but they may also provide new synthetic pathways to creating otherwise difficult to obtain nanoparticle architectures. Core@shell nanoparticle architectures may be more easily obtained by using gas or liquid-phase adsorbates to attract the desired metal to the surface of a preformed alloy or gradient alloy nanoparticle than by creating the core@shell nanoparticle using common solution-phase synthetic techniques.

Finally, by combining *in situ* vibrational spectroscopy/online gas phase product analysis with the growing repertoire of well-characterized core@shell and alloy bimetallic nanoparticles in our lab, we expect to gain a more complete picture of the structure-function relationships that exist for these catalysts. Having the ability to correlate the structure of a bimetallic nanoparticle catalyst via *ex situ* (TEM, UV-Vis, XRD, FTIR-CO, EDS, etc.) and *in situ* (DRIFT and Raman spectroscopy) studies with its catalytic activity would be a powerful experimental combination.

## Co-author contributions and acknowledgements

Chapters 2-5 have been submitted or are in preparation to be submitted as peer-reviewed articles. The contributions of the co-authors and those who have aided in the work are listed below according to chapter.

All Chapters: Dr. Wen-An Chiou trained me on the LaB<sub>6</sub> TEM used for most of the TEM images in this thesis. Dr. Peter Zavalij trained me on the operation of the XRD instrument.

Chapter 2: Professor James Dumesic and Mark Tucker at the University of Wisconsin performed the CO chemisorption measurements shown in Table 2.1.

Chapter 4: Dr. Selim Alayoglu, at the University of California, Berkeley, synthesized the Ru@Pt and PtRu alloy nanoparticles and subsequent catalysts under investigation in that chapter. Dr. Zili Wu at Oak Ridge National Lab trained me on their DRIFTS system during my three-week stay over the summer of 2008. Dr. Wu also performed many of the CO adsorption DRIFTS experiments shown in Figure 4.3. Dr. Larry Lai at the UMD Nanocenter NISP lab helped acquire the STEM-EDS measurements of Ru@Pt catalysts shown in Figures 1.3 and 4.2.

## Alphabetical Listing of References by First Author

- (1) Aiken, J. D.; Finke, R. G. *J Mol Catal A-Chem* **1999**, *145*, 1-44.
- (2) Alayoglu, S.; Nilekar, A.; Mavrikakis, M.; Eichhorn, B. *Nat Mater* **2008**, *7*, 333-338.
- (3) Alayoglu, Selim. Ph.D. Thesis, University of Maryland, College Park, MD, 2008.
- (4) Alexeev, O. S.; Chin, S. Y.; Engelhard, M. H.; Ortiz-Soto, L.; Amiridis, M. D. *J. Phys. Chem. B* **2005**, *109*, 23430-23443.
- (5) Amekura, H.; Kono, K.; Takeda, Y.; Kishimoto, N. *Appl. Phys. Lett.* **2005**, *87*, 153105.
- (6) Argo, A. M.; Odzak, J. F.; Lai, F. S.; Gates, B. C. *Nature* **2002**, *415*, 623-626.
- (7) Assmann, J.; Loffler, E.; Birkner, A.; Muhler, M. *Catal. Today* **2003**, *85*, 235-249.
- (8) Bao, X.; Barth, J. V.; Lehmpfuhl, G.; Schuster, R.; Uchida, Y.; Schlogl, R.; ERTL, G. *Surf. Sci.* **1993**, *284*, 14-22.
- (9) Bard, A. J.; Faulkner, L. R. *Electrochemical Methods: Fundamentals and Applications*; John Wiley & Sons: New York, 2001;
- (10) Baird, A. S.; Kross, K. M.; Gottschalk, D.; Hinson, E. A.; Wood, N.; Layman, K. A. *J. Phys. Chem. C* **2007**, *111*, 14207-14214.
- (11) Barth, J. V.; Brune, H.; Ertl, G.; Behm, R. J. *Phys. Rev. B* **1990**, *42*, 9307-9318.
- (12) Bell, A. T. *Science* **2003**, *299*, 1688-1691.

- (13) Bernardi, F.; Alves, M.; Traverse, A.; Silva, D.; Scheeren, C.; Dupont, J.; Morais, J. *J. Phys. Chem. C* **2009**, *113*, 3909-3916.
- (14) Bian, C. R.; Suzuki, S.; Asakura, K.; Ping, L.; Toshima, N. *J Phys Chem B* **2002**, *106*, 8587-8598.
- (15) Bonnemann, H.; Richards, R. M. *Eur J Inorg Chem* **2001**, 2455-2480.
- (16) Borodko, Y.; Habas, S.; Koebel, M.; Yang, P.; Frei, H.; Somorjai, G. A. *J Phys Chem B* **2006**, *110*, 23052-23059.
- (17) Borodko, Y.; Humphrey, S. M.; Tilley, T. D.; Frei, H.; Somorjai, G. A. *J. Phys. Chem. C* **2007**, *111*, 6288-6295.
- (18) Bourane, A.; Dulaurent, O.; Bianchi, D. *J. Catal.* **2000**, *196*, 115-125.
- (19) Bond, G. C.; Thompson, D. T. *Catal. Rev.-Sci. and Eng.* **1999**, *41*, 319-388.  
*98*, 10180-10188.
- (20) Bonnemann, H.; Brijoux, W.; Brinkmann, R.; Dinjus, E.; Jousen, T.; Korall, B. *Angew. Chem.-Int. Ed.* **1991**, *30*, 1312-1314.
- (21) Borchert, H.; Tenske, D.; Kolny-Olesiak, J.; Parisi, J.; Al-Shamery, K.; Baeumer, M. *Angew. Chem.-Int. Ed.* **2007**, *46*, 2923-2926.
- (22) Bozzolo, G.; Garces, J. E.; Noebe, R. D.; Abel, P.; Mosca, H. O. *Prog. Surf. Sci.* **2003**, *73*, 79-116.
- (23) Bradley, J. S.; Hill, E. W.; Behal, S.; Klein, C.; Chaudret, B.; Duteil, A. *Chem. Mater.* **1992**, *4*, 1234-1239.
- (24) Bradley, J. S.; Hill, E. W.; Klein, C.; Chaudret, B.; Duteil, A. *Chem. Mater.* **1993**, *5*, 254-256.

- (25) Bradley, J. S.; Hill, E. W.; Chaudret, B.; Duteil, A. *Langmuir* **1995**, *11*, 693-695.
- (26) Bradley, J. S.; Millar, J. M.; Hill, E. W.; Klein, C.; Chaudret, B.; Duteuil, A.; Geus, J. W.; Joyner, R. W.; Fouilloux, P.; Sermon, P. A.; Ichikawa, M.; Bozonverduraz, F. *Stud. Surf. Sci. Catal.* **1993**, *75*, 969-979.
- (27) Bradley, J. S.; Via, G. H.; Bonneviot, L.; Hill, E. W. *Chem. Mater.* **1996**, *8*, 1895-1903.
- (28) Bratlie, K. M.; Lee, H.; Komvopoulos, K.; Yang, P.; Somorjai, G. A. *Nano Letters* **2007**, *7*, 3097-3101.
- (29) Burda, C.; Chen, X. B.; Narayanan, R.; El-Sayed, M. A. *Chem. Rev.* **2005**, *105*, 1025-1102.
- (30) Cable, R.; Schaak, R. *Chem. Mater.* **2007**, *19*, 4098-4104.
- (31) Campbell, R. A.; Rodriguez, J. A.; Goodman, D. W. *Phys. Rev. B* **1992**, *46*, 7077-7087.
- (32) Campbell, C. *Science* **2002**, *298*, 811-814.
- (33) Chan, H. Y. H.; Zou, S. Z.; Weaver, M. J. *J. Phys. Chem. B* **1999**, *103*, 11141-11151.
- (34) Chin, S. Y.; Alexeev, O. S.; Amiridis, M. D. *J. Catal.* **2006**, *243*, 329-339.
- (35) Chin, S. Y.; Williams, C. T.; Amiridis, M. D. *J. Phys. Chem. B* **2006**, *110*, 871-882.
- (36) Choudhary, T. V.; Sivadinarayana, C.; Chusuei, C. C.; Datye, A. K.; Fackler, J. P.; Goodman, D. W. *J. Catal.* **2002**, *207*, 247-255.

- (37) Coq, B.; Kumbhar, P. S.; Moreau, C.; Moreau, P.; Figueras, F. *J. Phys. Chem.* **1994**,
- (38) Cremer, P.; Stanners, C.; Niemantsverdriet, J. W.; Shen, Y. R.; Somorjai, G. *Surf. Sci.* **1995**, *328*, 111-118.
- (39) Du, Y. K.; Yang, P.; Mou, Z. G.; Hua, N. P.; Jiang, L. *J. Appl. Polym. Sci.* **2006**, *99*, 23-26.
- (40) Dulaurent, O.; Courtois, X.; Perrichon, V.; Bianchi, D. *J. Phys. Chem. B* **2000**, *104*, 6001-6011.
- (41) Enache, D. I.; Edwards, J. K.; Landon, P.; Solsona-espriu, B.; Carley, A. F.; Herzing, A. A.; Watanabe, M.; Kiely, C. J.; Knight, D. W.; Hutchings, G. J. *Science* **2006**, *311*, 362-365.
- (42) Ertl, G. *Science* **1991**, *254*, 1750-1755.
- (43) Fairbanks, M. C.; Benfield, R. E.; Newport, R. J.; Schmid, G. *Solid State Commun.* **1990**, *73*, 431-436.
- (44) Fan, F.; Liu, D.; Wu, Y.; Duan, S.; Xie, Z.; Jiang, Z.; Tian, Z. *J. Am. Chem. Soc.* **2008**, *130*, 6949-+.
- (45) Ferrando, R.; Jellenik, J.; Johnston, R. L. *Chem. Rev.* **2008**, *108*, 845-910.
- (46) Fukuoka, A.; Kimura, T.; Kosugi, N.; Kuroda, H.; Minai, Y.; Sakai, Y.; Tominaga, T.; Ichikawa, M. *J. Catal.* **1990**, *126*, 434-450.
- (47) Grass, M.; Yue, Y.; Habas, S.; Rioux, R.; Teall, C.; Yang, P.; Somorjai, G. *J. Phys. Chem. C* **2008**, *112*, 4797-4804.
- (48) Grass, M. E.; Joo, S. H.; Zhang, Y.; Somorjai, G. A. *J. Phys. Chem. C* **2009**, *113*, 8616-8623.

- (49) Greeley, J.; Mavrikakis, M. *Nat Mater* **2004**, *3*, 810-815.
- (50) Greeley, J.; Norskov, J. K.; Mavrikakis, M. *Annu. Rev. Phys. Chem.* **2002**, *53*, 319-348.
- (51) Habas, S. E.; Lee, H.; Radmilovic, V.; Somorjai, G. A.; Yang, P. *Nat Mater* **2007**, *6*, 692-697.
- (52) Hammer, B.; Norskov, J. K. *Surf. Sci.* **1995**, *343*, 211-220.
- (53) Hammer, B.; Morikawa, Y.; Norskov, J. K. *Phys. Rev. Lett.* **1996**, *76*, 2141-2144.
- (54) Haruta, M. *Gold Bull* **2004**, *37*, 27-36.
- (55) Haruta, M. *Catal. Today* **1997**, *36*, 153-166.
- (56) Herrera, J. E.; Balzano, L.; Borgna, A.; Alvarez, W. E.; Resasco, D. E. *J. Catal.* **2001**, *204*, 129-145.
- (57) Hutchings, G. J.; Haruta, M. *Appl Catal A-Gen* **2005**, *291*, 2-5.
- (58) Ichikawa, M.; Rao, L. F.; Kimura, T.; Fukuoka, A. *J. Mol. Catal.* **1990**, *62*, 15-35.
- (59) Kim, S.; Yin, Y.; Alivisatos, A.; Somorjai, G. A.; Yates, J. T. *J. Am. Chem. Soc.* **2007**, *129*, 9510-9513.
- (60) Knecht, M. R.; Weir, M. G.; Frenkel, A. I.; Crooks, R. M. *Chem. Mater.* **2008**, *20*, 1019-1028.
- (61) Kolb, U.; Quaiser, S. A.; Winter, M.; Reetz, M. T. *Chem. Mater.* **1996**, *8*, 1889-1894.
- (62) Konya, Z.; Molnar, E.; Tasi, G.; Niesz, K.; Somorjai, G. A.; Kiricsi, I. *Catal. Lett.* **2007**, *113*, 19-28.

- (63) Kowal, A.; Li, M.; Shao, M.; Sasaki, K.; Vukmirovic, M. B.; Zhang, J.; Marinkovic, N. S.; Liu, P.; Frenkel, A. I.; Adzic, R. R. *Nat Mater* **2009**, *8*, 325-330.
- (64) Lang, H.; Maldonado, S.; Stevenson, K.; Chandler, B. *J. Am. Chem. Soc.* **2004**, *126*, 12949-12956.
- (65) Lange, C.; De Caro, D.; Gamez, A.; Storck, S.; Bradley, J. S.; Maier, W. F. *Langmuir* **1999**, *15*, 5333-5338.
- (66) Lee, H.; Habas, S. E.; Kweskin, S.; Butcher, D.; Somorjai, G. A.; Yang, P. D. *Angew. Chem.-Int. Ed.* **2006**, *45*, 7824-7828.
- (67) Lee, W. R.; Kim, M. G.; Choi, J. R.; Park, J. I.; Ko, S. J.; Oh, S. J.; Cheon, J. *J. Am. Chem. Soc.* **2005**, *127*, 16090-16097.
- (68) Lewera, A.; Zhou, W. P.; Hunger, R.; Jaegermann, W.; Wieckowski, A.; Yockel, S.; Bagus, P. S. *Chem. Phys. Lett.* **2007**, *447*, 39-43.
- (69) Li, Y.; El-Sayed, M. A. *J Phys Chem B* **2001**, *105*, 8938-8943.
- (70) Lim, B.; Wang, J.; Camargo, P.; Jiang, M.; Kim, M. J.; Xia, Y. *Nano Lett.* **2008**, *8*, 2535-2540.
- (71) Liu, R. X.; Iddir, H.; Fan, Q. B.; Hou, G. Y.; Bo, A. L.; Ley, K. L.; Smotkin, E. S.; Sung, Y. E.; Kim, H.; Thomas, S.; Wieckowski, A. *J Phys. Chem. B* **2000**, *104*, 3518-3531.
- (72) Liu, Z.; Reed, D.; Kwon, G.; Shamsuzzoha, M.; Nikles, D. E. *J. Phys. Chem. C* **2007**, *111*, 14223-14229.
- (73) Liu, Z.; Shamsuzzoha, M.; Ada, E. T.; Reichert, W. M.; Nikles, D. E. *J. Power Sources* **2007**, *164*, 472-480.

- (74) Ma, T.; Fu, Q.; Su, H.; Liu, H.; Cui, Y.; Wang, Z.; Mu, R.; Li, W.; Bao, X. *ChemPhysChem* **2009**, *10*, 1013-1016.
- (75) Mavrikakis, M.; Hammer, B.; Norskov, J. K. *Phys. Rev. Lett.* **1998**, *81*, 2819-2822.
- (76) Mazzieri, V.; Coloma-Pascual, F.; Arcoya, A.; L'Argentiere, P.; Figoli, N. S. *Appl. Surf. Sci.* **2003**, *210*, 222-230.
- (77) McClure, S. M.; Goodman, D. W. *Chem. Phys. Lett.* **2009**, *469*, 1-13.
- (78) McIntyre, B. J.; Salmeron, M. B.; Somorjai, G. A. *Catal. Lett.* **1992**, *14*, 263-269.
- (79) Moores, A.; Goettmann, F. *New J. Chem.* **2006**, *30*, 1121-1132.
- (80) Mu, R.; Fu, Q.; Liu, H.; Tan, D.; Zhai, R.; Bao, X. *Appl. Surf. Sci.* **2009**, *255*, 7296-7301.
- (81) Mulvaney, P.; Ahrenstorff, K.; Heller, H.; Kornowski, A.; Broekaert, J.; Weller, H. *Adv. Funct. Mater.* **2008**, *18*, 3850-3856.
- (82) Murray, C. B.; Kagan, C. R.; Bawendi, M. G. *Annu Rev Mater Sci* **2000**, *30*, 545-610.
- (83) Narayanan, R.; El-Sayed, M. A. *Nano Lett.* **2004**, *4*, 1343-1348.
- (84) Narayanan, R.; El-Sayed, M. A. *J Phys Chem B* **2005**, *109*, 12663-12676.
- (85) Nashner, M. S.; Frenkel, A. I.; Somerville, D.; Hills, C. W.; Shapley, J. R.; Nuzzo, R. G. *J. Am. Chem. Soc.* **1998**, *120*, 8093-8101.
- (86) Ng, Y. H.; Ikeda, S.; Harada, T.; Park, S.; Sakata, T.; Mori, H.; Matsumura, M. *Chem. Mater.* **2008**, *20*, 1154-1160.
- (87) Nilekar, A. U.; Mavrikakis, M. *Surf. Sci.* **2008**, *602*, L89-L94.

- (88) Niemantsverdriet, J. W. *Spectroscopy in Catalysis*; Wiley-VCH: Weinheim, 2007;
- (89) Ozbay, E. *Science* **2006**, *311*, 189-193.
- (90) Pan, X.; Fan, Z.; Chen, W.; Ding, Y.; Luo, H.; Bao, X. *Nat Mater* **2007**, *6*, 507-511.
- (91) Park, J. Y.; Zhang, Y.; Grass, M.; Zhang, T.; Somorjai, G. A. *Nano Lett.* **2008**, *8*, 673-677.
- (92) Park, J. I.; Cheon, J. *J. Am. Chem. Soc.* **2001**, *123*, 5743-5746.
- (93) Pecharsky, V. K.; Zavalij, P. Y. *Fundamentals of Powder Diffraction and Structural Characterization of Materials*; Springer: 2009;
- (94) Ponec, V.; Bond, G. C. *Catalysis by Metals and Alloys*; Elsevier: Amsterdam, 1995;
- (95) Rao, L. F.; Fukuoka, A.; Kosugi, N.; Kuroda, H.; Ichikawa, M. *J Phys Chem-US* **1990**, *94*, 5317-5327.
- (96) Rauscher, H.; Hager, T.; Diemant, T.; Hoster, H.; De, Buatier, M., F.; Behm, R. *J. Surf. Sci.* **2007**, *601*, 4608-4619.
- (97) Reetz, M. T.; Helbig, W.; Quaiser, S. A. *Chem. Mater.* **1995**, *7*, 2227-&.
- (98) Rioux, R. M.; Song, H.; Hoefelmeyer, J. D.; Yang, P.; Somorjai, G. A. *J. Phys. Chem. B* **2005**, *109*, 2192-2202.
- (99) Rioux, R. M.; Song, H.; Grass, M.; Habas, S.; Niesz, K.; Hoefelmeyer, J. D.; Yang, P.; Somorjai, G. A. *Topics in Catal.* **2006**, *39*, 167-174.
- (100) Rodriguez, J. A.; Goodman, D. W. *J Phys Chem-US* **1991**, *95*, 4196-4206.
- (101) Rodriguez, J. A.; Goodman, D. W. *Surf Sci Rep* **1991**, *14*, 1-107.

- (102) Romanowski, S.; Bartczak, W. M.; Wesolkowski, R. *Langmuir* **1999**, *15*, 5773-5780.
- (103) Sanchez-Escribano, V.; Arrighi, L.; Riani, P.; Marazza, R.; Busca, G. *Langmuir* **2006**, *22*, 9214-9219.
- (104) Schaak, R. E.; Sra, A. K.; Leonard, B. M.; Cable, R. E.; Bauer, J. C.; Han, Y. F.; Means, J.; Teizer, W.; Vasquez, Y.; Funck, E. S. *J. Am. Chem. Soc.* **2005**, *127*, 3506-3515.
- (105) Schlapka, A.; Kasberger, U.; Menzel, D.; Jakob, P. *Surf. Sci.* **2002**, *502*, 129-135.
- (106) Schmid, G.; Baumle, M.; Geerkens, M.; Helm, I.; Osemann, C.; Sawitowski, T. *Chem. Soc. Rev.* **1999**, *28*, 179-185.
- (107) Scott, R. W. J.; Wilson, O. M.; Oh, S. K.; Kenik, E. A.; Crooks, R. M. *J. Am. Chem. Soc.* **2004**, *126*, 15583-15591.
- (108) Seo, J. W.; Jun, Y. W.; Ko, S. J.; Cheon, J. *J Phys Chem B* **2005**, *109*, 5389-5391.
- (109) Sharrna, P.; Brown, S.; Walter, G.; Santra, S.; Moudgil, B. *Adv Colloid Interface* **2006**, *123*, 471-485.
- (110) Shiraishi, Y.; Ikenaga, D.; Toshima, N. *Aust. J. Chem.* **2003**, *56*, 1025-1029.
- (111) Shriver, D. F.; Atkins, P. W. *Inorganic Chemistry*; W.H. Freeman and Company: New York, 2000;
- (113) Sinfelt, J. H. *Bimetallic Catalysts: Discoveries, Concepts and Applications*; John Wiley & Sons: New York, 1983;
- (114) Sinfelt, J. H. *J. Catal.* **1973**, *29*, 308-315.

- (115) Sinfelt, J. H. *Surf. Sci.* **2002**, *500*, 923-946.
- (116) Smithells, C.; Brandes, E. *Metals Reference Book*; Butterworths: London, 1976;
- (117) Somorjai, G. A.; Park, J. Y. *J. Chem. Phys.* **2008**, *128*, 182504.
- (118) Somorjai, G. A.; Park, J. Y. *Top Catal* **2008**, *49*, 126-135.
- (119) Song, H.; Rioux, R. M.; Hoefelmeyer, J. D.; Komor, R.; Niesz, K.; Grass, M.;  
Yang, P. D.; Somorjai, G. A. *J. Am. Chem. Soc.* **2006**, *128*, 3027-3037.
- (120) Spiewak, B. E.; Shen, J.; Dumesic, J. A. *J. Phys. Chem.* **1995**, *99*, 17640-17644.
- (121) Sra, A. K.; Schaak, R. E. *J. Am. Chem. Soc.* **2004**, *126*, 6667-6672.
- (122) Stencel, J. M. *Raman Spectroscopy for Catalysis*; Van Nostrand Reinhold: New  
York, 1990;
- (123) Tao, A.; Habas, S.; Yang, P. *Small* **2008**, *4*, 310-325.
- (124) Toshima, N.; Yonezawa, T.; Harada, M.; Asakura, K.; Iwasawa, Y. *Chem. Lett.*  
**1990**, 815-818.
- (125) Toshima, N.; Wang, Y. *Advan. Mater.* **1994**, *6*, 245-247.
- (126) Toshima, N.; Yonezawa, T. *New J. Chem.* **1998**, *22*, 1179-1201.
- (127) Valden, M.; Lai, X.; Goodman, D. W. *Science* **1998**, *281*, 1647-1650.
- (128) Vanhove, M. A.; Moritz, W.; Over, H.; Rous, P. J.; Wander, A.; Barbieri, A.;  
Materer, N.; Starke, U.; Somorjai, G. A. *Surf Sci Rep* **1993**, *19*, 191-229.
- (129) Vasquez, Y.; Luo, Z.; Schaak, R. *J. Am. Chem. Soc.* **2008**, *130*, 11866-11867.
- (130) Wang, Y.; Toshima, N. *J Phys Chem B* **1997**, *101*, 5301-5306.
- (131) Wang, Y.; Alsmeyer, D. C.; McCreery, R. L. *Chem. Mater.* **1990**, *2*, 557-563.
- (132) Waychunas, G. A. *J. Mater. Sci.* **1983**, *18*, 195-207.
- (133) Wise, F. W. *Accounts Chem Res* **2000**, *33*, 773-780.

- (134) Wu, Z.; Zhou, S.; Zhu, H.; Dai, S.; Overbury, S. H. *J. Phys. Chem. C* **2009**, *113*, 3726-3734.
- (135) Xiao, L.; Zhuang, L.; Liu, Y.; Lu, J.; Abruna, H. D. *J. Am. Chem. Soc.* **2009**, *131*, 602-608.
- (136) Yan, W. F.; Petkov, V.; Mahurin, S. M.; Overbury, S. H.; Dai, S. *Catal Commun* **2005**, *6*, 404-408.
- (137) Ye, H.; Crooks, R. M. *J. Am. Chem. Soc.* **2007**, *129*, 3627-3633.
- (138) Yoo, J. W.; Hathcock, D. J.; El-sayed, M. A. *J. Catal.* **2003**, *214*, 1-7.
- (139) Zhang, Y.; Huang, W.; Habas, S.; Kuhn, J. N.; Grass, M. E.; Yamada, Y.; Yang, P.; Somorjai, G. A. *J. Phys. Chem. C* **2008**, *112*, 12092-12095.
- (140) Zhou, W.; Lewera, A.; Bagus, P. S.; Wieckowski, A. *J. Phys. Chem. C* **2007**, *111*, 13490-13496.
- (141) Zhou, S. H.; Varughese, B.; Eichhorn, B.; Jackson, G.; McIlwrath, K. *Angew Chem Int Edit* **2005**, *44*, 4539-4543.
- (142) Zhou, S.; Jackson, G. S.; Eichhorn, B. *Adv. Funct. Mater.* **2007**, *17*, 3099-3104.